UNIVERSITY OF CALIFORNIA
Los Angeles

Multi-Particle Bose-Einstein Correlations at 158 GeV A

A dissertation submitted in partial satisfaction of the
requirements for the degree Doctor of Philosophy
in Physics

by

Brian Lasiuk

1997

The dissertation of Brian Lasiuk is approved.

E. J. Hoffman

H. Huang

J. Hauser

G. J. Igo

C. A. Whitten Jr., Committee Chair

University of California, Los Angeles

1997

For my Mom

and

the memory of my Father.

Contents

List of Figures

List of Tables

ACKNOWLEDGEMENTS

When one undertakes to write a thesis in experimental high energy physics these days, you are dependent on many people; and even though you can not thank them all, there are certain individuals who must be specifically mentioned. First to mom and dad without whose support, none of this would have been possible. To my advisors, Prof. C. A. Whitten Jr. and Prof. G. J. Igo whom gave me the freedom, support, and opportunity to pursue my own interests within the experiment. To Dr. H. G. Fischer, whom was one of the few people I have met that was knowledgeable in every aspect of the experiment; design, construction, operation, simulation, analysis, and interpretation. I learned much in my interaction with him and I came away with a great deal of respect for him. Prof. H. Ströbele, with whom I worked very closely during the magnet mapping, gave me a great deal of responsibility within the collaboration. P. Buncic was always available to answer my, sometimes silly questions, whether regarding physics, C, or some DSPACK problem, but always with a smile—well usually. H. Appelshäuser helped me through some “serious” problems in my analysis and introduced me to John LeCarré. M. Calderon helped in finalizing the production script for the event reconstruction. A. Sandoval was always available to discuss problems; be it physics, analysis, or whatever. He also made sure I did not have to sleep in my office when my house burned down. And finally Prof. R. Stock, who is the driving force behind this experiment. It was not an easy job orchestrating a collaboration of 115 people from 17 institutions and 9 different countries, but he did it seamlessly. On a more personal level, he gave me a great deal of confidence with our short discussions, which I will always remember. He also made sure I could replace some of my Ferrari collection after the incendiary incident. My thanks to you all.

VITA

January 26, 1970	Born in Saskatoon, SK, Canada
May 22, 1991	BSc. conferred at University of Saskatchewan.
May 28, 1993	MSc. conferred at University of Saskatchewan.
December, 1997	Phd. conferred at University of Califoria at Los Angeles.

PUBLICATIONS

T. Emura et al. (TAGX Collaboration), Phys. Lett. B306 (1993) 6.

B. Lasiuk, Acta Phys. Slov. 47 (1997) 15.

B. Lasiuk for the NA49 Collaboration, Acta Phys. Slov. 47 (1997) 27.

B. Lasiuk for the NA49 Collaboration, Particle Identification in the NA49 TPCs, in press.

ABSTRACT OF THE DISSERTATION

Title of thesis

by

Brian Lasiuk
Doctor of Philosophy in Physics
University of California, Los Angeles, 1997
Professor C. A. Whitten Jr., Chair

NA49 is a large acceptance spectrometer which was designed to measure the charged hadrons produced in 158 GeV A Pb-Pb collisions at the CERN-SPS. The ultimate goal of such studies is to determine if the conventional hadronic degrees of freedom which govern nuclear matter are melted away at high matter and energy densities forming a weakly interacting partonic medium—a Quark-Gluon Plasma (QGP). In order to determine whether a phase transition to such a state occurs, it is important to characterize the properties of the source that is formed in nucleus-nucleus (AA) collisions. This thesis examines the geometrical and dynamic properties produced in Pb-Pb collisions through the technique of Hanbury-Brown and Twiss (HBT) intensity interferometry. In particular, the first measurement of radii parameters in the backward rapidity region will be presented. The technical aspect of how these parameters change with the use of identified particles will also be addressed. The first results from a method utilizing second order $<\mathrm{q}_i^2>$ moments to extract HBT parameters is also presented, and a method, and its first results, for extracting correlation parameters from a single event is given.

Chapter 1

Prologue

1.1 The Goal of Nuclear Physics

Nuclear physics began at the turn of the century with Rutherford's famous $\alpha-$backscattering experiment, which was the first indication of the presence of a small, dense, highly charged core at the center of atoms [1]. Since that time, the characterization of the properties, and dynamics of this system has defined the goals and problems of nuclear physics. These studies have benefited from a wide range of particle beams that have been available. Differing particle species, and energies varying over many orders of magnitude have allowed studies of various structures and interactions which have provided diverse and complementary information to our understanding of the sub-atomic world.

The advent of accelerators made controlled and systematic studies of nuclei, and nuclear processes, in the laboratory possible. Electron, photon, and hadron beams have provided complimentary information on the spatial extent of the nucleon and nuclei, as well as general nuclear properties, like binding energy, nucleon momentum distributions, magnetic moments, etc. They have also allowed modelling of the nucleon-nucleon (NN) interaction. These studies led directly to the discovery of the rich hadronic structure and the first ideas of nucleon sub-structure [2]. A framework for this substructure was given in terms of the quark model in the early 1960s [3].

Lepton beams led the way in probing these new degrees of freedom and supplied the first experimental evidence for such objects (quarks) at the Stanford Linear Accelerator (SLAC) in 1968 [4]. Not surprisingly, this spawned questions of how such a substructure could play a role in nuclei.

Sufficient energy to excite internal degrees of freedom of a system must be deposited in order to study its substructure. Just as energy deposited into atoms causes ionization which reveals atomic structure, it was believed a similar process could exist for nuclear systems to liberate quarks. Unfortunately, quarks and gluons do not behave in a "conventional" manner. Their interactions are described in terms of Quantum Chromodynamics (QCD) and although ionization of a hadron into its constituent quarks is not possible, QCD does allow for the formation of an "ideal gas" of quarks and gluons—a Quark Gluon Plasma (QGP). Under extreme densities, hadrons may overlap to such a degree that they, in effect, lose their identity, leaving only an extended system of quarks and gluons. Thus if a sufficiently large amount of energy could be deposited into nuclear matter, it may be possible to observe a phase transition to such a state.

Before the mid 1960s there was very little knowledge of what happens in nuclei under extreme energy densities. Conventional nuclear physics experiments typically deposit small amounts of energy into nuclei, mildly perturbing the system. This provides very little variation of energy density over that of normal nuclear matter. This is an important realization, because limitations in conventional nuclear descriptions are likely to be more prominent under extreme conditions. With this thought, a program to study nucleon-nucleus (pA) collisions at Brookhaven National Laboratory (BNL) began in the early 1960s. These studies focused on rather broad and general characterizations of such collisions, but they laid the groundwork for future ion-ion collisions, and in 1969, a dedicated heavy ion laboratory (GSI) opened in Germany. Its primary mission was to investigate the dynamics of large nuclear systems with the ultimate goal of reaching the "island of stability" thought to be around element $\mathbf{Z}$=114 [5]. In the mid 1970s, a small group initiated a program to study heavy ion collisions, at several hundred MeV per nucleon (MeV A) at the

Bevalac. Like the earlier BNL experiments, these investigations were also concerned with very general properties of systems created in the laboratory—total energy and multiplicity, particle spectra, etc [6]. A complimentary program at the European Center for Nuclear Research (CERN) Intersecting Storage Ring (ISR) also began. Collisions between lighter ions—deuterons and alphas—at a higher energy—up to $\sqrt{s} = 20$ GeV—were investigated.

By 1982, beams with projectiles as heavy as uranium and energies of several hundred MeV A were available at GSI, and up to 2.1 GeV A at the Bevalac. It was at this time an international group of scientists met in Bielefeld to discuss the possibility of producing and studying "Quark Matter" in the laboratory [7]. Although only a couple of hundred people attended, they provided motivation and outlined the possible physics that could be uncovered by studying collisions between ultra-relativistic heavy ions in the laboratory. The immediate consequence of this conference was the creation of two experimental programs to explore these possibilities at BNL and CERN.

In late 1986, both BNL and CERN accelerated intermediate mass ions (^{16}O) to energies of 14.6 GeV A and 60 GeV A respectively. The next year, the same laboratories accelerated heavier mass ions—^{28}Si at BNL and ^{32}S at CERN; and in 1988, CERN was able to reach energies of 200 GeV A. Although these experiments provided a look at the behavior of high density nuclear matter and provided a wealth of data concerning event characterization and particle spectra, perhaps their most important contribution was the demonstration, of the feasibility of producing and measuring collisions of relativistic heavy ions. The general success of these experiments led to the approval of very heavy ion beams—10.6 GeV A ^{197}Au beams at BNL and 158 GeV A ^{208}Pb beams at CERN in 1990. It was also at this time that approval for the construction of a new dedicated heavy ion accelerator at BNL, the Relativistic Heavy Ion Collider (RHIC), was given as well as the incorporation of a heavy ion program at the Large Hadron Collider (LHC) at CERN. Indeed relativistic heavy ion physics had become a major sub-discipline of nuclear physics in a short time.

It was with the new ^{197}Au and ^{208}Pb beams at BNL and CERN, that the first real hope of observing a transition from nuclear matter to quark matter was made a reality. It is with such anticipation and speculation that we enter the world of Heavy Ion Physics in the "SPS Pb Era".

Chapter 2

Heavy Ion Physics

2.1 Origin and Development of the Strong Interaction in Physics

The history of physics is one of unification. It has always been a goal to condense or unify the known interactions in nature into the simplest and most compact prescription. The results of the pursuit of this philosophy have, up until now, been quite successful as illustrated in figure 2.1. Quantum Electro-Dynamics (QED), which governs all Electro-Magnetic (EM) interactions was combined with Fermi's theory of weak interactions into the Glashow-Weinberg-Salam Electro-Weak (EW) theory. This along with Quantum Chromo-Dynamics (QCD), and General Relativity (GR) contains our most fundamental understanding of the forces in nature today and makes up what is called the Minimal Standard Model (MSM) [8].

All these theories (except for GR) are fully relativistic quantum field theories that are based on a single principle—local gauge invariance. Fundamentally, interactions in the MSM are understood as point-like particles which act upon one another via the exchange of quanta (gauge bosons). The strength of each interaction is characterized by a coupling constant which, with our current understanding, is a free parameter. As such, it can only be deduced from experiment. This is seen as one of the major shortcomings of the MSM. In fact, some 21 free parameters (i.e. masses, coupling constants, mixing angles), litter the MSM.

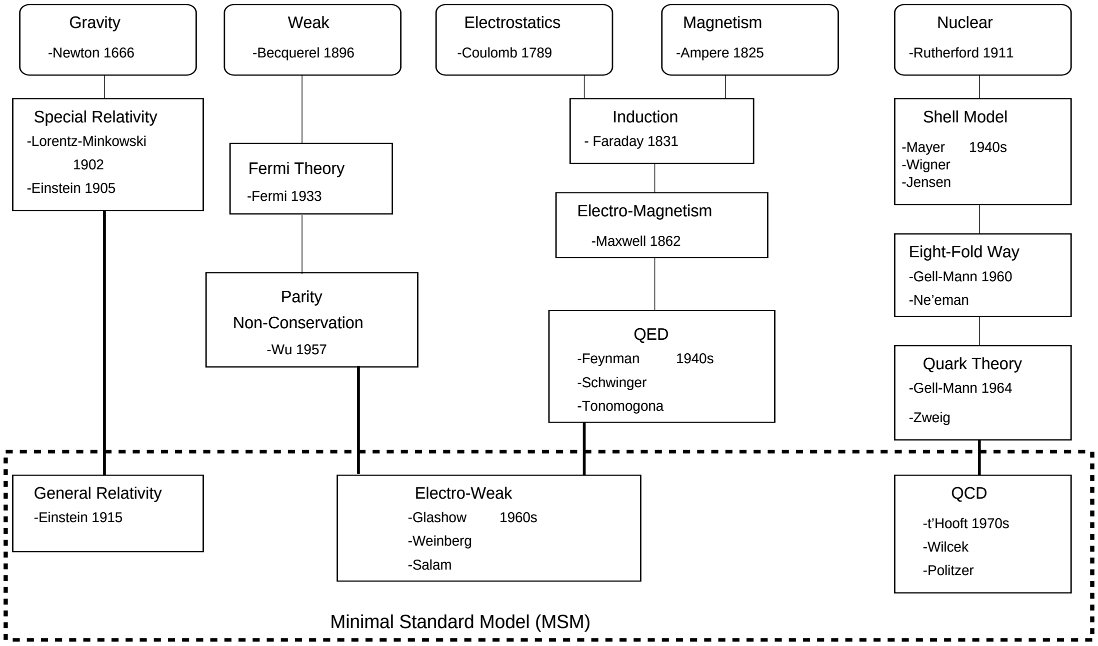

Figure 2.1: The evolution of the Standard Model and its four basic forces or interactions—Gravity, Weak, Electro-Magnetic, and Strong or Nuclear.

The fundamental constituents of matter come in two main species—leptons and quarks. Leptons interact only via the EW[1] interaction. However quarks carry an additional internal degree of freedom which allow them to bind into hadrons and ultimately, hadrons into nuclei. Although this binding is strong for hadrons, the coupling constant of the EM force is small ($\alpha \sim \frac{1}{137}$). This has allowed the use conventional perturbative techniques in extremely precise calculations. Furthermore this precision has been equalled in the laboratory so as to allow very stringent tests on the limit of the theory.[2] As such, the EW theory is extremely well understood.

---

[1] and gravity, but it is much weaker and generally neglected in particle processes.

[2] For example Magnetic moment of the muon: $\mu = 1.001165923(8)\ \mu_B$.

The same cannot be said of the strong interaction, which governs the physics at the nuclear level.

With the discovery of the neutron in 1931 [9], the composition of nuclei was thought to be complete, however a problem still remained because the neutron was electrically neutral. An EM force could not be invoked to explain the nuclear binding, so a new "strong" short range force that acted only between nucleons (hadrons) was postulated. In 1941 Yukawa proposed a possible mechanism for the strong force in which particle exchange would facilitate the attraction, or repulsion, between particles [10]. Experimental evidence for such a strongly interacting, intermediate mass particle came within a matter of years when the pion was discovered in 1947 [11]. With this, the nuclear system seemed complete. Protons and neutrons were bound in systems by a short range force which was mediated by the exchange of pions. From this simple picture, many phenomenological approaches were developed—most noteworthy the shell [12], and collective [13] models which allowed for descriptions of the bulk properties of nuclei across the periodic table.

Nonetheless as accelerator energies continued to increase, a multitude of new particles and resonance states were discovered, and questions arose of why such a rich hadronic structure existed [14]. It was during this period that nuclear physics split into two different camps; the conventional nuclear physicists who still looked to the nucleus as the ultimate testing ground, and particle physicists, who concentrated on the study of single particles, resonant states, and their interactions.

It was in fact the particle physicists, after recognizing symmetries and patterns in the quantum numbers and mass spectra of the hadrons, who formulated a description in which all known hadrons could be built up from a common substructure of just 3 constituent particles.[3] The particles, called quarks, had rather unusual properties. They carried fractional quantum numbers (i.e. electric charge, isospin, baryon number) and were endowed with a new internal degree of freedom called color. While color was initially introduced to rectify the problem of the quarks

---

[3] at the time only *up* (u), *down* (d), and *strange* (s) quarks were postulated.

apparent disregard for quantum statistics, it was later identified with the charge of the strong force, just as electric charge is that of the EM interaction. Furthermore quarks existed, or were confined in systems ("bags") where the observed quantum numbers were only integer (or half integer). The quark-quark interaction was, as the other forces in the MSM, mediated by the exchange of a gauge boson—the gluon. Like the photon it was massless, but unlike the photon, the gluon carried the charge of the interaction it mediated—color. As such, gluon-gluon interactions can occur at tree level, which is the major difference between the two theories.[4]

Experimental evidence for quarks eventually came from two different observations. First from SLAC, in an experiment reminiscent of Rutherford's backscattering experiment, high energy e^-p collisions suggested that the nucleon was composed of point-like constituents or partons [4]. Elsewhere, a small number of high energy pp collisions appeared to fragment into narrow cones or jets of particles, also consistent with the picture of confined quarks [15]. In spite of this circumstantial experimental evidence, general acceptance of QCD was only realized when t'Hooft showed that a spontaneously broken Yang-Mills field theory is renormalizable [16]. This led to the discovery of asymptotic freedom—the vanishing of the coupling constant at small distances—and a possible mechanism for the generation of a confining potential [17]. With this, the quarks of QCD were identified with the partons in the deep-inelastic scattering experiments, and studies began to focus on the implications and experimental consequences of the quark model and QCD.

2.2 QCD and Nuclear Physics

QCD is a fully relativistic, non-Abelian gauge field theory that describes the interactions of quarks and gluons [18]. It has two remarkable features, which are illustrated in the behavior of its coupling constant (α_s). QCD asymptotically ap-

---

[4] Actually γ-γ interactions can occur but they are second order (in the coupling constant) and therefore have a reduced probability in contrast to that of a $e^\pm$–$e^\pm$ interaction.

proaches that of a non-interacting free-field theory (i.e. $\lim_{q^2 \to \infty} \alpha_s = 0$) in the high-energy (short distance) regime. Conversely, at low energies (large distances), the theory is non-perturbative because the coupling constant can become arbitrarily large (i.e. $\lim_{q^2 \to 0} \alpha_s = \infty$). In this manner it is exactly opposite to QED. With this behavior, and the idea of composite hadrons, it is possible to understand the prediction it makes about the existence of a QGP.

Although QCD is derived from first principles, nuclear physics is still a purely phenomenological science. The shell model and nucleon-nucleon (NN) potentials all deal with an effective Hamiltonian which lacks any fundamental dynamics. The shell model takes nucleons as inert, non-relativistic objects present in a mean field, feeling only pair-wise NN forces. For example, the Paris potential is parameterized using the extensive data obtained from phase shift analysis in NN and πN scattering studies [19]. Although there have been more recent attempts to calculate the potential in terms of meson-nucleon coupling strengths [20], it is still not anything that can be called fundamental in terms of the MSM, and herein lies the problem. The strong force should be described in the context of a single theory which does not rely on separate approaches for the different energy/distance regimes (i.e. the nuclear and QCD scales). In this light, it is desirable to understand nuclear physics from the principles of QCD.

Although this approach is the ideal one, it is not a simple task for a variety of reasons. A nucleus is a many-body system. This alone has a multitude of technical problems associated with it, even though many simplifications can be made to make the situation more tractable [21]. To a good approximation nucleons can be considered inert, but there is an additional level of complexity in nuclei that cannot be ignored—those of collective effects. Problems become exponentially worse when a nucleus in considered in terms of QCD. In QCD, a *single* nucleon becomes a relativistic many-body system in contrast to the relatively “simple” shell model. Furthermore, because the coupling constant is large at low energies, perturbative expansion in powers of the coupling constant is only possible at highly relativistic energies (i.e. $q^2 \gg 1GeV^2$). Thus in the low energy regime, which nuclear physics is concerned with, perturbative expansions do not converge. Furthermore, in the context of QCD, nuclear binding appears more as a residual interaction, like the Van der Waal force in EM, than a fundamental interaction. In this spirit, it can be argued that the basis of the strong interaction cannot be deduced from nuclear interactions, even though QCD ultimately describes it.

At this point it is perhaps instructive to discuss the NN potential in some detail, and indicate where problems with QCD occur. A schematic depiction of the nuclear/QCD potential is given in figure 2.2. The range of the nuclear force extends beyond the spatial extension of the radius of the nucleon to several Fermi's. This region is phenomenologically well described by the One Pion Exchange Potential (OPEP), which is a good approximation in low energy NN scattering processes [22]. Moving to smaller distances, the strength of the force increases. This is understood in the nuclear environment by the contributions from higher mass mesons. Moving further into the nucleon ($r < .5$ fm), the force reaches its maximum attraction and then turns highly repulsive. This manifests itself as a saturation density in nuclei where the nuclear density is nearly constant across the periodic table ($\rho_o \sim .15 \text{ fm}^{-3}$). This repulsive nature has been parameterized in the past, rather artificially, as a hard core, or cut-off in the potential which effectively makes it inert. Because it occurs at short inter-nucleon distances, large energies, in comparison to the Fermi momentum of the nucleons within the nucleus (i.e. > 300 MeV), are needed to probe this region. Relativistic effects, isobar excitations, and three-body forces are invoked to describe these short-range correlations at the nuclear level [23].

At the other end of the energy scale, extremely high energy pp collisions, are well described by the interaction of point-like quarks. Such processes can be understood in terms of QCD, because the short range potential is extremely weak and perturbative expansion becomes reliable. As energy is decreased and inter-quark separation becomes larger, the interactions are not local among point-like particles; collective effects come into play. Phenomenologically it can be explained as the interaction of the bags confining the quarks which is highly repulsive. This (bag interactions) long range part of the QCD potential, not to be confused with the

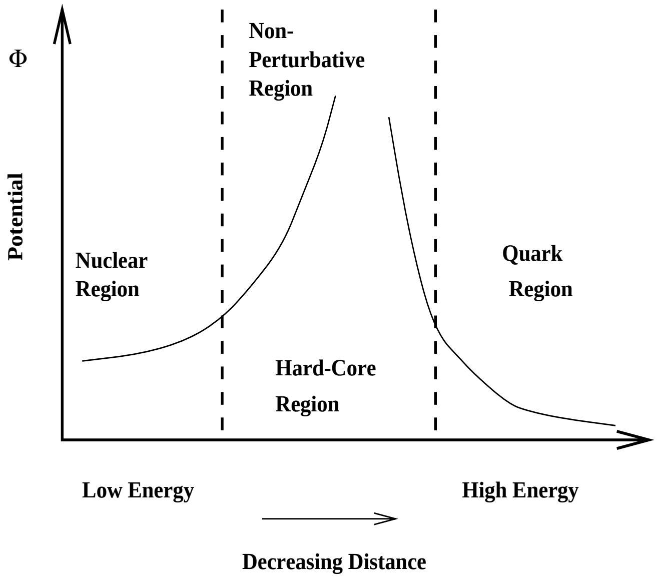

Figure 2.2: A schematic of the potential of the strong nuclear force. At relatively large distances (> 1 fm), or small energies, the force is understood in terms nucleon/meson degrees of freedom. At the other end of the energy spectrum, QCD allows a perturbative treatment and can be described in terms of quarks and gluons. In the hard-core region however, nucleon degrees of freedom do not seem appropriate and QCD does not allow for calculation—yet.

highly attractive quark-quark interaction, is the same as the short-range, hard-core region described above in the language of nuclear physics. The difference is merely semantics. No matter which description is chosen, this particular region is one of transition as nucleon and meson degrees of freedom are suitable below this point, and quarks and gluons are appropriate above it. It is for this reason that the study of this region has been termed "Quark Nuclear Physics" (QNP).

There are several ways of probing this non-perturbative region. Because leptons do not posses color, they provide an experimental avenue to decouple the strong and EM interactions. Furthermore, because the EM interaction is well understood, e^-N and γN reactions serve as useful probes to disentangle structure and reaction mechanisms. Such studies are being pursued at dedicated labs like TJNAF (formerly CEBAF) [24] and MIT-Bates [25], and there are plans to extend these programs in Europe (ELFE) [26] and Japan (SPring8) [27]. These programs all look to understand reaction mechanisms by studying few body systems, in highly exclusive channels and kinematically complete manners. This is not the only approach however, as another set of experiments— relativistic heavy ion collisions—is trying to understand this non-perturbative region with an entirely different approach. This is best illustrated by the following scenario.

Consider a generic nucleus of **A** nucleons which are composed of **Z** protons and **N** neutrons ($\mathbf{A} = \mathbf{Z} + \mathbf{N}$). At equilibrium, the density is approximately constant independent of **A**. The bulk properties of the nucleus (i.e. magnetic moment, binding energy, etc.) are well described with nucleons as the effective degrees of freedom. Now suppose external pressure is applied to the system and it is slowly compressed. As the volume decreases, the density increases and the potential, or thermodynamically speaking, the temperature, also increases. As compression continues, the NN potential eventually turns repulsive as the hard-core region is reached. Adding further energy to the system in order to overcome the repulsion, the system of **A** nucleons is compressed; eventually to the volume of a single nucleon. It certainly does not make sense to discuss such a system in terms of nucleonic degrees of freedom at this point, as they are certainly not "distinguishable",[5] and it appears that a description in terms of the nucleon's constituents—quarks and gluons—is more appropriate. Upon further compression the inter-quark distances eventually fall to zero and the system becomes an ensemble of free particles—in essence an ideal gas of quarks and gluons—a QGP.

Although at a phenomenological level, it is compelling to expect constituent degrees of freedom to become dominant at higher energies, or other suitable conditions, it is important to have quantitative predictions, but how is this possible without perturbative calculational tools, and in what situations does it make sense to talk about the thermodynamics of hadronic matter?

QCD prescribes an exact Lagrangian and this allows a partition function to be

---

[5] This is meant in the classical sense with the picture of a nucleon as an inert hard-sphere. In such a picture, nucleons cease to exist under these extreme conditions.

constructed, from which a variety of thermodynamic quantities can be calculated. In the absence of analytical solutions or approximations, this can even be done numerically. This is in fact the basis of Lattice QCD calculations [28]. These calculations have allowed a description of hadronic matter in terms of thermodynamic quantities. This is shown in figure 2.3

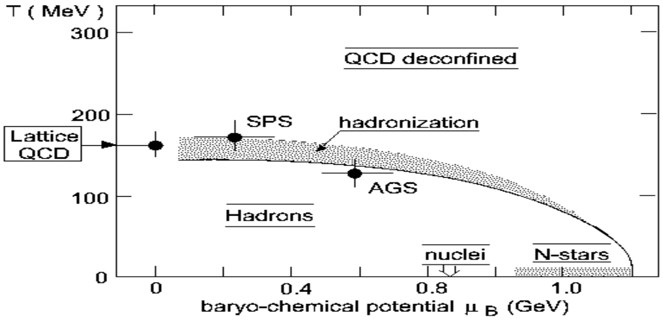

Figure 2.3: A schematic depiction of hadronic matter in the chemical potential/temperature plane. At a high enough temperature (energy density) or chemical potential (matter density), hadronic matter may undergo a phase transition where properties could be quite different. From [29].

Such calculations have unambiguously shown that a phase transition to a state with the properties of an ideal gas occurs in gluonic systems [30]. These studies have been refined to include quark degrees of freedom and the signature of a phase transition remains.

A well established result from lattice calculations is the strong dependence of the order of the phase transitions on the number of flavor degrees of freedom (number of quark species). In the absence of quarks (i.e. a pure gluon gas), the phase transition is first order if one allows for three colors. In the case of 2 distinct quark flavors (u and d), the transition seems to be second order and for $n_f \geq 3$, it appears to be first order again. The critical temperature (T_c) also varies widely from ∼150 MeV for 2 light quarks, to as high as 260 MeV for purely gluonic theories

[31]. The latter seems improbably high and may be understood by the fact that in the absence of light mesons, higher temperatures are required to excite the much heavier glueballs to overlap and produce a critical density. Nonetheless the different models outline some limits in which the phase transition is expected to occur. All lattice calculations show that at a critical temperature, there is a rapid change in the energy density as a function of pressure, and a steep increase of the specific heat and associated quantities. This is shown in figure 2.4. This is the bulk of the thermodynamic evidence for a phase transition. A phenomenological explanation of this critical temperature is presented in Appendix B [32].

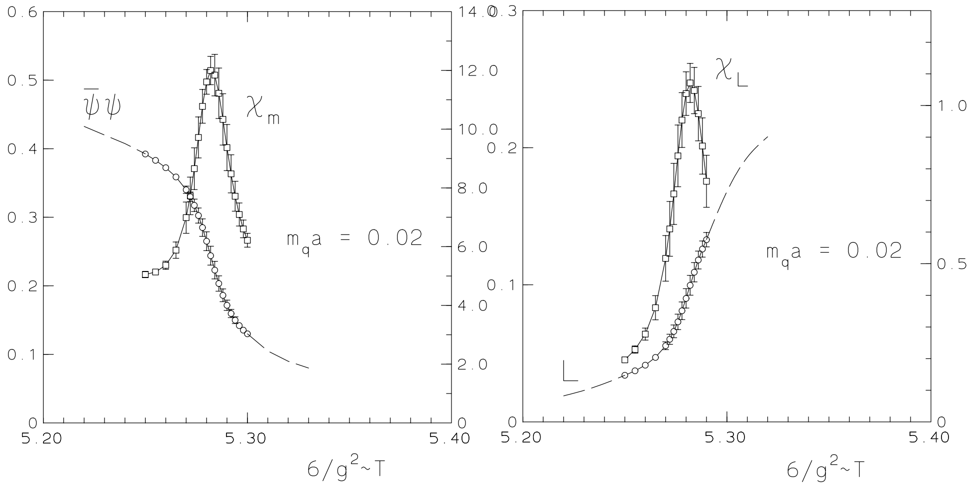

Figure 2.4: Results from lattice QCD calculations show at a certain critical temperature, hadronic matter goes through a transition in which its properties change. Shown is the is the effective quark mass scale $< \bar{\psi}\psi >$ (left) and the Wilson loop L (right) which quantifies the free quark energy. Also shown are the associated suceptibilities χ_m and χ_L. The temperature is given in units of the inverse lattice coupling constant g. Plots from [33].

2.3 Experimental Considerations

Experimentally where are such conditions expected to occur? First, the system must have a large energy density extended over a finite volume. Single particle collisions (i.e. pp or e^+e^-) are capable of the highest peak energy densities, but over very restricted volumes. Furthermore, energy deposition or stopping power of these systems is not linear with incident energy. In pp collisions, the onset of transparency, reduces the amount of “stopping” or energy deposited in the target nucleon [34]. It should also be said that in order to apply statistical methods, the system under consideration must be large. Just as it makes little sense to melt or dissolve a single molecule, it makes little sense to do the same to a single hadron in this picture. While in this respect the single particle collisions seem unsuitable, heavy ion collisions seem to be quite attractive, because there is a large energy deposition [35]. Because this energy is distributed in nuclear material, there is the possibility for the system to thermalize if the lifetime is sufficient, and a thermodynamic description may be justified. As for the relevance of thermodynamics, it is known that the transverse energy (E_T) and transverse momentum (p_T) spectra of secondary hadrons in pp collisions can be described with a thermal or Boltzman distribution [36]. Thus, within the context of such a model, the concept of a temperature may be defined.

Although heavy ion collisions seem attractive in these respects, there are still many problems in uncovering the presence (or absence) of a QGP phase since it is not an observable, unlike more familiar phase transitions around us. Therefore the presence or absence of such a state must be determined from the final state products of a collision. But, *Is it possible to separate structure and interaction in a model independent way in order to reveal this phase transition?*

In a word, no. If something is not an explicit observable, it needs to be interpreted in the context of some model. In any model, some assumption about structure and interaction is made. This implies that there probably will not exist a “smoking gun” observable or experiment, with direct evidence of plasma formation. However, supporting evidence from a variety of different observables which are consistent, yet not reconcilable with the simple picture of a super-position of NN collisions, may prove just as valuable.

2.4 What Can be Learned From Heavy Ion Collisions?

The most compelling reason to study heavy ion collisions is to understand the workings of QCD in high density environment. The transition to a plasma, if experimentally observable, has the potential to divulge much information regarding the dynamics of QCD in a medium. In this respect these studies are complementary to spectroscopy measurements on single particles [37]. The presence of a QGP phase may allow perturbative methods to be used in describing high density nuclear, or quark matter. It would also show that QCD does in fact have predictive power in the low energy region and illustrate the usefulness of lattice calculations. Similarly its absence would raise questions why QCD does not describe the low energy region. Investigations of QCD also test the concepts of non-Abelian theories and whether our theoretical understanding is correct. This has applications beyond that of the strong force—specifically quantum gravity, which, like QCD, is also non-Abelian. More speculatively, a QGP phase has implications on a wide variety of things in the universe—relic gravity waves [38], baryon inhomogeneities [39], as well as the structure of stellar objects like neutron stars, and black holes [40]. That being said, how can a phase transition be identified? There have been many suggestions from theory and several possible signatures for a transition are described below.

In a purely thermodynamic picture, a first order phase transition is seen by an increase in entropy at a constant temperature. Using simple thermodynamic relations (see Appendix C) this would manifest itself in a variation of event multiplicity with a constant mean transverse momentum. This has been one of the oldest ideas, and is based on the premise that it is possible to completely characterize an event in a thermodynamic picture. However if a strong ordered flow velocity within the source is present, this would become ambiguous. This is more fully discussed in chapter 3.

As suggested by Rafelski [41], strangeness enhancement, a consequence of the Pauli exclusion principle, is also a possible signature. The lightest hadron is the pion and as such, it is produced in the largest quantities. It is composed of the two lightest quarks, u and d. If hadronic densities become large enough, the chemical potential, or Fermi energy, of the u and d quarks can become the order of the strange quark mass (~150 MeV), since the Fermi energy is a function of the density of the system ($\epsilon_F \sim \rho^{\frac{2}{3}}$). In such a scenario, it becomes energetically favorable to thermally produce strange (s) quarks instead of the lighter flavors, with the consequence that the yield of strange hadrons increases. Strangeness enhancement should be quantifiable in a ratio of strange to non-strange hadrons (i.e. $\frac{K}{\pi}$, $\frac{\Lambda}{p}$, etc.) Such has been studied by many previous experiments and is an important component in the NA49 research program.

Opposite to strangeness enhancement is J/Ψ suppression, as suggested by Satz and Matsui [42]. The mass of the charm (c) quark is substantially higher than that of the light quarks (u, d, or s) and therefore c quarks cannot be produced thermally in a collision. The mode of production is through hard parton-parton interactions in the initial stages of an AA collision which is calculable by perturbative QCD. However, if a QGP is formed a $c\bar{c}$ pair will be unable to bind at its production point. If the deconfined phase has a significant lifetime, as it evolves, the spatial separation of the $c\bar{c}$ system may be large enough that the system will not be close enough to bind when hadronization occurs. This will increase the rate of production of open charm mesons (i.e. D mesons) and decrease the J/Ψ yield. Although it has been pointed out that charm absorption can occur in highly dense hadronic matter without the need to invoke deconfinement [43], a factor of 2 in suppression is still seen in CERN Pb-Pb collisions, and this defies conventional explanation [44].

It should also be remarked that at high energies it is believed chiral symmetry should be restored. With the restoration of chiral symmetry, the quark masses vanish. There have been indications that intermediate mass mesons (i.e. ρ) have a slightly decreased mass in heavy ion collisions [44]. Such a mass shift has been interpreted as a possible prelude to chiral symmetry restoration. It is not known whether such chiral restoration occurs with or without deconfinement or whether it is a distinct transition by itself. Nonetheless the current experimental situation is intriguing.

All the above signatures are in terms of a specific model, which is not desirable. In order to reduce the model dependency of a signature, Stock has suggested that it may be advantageous to exploit the idea of a phase transition as a critical phenomenon [45]. As such, non-statistical fluctuations may be induced in some observables. Since conditions in central Pb-Pb collisions at the CERN-SPS are marginal for QGP formation according to calculation, a QGP may not form in every event. In this scenario, it becomes necessary to measure these observables on an event-by-event basis in order to reduce the chance of diluting a signal due to event averaging. The large multiplicity of a single relativistic heavy ion collision allows each event to become statistically meaningful by itself [46]. Such a philosophy weighs heavily in the intentions of the NA49 experiment which are detailed in this thesis.

Using this philosophy, the search strategy for a phase transition becomes a two-step process. First it is necessary to characterize the average properties of the collisions. The next step is to search for fluctuations in specific observables, on an event-by-event basis (i.e. high temperature ($<\mathrm{p}_T>$), high strangeness content ($\frac{K}{\pi}$), high multiplicity ($\frac{dN}{dy}$), large source size, etc. Ensemble properties are important so as to have an idea what average conditions are, and to have some measure to compare "fluctuations" against. This is an important point as there is little theoretical guidance is specifying what constitutes "normal" conditions. To this end NA49 also includes pp and pA collisions in its experimental program. This will allow comparison of Pb-Pb collisions with a variety of other nuclei which will allow a systematic characterization of fluctuations with respect to different systems.

The following chapters will detail the characterization of the spatial-temporal extensions of the average source size created in 158 GeV A Pb-Pb collisions using particle interferometry. A method to extract a source size on an event-by-event basis will also be described. The geometric characterization of the source is an important component in understanding the evolution of a heavy ion collision, as it is required in order to realize an equation of state. Furthermore, it is possible that a first order phase transition could be deduced by such measurements. For instance, an anomalously long lifetime could signal the presence of a system that has a latent heat associated with it. If the source is also expanding, it would also have a large spatial extension. However, just as deconfined phase is not an observable, neither is the spatial (or temporal) extension of a nuclear fireball, and a suitable method for measuring subatomic distances is required–that of HBT interferometry.

Chapter 3

Interferometry and the HBT Effect

A new kind of interferometry was formulated in the mid-1950s by R. Hanbury-Brown and R. Q. Twiss for the purpose of improving the resolution of existing radio-interferometers [47]. This new intensity, or HBT interferometry, as it has come to be known, was first applied in astronomy in order to deduce the spatial extension of stars. Shortly after its development it was shown that this effect is universal and could be observed for any emitting source [48]. Its principle was first applied in particle physics by Goldhaber et al. in order to explain the angular distribution of pions in pp collisions [49]. The opening angle distribution between pion pairs was systematically different for like and unlike sign pairs. Whereas the unlike sign pairs were in agreement with expectations from purely phase-space considerations, the like sign pairs were more sharply peaked at smaller angles.

This "HBT-effect", unlike conventional interferometry which has a classical interpretation in terms of the wave nature of light, has its physics rooted in the principles of quantum statistics. In the case of bosons, there is an attraction or correlation between identical particles, whereas fermions exhibit the opposite behavior and produce a repulsion or anti-correlation between particles. Both effects have been seen experimentally and have allowed estimates of the space-time structure of subatomic collisions [50].

3.1 How is Spatial and Temporal Information Contained in Intensity Correlations?

In conventional optics, the Fourier transform of an interference pattern contains information on the spatial structure of the source (i.e. a slit pattern or a diffraction grating). Similarly, the coordinates of identical particles in momentum space contain information regarding the space-time structure of the emitting source, because momentum and position are related through canonical commutation relations. This information is contained in the symmetry properties of a multi-particle wave function. Thus unlike conventional interference where it is possible to interpret the effect as a single particle phenomena [51], the effect in HBT interferometry is manifestly between pairs (triplets ... etc.) of particles—hence the name multi-particle correlations. A simple derivation of the formalism is given below.

Consider a simple wave function of a pair of identical particles:

$$\Psi_2(p_1,p_2)=\frac{1}{\sqrt{2}}(\psi(p_1,p_2)\pm\psi(p_2,p_1)) \tag{3.1}$$

where p_i denotes the 4-momentum of the i^{th} particle. The $(-)+$ sign is for (fermions) bosons in order to account for the correct (anti-)symmetry of the wave function. This sign, as it will be shown, is the *complete* basis of the correlation! If the particles are assumed to be free, the single particle plane wave approximation may be used:

$$\begin{aligned} \psi(p_1,p_2) &\sim e^{ip_1x_1}e^{ip_2x_2} \\ \psi(p_2,p_1) &\sim e^{ip_2x_1}e^{ip_1x_2} \end{aligned} \tag{3.2}$$

where r_i is the space-time four-vector of the i^{th} particle. A two particle probability density is given by:

$$\wp(p_1, p_2) = \int_{source} d^4x_1 d^4x_2 \, |\Psi_2(p_1, p_2)|^2 S_i(x_1, p_1) S_i(x_2, p_2) \tag{3.3}$$

where $\mathrm{S}_i(x_i, p_i)$ is the source density distribution or emission function. It is the probability that a particle of type i is emitted at point x_i with momentum p_i [52]. It contains all the information necessary to completely specify the source, and can be used as to calculate any observable. For example a single particle spectrum:

$$P_1(\mathbf{k}) = E_k \frac{dN}{d^3\mathbf{k}} = E_k < \hat{a}^\dagger(\mathbf{k}) \; \hat{a}(\mathbf{k}) > \tag{3.4}$$

normalized to the total number of particles:

$$\int \frac{d^3\mathbf{k}}{E_k} P_1(\mathbf{k}) =< N > \tag{3.5}$$

is given by:

$$P_1(\mathbf{k}) = \int d^4x \, S_i(x, k) \tag{3.6}$$

and a two particle spectrum:

$$P_2(\mathbf{k}_1, \mathbf{k}_2) = E_1 E_2 \frac{dN}{d^3\mathbf{k}_1 d^3\mathbf{k}_2} = E_1 E_2 < \hat{a}^\dagger(\mathbf{k}_1) \; \hat{a}^\dagger(\mathbf{k}_2) \; \hat{a}(\mathbf{k}_2) \; \hat{a}(\mathbf{k}_1) > \tag{3.7}$$

normalized to the total number of pairs of particles:

$$\int \frac{d^3\mathbf{k}}{E_k} P_2(\mathbf{k}_1, \mathbf{k}_2) =< N(N-1) > \tag{3.8}$$

is given by:

$$P_2(\mathbf{k}_1, \mathbf{k}_2) = \int d^4x_1 d^4x_2 \, S_i(x_1, k_1) S_i(x_2, k_2) \tag{3.9}$$

Likewise, a two particle correlation function can also be constructed from the emission function, although one must be careful in blindly applying equation 3.3. The symmetry or anti-symmetry of a wave function is a product of the symmetry properties of the spatial, spin, and isospin components; that is $L+S+T=$ (odd) even for (anti-)symmetric states, where L is the relative angular momentum, S is the spin angular momentum and T is the isospin of the system. In the case of scalar or pseudo-scalar particles, the symmetry properties are given uniquely by the spatial component. Even though plane waves (i.e. e^{ikr}) are not parity, nor angular momentum eigenstates, the symmetry properties are imposed by explicity including an exchange term in equation 3.1. This is not necessarily possible for non-scalar particles. In the case of protons, both the spatial and spin wave functions may be symmetric or anti-symmetric (the isospin is fixed in the singlet state); so long as the condition $L+S+T \rightarrow$ odd holds. In this case equation 3.3 is not sufficient as one must include the spin part of the wave function in the integral. This is just a cautionary note. For scalar particle pairs, substituting the plane waves of equation 3.2 into equation 3.3 results in:

$$\begin{aligned}\wp(p,p^{'}) = &\int_{source} d^4x d^4x^{'}\, S(x,p) S^*(x^{'},p^{'}) \;\pm \\ &\int_{source} d^4x d^4x^{'}\, S(x,p) e^{iq\cdot x} S^*(x^{'},p^{'}) e^{-iq\cdot x^{'}} \qquad (3.10)\end{aligned}$$

where $q = (p - p^{'})$ is the *relative* four-momentum of a particle pair. Examining the above shows that the first term is the product of two single particle spectra, and the second term is the square of the Fourier transform of the source density, which contains the spatial-temporal information sought after. Dividing equation 3.10 by the single particle spectra (Eqn. 3.6) gives an expression for the correlation function:

$$C_2(p,p^{'}) = 1 \pm \frac{\int_{source} d^4x d^4x^{'}\, S(x,p) e^{iq\cdot x} S^*(x^{'},p^{'}) e^{-iq\cdot x^{'}}}{\int_{source} d^4x d^4x^{'}\, S(x,p) S^*(x^{'},p^{'})} \qquad (3.11)$$

For bosons the correlation is seen as an “enhancement” in the two particle spectra as compared to the single particle spectra–or an uncorrelated background. Thus we have:

$$C_2(\mathbf{k}_1, \mathbf{k}_2)_{theory} = \frac{< N >^2}{< N(N-1) >} \frac{\tilde{P}_2(\mathbf{k}_1, \mathbf{k}_2)}{P_1(\mathbf{k}_1)P_1(\mathbf{k}_2)} \tag{3.12}$$

where the $\tilde{P}$ denotes the Fourier transform of the two particle distribution. This can be simplified, and the correlation function can be written as:

$$C_2(q, K) = 1 \pm \frac{\mid \int_{source} d^4x\, S(x, K)e^{iq\cdot x} \mid^2}{\mid \int_{source} d^4x\, S(x, K) \mid^2} \tag{3.13}$$

where $\mathrm{K} = \frac{1}{2}(\mathrm{k}_1 + \mathrm{k}_2)$, the average momentum of the particle pair.

Up until this point the derivation has been model independent, exploiting only general symmetry properties of identical particles and statistics. However, the correlation function measures the magnitude of a normalized Fourier transform of the emission function, not its value at every point. Thus a given emission function characterizes a source completely, but an experimentally determined correlation function does not uniquely determine an emission function. Therefore, in order to extract a parameterization of the emission function, some assumptions regarding its shape are necessary. This can be understood more intuitively by the following argument. In order to completely characterize a generic source it takes no less then ten independent parameters—three for the spatial extension, three Euler angles for its orientation, three independent velocity components, and one temporal extension. A pair of particles has only six independent degrees of freedom in momentum space—the relative (**q**) and average (**K**) components. Therefore it becomes necessary to work within the context of some model to interpret the spatial information contained in a correlation function.

3.2 Application of HBT in High Energy Physics

Although any kind of particle species can be used for intensity interferometry, the usual choice in high energy physics is charged pions. This is done for several reasons. First, because the pion is the lightest meson, they are produced in the largest quantities. This is important from a standpoint of statistics because the number of pairs per event is proportional to the square of the multiplicity. Second, charged particles are much easier to detect than neutrals, which reduces the experimental difficulties. The reason negative pions are preferable is because the initial state contains a large number of protons. At high energy, they can be misidentified as pions and since the HBT effect is due to the quantum statistics of identical particles, such misidentification will dilute the real correlations. It should be mentioned that photons also suffer this type of contamination in high energy physics processes because of the decays of π^0's (the most prolific source) and vector mesons. However, unlike photons, charged particles are subject to Coulomb effects and final state interactions which cannot be neglected. This will be discussed in detail in chapter 5.

3.3 Extraction of Source Geometry

The spatio-temporal information is contained in the width of the correlation function, and this must be quantified in some manner. The simplest parameterization one can use for the correlation function is that of a single variable in Q_{inv} of the form:

$$C_2(q) = 1 + \lambda e^{-Q_{inv}^2 R_{inv}^2} \tag{3.14}$$

where $Q_{inv} = (p_1 - p_2)$. It should be noted that another parameter—λ—has been added in order to characterize the correlation strength. It is sensitive to the effects of source coherence, impurity in particle species, resonance effects and a host of other effects [53]. Experimentally the need for this parameter is illustrated by the fact that the correlation function is somewhat less than the maximum theoretical value of 2 at $Q_{inv} = 0$, as illustrated in figure 6.11.

This parameterization has been applied to high-energy e^+e^-, pp, and $p\bar{p}$ collisions, where a value of $R_{inv} \sim 1$ fm was found [54, 55]. This was found to be independent of the nature of the particles and virtually independent of the incident energy. Since Q_{inv} convolutes spatial and temporal information in a non-trivial way, R_{inv} is not simple to interpret. However the invariance of R_{inv} seems to suggest that the underlying space-time structure of the collision region does not change in these systems.

The first heavy ion collisions at the Bevalac did show an increase in the source size—or at least in R_{inv}—over that of single particle collisions [56], It was found that 1.8 GeV A $^{40}Ar - Pb_3O_4$[1] interactions produced a system with $R_{inv} \sim 3$ fm. An increase over that of pp was expected owing to the larger size of projectiles involved in these collisions, and this increase was also observed at BNL and the CERN-SPS [57], however another puzzle soon surfaced. It was observed that the size remained essentially constant (at ~ 4.5 fm) from BNL to SPS energies. It was known that the radius parameter was a strong function of the incident projectile size and even though there was a negligible difference between the sizes of projectiles at BNL to CERN (^{28}Si $\rightarrow ^{32}$S), the energy difference was of the order of a factor of 20. With these considerations, it seemed that a saturation size had been reached.

This was answered when the "5 fm threshold" was finally broken when 158 GeV A Pb beams were accelerated in December of 1994 at the CERN-SPS. The measured HBT spectra showed sources with a size of ~ 6 fm, as shown in figure 6.11. The statistical power of the events is striking and as such, present heavy ion experiments allow highly differential measurements of all observables, including correlation functions. For correlation studies this has meant investigations into the different spatial extensions of the source—the transverse and longitudinal directions—as well as systematic studies on the variations of parameters with rapidity and transverse

---

[1] and BaI_2

momentum (K_T) of the pair. This has allowed characterizations of different spatial-temporal regions within the source as well as dynamical properties like collective flow and expansion [58].

In order to look at the different "sides" of the source, it is necessary to decompose Q_{inv} into different components. This is formulated by assuming a Gaussian form for the emission function [59]:

$$S_i(x,K) = S_i(\bar{x},K)\, e^{-\frac{1}{2}\bar{x}^{\mu}\bar{x}^{\nu}\ B_{\mu\nu}(K)} + \delta(x,K) \tag{3.15}$$

where **B** is a tensor and characterizes the space-time variances of the emission function:

$$(B^{-1})_{\mu\nu} =< x_{\mu}x_{\nu} > - < x_{\mu} >< x_{\nu} > \tag{3.16}$$

and δ(x,K) represents the deviation from Gaussian behavior. If this term is neglected, the correlation function can be written as:

$$C_2(q) = 1 + \lambda e^{-(B^{-1})_{\mu\nu}\ q^{\mu}\ q^{\nu}} \tag{3.17}$$

It seems reasonable that event averaging allows one to make the assumption of an axial symmetric source (i.e. $S_i(x,K)$ is invariant under $y \to -y$) [60]. With such a premise, substituting equation 3.15 into equation 3.13, a form, first suggested by Bertsch[61] and refined by Chapman and collaborators [60], is realized:

$$C_2(q) = 1 + \lambda e^{-(Q^2_{Tout}R^2_{Tout} + Q^2_{Tside}R^2_{Tside} + Q^2_L R^2_L + 2Q_{Tout}Q_L R^2_{OL})} \tag{3.18}$$

In this parameterization it is possible to differentiate between the longitudinal and transverse directions. Here R_L is the direction along the beam (z); and the other two terms denote the transverse directions—R_{Tout} being parallel to the pair transverse momentum and R_{Tside} perpendicular to both. By convention, R_{Tside} is always taken to be positive. A schematic of this decomposition is given in figure 3.1.

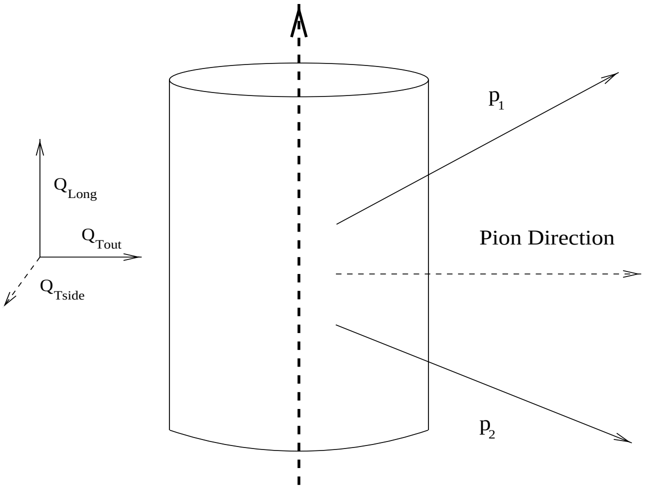

Figure 3.1: Schematic of a cylindrically symmetric source. The dashed arrow denotes the beam direction and and longitudinal direction. The "out" direction is parallel to the transerve momentum of the pion pair.

In general the correlation radii also depend on other variables like rapidity and transverse momentum of the pair, because the emission function also has these dependencies. The cross-term (R^2_{OL}) is a non-trivial factor that does not owe its existence to the choice of reference frame in which the correlation function is constructed, but rather measures the asymmetry of the source in the longitudinal and transverse directions. In general, two other cross-terms also exist (i.e. R^2_{SL} and R^2_{OS}). However, they vanish in the case of an axial symmetric source. They are expected to be non-zero in single event correlation functions if the interaction is not perfectly central. The parameters in equation 3.18 have the following interpretation (to first order):

$$R^2_{Tside} =< y^2 > - < y >^2 = R^2$$
$$R^2_{Tout} =< (x - \beta_o t)^2 > - < x - \beta_o t) >^2 = R^2 + \beta_o^2 (\delta t)^2$$
$$R^2_L =< (z - \beta_l t)^2 > - < z - \beta_l t) >^2 = l^2 + \beta_l^2 (\delta t)^2$$
$$R^2_{OL} =< (x - \beta_o t)(z - \beta_l t) > - < x - \beta_o t >< z - \beta_l t) >= \beta_o \beta_l (\delta t)^2 \quad (3.19)$$

A static source would have no time or velocity dependence and the parameters could then be interpreted in a purely geometric fashion. The time and velocity dependences become manifest in collisions because of the dynamics of the created source. As such the radii parameters can only be interpreted over limited "regions of homogeneity" [63] where the source appears stationary and position-momentum correlations are negligible. In this scheme, it can be seen from equation 3.19 that R_{Tside} contains only spatial information while the remaining terms convolute the spatial-temporal information. The differences of the squares of the transverse radii is directly proportional to the particle emission duration. The cross-term is also sensitive to this. However because it is sensitive to x-t and z-t correlations, it disappears at mid-rapidity (it is odd in z!), and should change sign in the backward rapidity region. No such measurement exists in this region. It also disappears everywhere in the case of a boost invariant source. This spatial-temporal convolution allows the measurement of an ordered expansion within the source by observing the evolution of the radii with the momentum of the correlating pair. This complication necessitates the interpretation of correlation radii in the context of some model [64].

A simple model of an evolving source is one that is longitudinally boost invariant; that is, the longitudinal velocity of the source, (β_l) is zero. In this case a convenient observation frame is the Longitudinal Co-Moving System (LCMS), and it will be used in this thesis. In this reference frame the longitudinal pair momentum (K_L) vanishes. There are three relative momentum coordinates defined; one in the longitudinal direction (Q_L) and two in the transverse directions (Q_{Tside} and Q_{Tout}):

$$\begin{aligned}
Q_L^2 &= M_{inv\perp}^2 - m_{1\perp}^2 - m_{2\perp}^2 - 4m_{2\perp}m_{2\perp} \\
Q_{Tout} &= \frac{P_T \cdot Q_T}{|P_T|} \\
Q_{Tside}^2 &= Q_{Tout}^2 - (\frac{P_T \cdot Q_T}{|P_T|})^2
\end{aligned} \tag{3.20}$$

where $m_{i\perp}^2 = E_i^2 - p_{zi}^2$, $P_T = \frac{1}{2}(\mathbf{p}_{T1} + \mathbf{p}_{T1})$, and $Q_T = \mathbf{p}_{T1} - \mathbf{p}_{T1}$. The three momentum of a particle is specified by $\mathbf{p}_i$ and its transverse momentum by $\mathbf{p}_{Ti}$.

Although the indistinguishability of the particles making up any pair makes the sign of $\mathbf{q}$ insignificant, in order to define the sign of the cross-terms, Q_{Tside} will be defined to be positive. Model studies have shown that longitudinal boost invariance precludes the existence of a cross term [60]. Thus the radii parameters can shed some light on the structure of the source. Strictly speaking, a finite source can never be completely boost invariant, as this would predict a completely flat $\frac{dN}{dy}$ distribution. This however, is known to be peaked about mid-rapidity [62].

It should be noted that the parameterizations presented thus far presuppose the shape of the source to be Gaussian in profile. This is a rather strong assumption and it need not be made. With the increasing experimental precision of correlation functions, it is becoming feasible to characterize the non-Gaussian behavior of the source in a quantitative manner. It is believed that this non-Gaussian behavior is due to pions produced from long-lived resonances [67]. At this point it is instructive to look at the different ways pions are produced.

Pions are produced dominantly through resonance de-excitation. Short-lived resonances (, $>$50 MeV), decay within the source region, and as such will carry information regarding the emission function. Long-lived resonances (, $\ll$1 MeV) can propagate several *cm*s from their production point. Because this distance can not be resolved on an MeV scale (i.e. the momentum resolution of current detectors), these merely contribute to the overall normalization of the correlation function (i.e. the λ parameter), and not its width. The real problem comes from the resonances that lie between these limits. For example the ω meson (, = 8.4 MeV) may contribute significant exponential tails to the emission function and seriously distort its shape. Thus in some way, the shape of the correlator may contain information on the relative production rate of certain vector mesons. Two problems are obvious: the extraction of radii parameter by a “shape independent” method, and the quantification of its shape.

This can be done by numerically calculating the second order q moments (variances) instead of fitting them with a Gaussian function [67]. For an arbitrary correlation function, these second order "q" moments (i.e. $< q_i^2 >$) can be written as:

$$< q_i q_j >= \frac{\int d^3\mathbf{q}\, q_i\, q_j\, [C(q,K)-1]}{\int d^3\mathbf{q}\, [C(q,K)-1]} = D_{ij}^{-1}(K) \qquad (3.21)$$

Such an expression is always defined and always converges. It has a well defined error, and no dependence on a fitting algorithm.[2] Furthermore, if the source is symmetric, odd moments (i.e. $< q^{2n+1} >$ where n=0,1,2...) should always vanish. The deviation from a Gaussian profile can also be extracted from calculation of higher order moments. This is quantified in the variable G_i:

$$G_i = \frac{< q_i^4 >}{3 < q_i^2 >< q_i^2 >} - 1 \qquad (3.22)$$

where G_i can be calulated for any component (projection) of a radius parameter. If the correlation function is Gaussian in form, G_i will vanish and the radii extracted from a fit and the integral methods should be identical. If the correlation function deviates from a Gaussian profile, there may be further information than can be extracted from the value of G_i. In particular, it has been postulated that such deviations may give a way to estimate the amount and effect of long lived resonances in the correlation function [68]. However, little theoretical guidance is available regarding this at present.

Although this method allows a characterization of the radii parameters in a shape independent way, it is not the case for the correlation strength or λ parameter. In order to extract this value with an integral method, some assumption regarding the value of the integral of the 0^{th} order moment must be made. If a Gaussian ansatz is made, λ is given as:

$$\lambda = \frac{\sqrt{\det \mathrm{D}}}{\pi^{\frac{3}{2}}} \int d^3\mathbf{q}\, [C(q,K)-1] \qquad (3.23)$$

---

[2] Now the dependence rests on an integration algorithm.

One must be cautious in the interpretation of λ with this method as a large value for G_i would seem to invalidate the assumption of a Gaussian form. Nonetheless, all the information derived from fitting a correlation function with a Gaussian is available with this new method.

Chapter 4

The NA49 Experiment

4.1 Conceptual Design of NA49

NA49 was foreseen as the experiment to extend upon the investigations of hadron production from relativistic heavy ion collisions which had been instigated by NA35. This experiment measured collisions of intermediate mass ions in the first phase of the heavy ion program at CERN (1986-1990) with a streamer chamber, which is an optical imaging device. This facilitated track reconstruction over large regions of phase space. Although the streamer chamber performed well, it was at its working limits and it was clear that it would not be able to handle the increased multiplicity expected in 158 GeV A central ^{208}Pb-Pb collisions ($\sqrt{s} \sim 18$). A new experimental apparatus was needed.

Calculations suggested that central Pb-Pb collisions would create conditions at or near the threshold where a QGP was expected to form, and this greatly influenced the manner in which NA49 was designed [46]. It should be made clear, that while studying the dynamics and behavior of dense nuclear matter is still an objective of heavy ion physics, the main focus of the field, at this time, is the search for the phase transition of nuclear matter to a QGP; NA49 was designed with this goal clearly in mind.

Because NA49 was foreseen to do studies of hadronic production in heavy ion collisions on an event-by-event basis, it was necessary to have a large acceptance detector. It was established in NA35 that symmetric colliding systems are reflection symmetric about mid-rapidity [69]. Thus in order to extract complete physics information, at least 50% of the total phase space needs to be covered. In order to deduce information on production of specific particle species (i.e. kaons, pions, protons, etc.), it is also necessary to have Particle IDentification (PID) capabilities. This requires the complete determination of a particle's four-momentum. The spatial components of the momentum can be deduced by measuring the curvature of a particle's trajectory in a magnetic field, as in NA35. This necessitates some sort of tracking detector. To complete the PID, a further measurement of the mass, energy, or velocity, is required. Since tracking chambers work by collecting a charged particle's ionization, this could be carried out by a measure of a particle's specific energy loss or $\frac{dE}{dx}$. However, in fixed target experiments, most of the produced particles are highly relativistic (i.e. $\beta\gamma \gg 1$). In such a case, the specific energy loss is a weak function of its velocity (see figure 5.6). Furthermore, since ionization is a statistical process, many individual measurements, over a long track length must be made to ensure high precision [70]. The length scale of the detector was essentially determined by the requirement the experiment should have the ability to measure the $\frac{K}{\pi}$ ratio at mid-rapidity. Simulations had shown that in order to separate pions and kaons in this region (5-10 GeV/c), a specific ionization measurement with 4% resolution was required. This implied a track length of at least 3.5 m [71]. This resolution requirement puts rather stringent constraints on the performance requirements of the electronics for the experiment, as well as limits on the tolerable fluctuations in environmental conditions. Furthermore, because the track density in the aftermath of a Pb-Pb collision is very high (i.e. $\frac{dN}{dy}|_{mid} \sim 300$), the granularity of the detector must be quite fine, implying a large number of electronic channels. Although these are quite daunting technical requirements, they are well suited to the capabilities of the Time-Projection-Chamber (TPC). These devices are able to track very efficiently and carry out PID through the measurement of $\frac{dE}{dx}$ in a wide range of experimental conditions and over large volumes of phase space.

The philosophy taken in the design of NA49 was to have several highly segmented detectors, each optimized to do a specific job. The best PID would be done with TPCs operating in a field free region forward of mid-rapidity. This had been shown to be feasible in NA35 [72], and NA36 [73]. Momentum information would be deduced by placing these chambers downstream of a magnetic field. Positioning chambers a large distance from the target would have the added benefit of reducing the particle track density in the detectors. In order to facilitate the reconstruction of neutral strange hadrons (i.e. Λ, K^o, etc.), which have a $c\tau$ of the order of centimeters to a few meters, a smaller chamber was to be located inside the magnetic field. Such a chamber would have a finer granularity in order to cope with the higher track density closer to the target. Furthermore, tracking capabilities within a magnetic field allow the momenta of charged particles to be deduced directly from the curvature of the tracks. This chamber was situated so that it would cover rapidities forward of mid-rapidity ($y \geq 2.9$). These detectors would cover the necessary 50% of phase space. However, because it was foreseen to investigate pp and pA collisions for comparison with the Pb-Pb interactions, it was also desirable to cover part of the backward hemisphere. Thus a second chamber was added inside the magnets closer to the target. It covered rapidities down to $y \sim 1.5$. The primary use of this chamber was foreseen to be the study of HBT correlations in the backward rapidity region. However, its proximity to the target gave it a large acceptance for both low momentum and high p_T tracks, which makes it useful for the study of single particle spectra. It also opens up the possibility of looking for protons and deuterons with $|\mathrm{x}_F| > 1$. Adding to the tracking capabilities of the experiment also increased the resolution attainable for specific ionization measurements.

4.2 The Accelerator

NA49 is located in the North Area on the CERN-SPS H2 extraction beam line which is capable of delivering both protons and ions to the experimental area at a variety of energies. The maximum possible energy is 158 GeV A for Pb ions and

450 GeV for protons.

A schematic of the accelerator machinery that produces the Pb beams is shown in figure 4.1. Although most of the existing infrastructure at CERN was used or adapted to facilitate Pb acceleration, some upgrades were necessary in order to cope with the properties of Pb ions. CERN had previously accelerated fully stripped ^{16}O and ^{32}S to an energy of 200 GeV A. In order to produce ^{208}Pb beams of comparable energy with the existing circular accelerators, it was necessary to utilize the most favorable charge to mass ratio, which implies the use of fully stripped Pb (i.e. Pb^{82+}). Fully stripped ions place stringent requirements on the vacuum system as charge exchange reactions with residual gas molecules are the greatest threat to the lifetime of ion beams [74]. This is most serious with low speed projectiles and as such implies that losses will be minimized if acceleration is rapid.

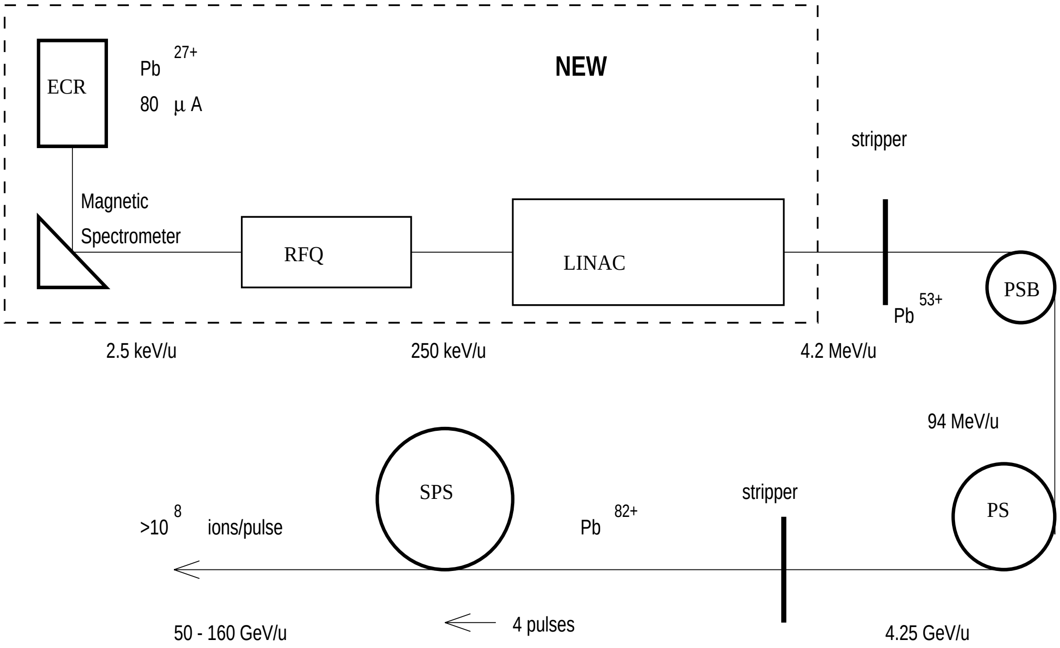

Figure 4.1: A schematic of the Pb ion accelerator complex at CERN.

Although it is possible to produce $^{208}Pb^{82+}$ in a single process, for practical utilization in an accelerator appreciable current is required. A design goal of 10^8 ions per spill was set, so 6-8 heavy ion experiments could operate simultaneously. For this purpose, an Electron Cyclotron Resonance (ESR) source was chosen [75]. Although it was able to deliver the necessary high currents ($\sim$ 2-3 mA), the most probable charge state it produced was $^{208}\mathrm{Pb}^{27+}$, which meant that further stripping, and its associated losses, was necessary. This charge state was selected with a magnetic spectrometer for delivery into the first acceleration stage. At the time, the existing LINear ACcelerator (LINAC), which was used as an injector the the CERN Proton Synchrotron Booster (PSB), did not posses the dynamic range to cope with the low charge to mass ratio of the Pb ions ($\frac{e}{m} = .13$ as compared with .375 for $^{32}\mathrm{S}^{16+}$, and 1. for $^{1}H^{1+}$). A new LINAC, with higher operating gradients was designed and constructed in collaboration with outside institutions [76]. The new LINAC and Radio Frequency Power Supply (RFQ) allows $^{208}Pb^{27+}$ acceleration to 4.2 MeV A, at which point the ions are passed through a thin Al foil for stripping before injection into the Proton Synchrotron (PS). The most probable charge state that emerges from this stripper is $^{208}\mathrm{Pb}^{53+}$. It is noteworthy that the stripping all occurs external to the circular machines as they do not possess the dynamic range to handle such operations internally. In the higher charge state the ions are then injected into the PSB, where they emerge with an energy of 94 MeV A and then into the Proton Synchrotron (PS) where energy reached 4.25 GeV A. The vacuum, after the PS, was measured as low as 8×10^{-10} Torr (gauge). At this point, the ions are passed through another Al foil and emerged fully stripped, before being injected into the Super-Proton Synchrotron (SPS). After acceleration to 158 GeV A, the ions are extracted at one of the two extraction points—the North and West areas.[1] The entire Pb spill was stretched over 5280 ms of the 19.2 s super cycle, which gives a duty factor of nearly 28%.

---

[1] the West Area was closed at the end of the 1996 run.

4.3 The Experimental Apparatus

The NA49 experimental apparatus is shown schematically in figure 4.2. The main components are 4 large volume Time Projection Chambers (TPCs). Two of them, so called Vertex TPCs (VTPC), are located in separate large aperture super-conducting dipole magnets (the CERN Vertex Magnets (VM)–hence the name VTPC) placed directly adjacent to one another, while two, much larger chambers or Main TPCs (MTPC) are located just downstream of the second VM in a field free region. The TPCs facilitate charged particle tracking and momentum reconstruction as well as PID via specific energy loss measurements ($\frac{dE}{dx}$). Their overall dimensions are specified in table 4.1.

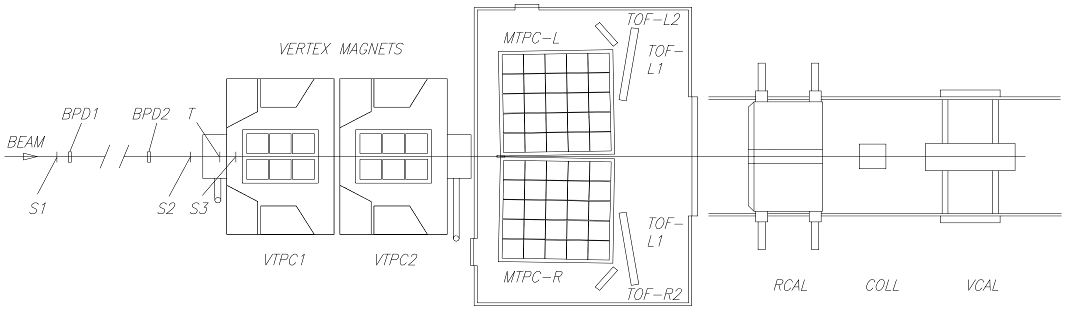

Figure 4.2: The NA49 Experimental Apparatus showing the target T, the VTPCs within the magnets, the MTPCs, the TOF system, and calorimeters. The MTPCs are 4×4 m^2 to give an indication of the size of the experiment.

NA49 TPC Dimensions		
TPC	VTPC	MTPC
Height (cm)	72	129
Length (cm)	260	384
Width (cm)	200	384
Drift Length (cm)	66	115

Table 4.1: Physical dimensions of the NA49 TPCs.

PID capabilities are augmented for particles of momentum $\leq$10 GeV/c with Time-Of-Flight (TOF) walls located just downstream of the MTPCs. There are two calorimeters: a ring calorimeter (RCAL), which is able to measure transverse energy over a small yet finite region of pseudo-rapidity[2] and a veto-calorimeter (VCAL) which is sensitive to forward energy and provides a convenient trigger [77]. These components along with the beam counters S_1, S_2, and S_3 are described in section 4.6. There are also two position calibration systems. The one which monitors the beam position consists of two orthogonal planes of Si-strips upstream of the target (BPD1 and BPD2). The second is a laser system which is able to produce tracks in any of the TPCs for distortion measurements and corrections as well as drift velocity monitoring [78].

4.4 The NA49 TPCs

A TPC is based on the same principles as a drift chamber which itself is a development of the Multi-Wire Proportional Chamber (MWPC) [79]. In the case of a TPC, however, the drift length is extended to the order of meters, instead of centimeters, and as such it is ideally suited for covering large volumes. Because it is able to determine the 3-dimensional spatial coordinates of a particle's trajectory, it is sometimes referred to as an electronic bubble chamber. As seen in figure 4.3, a TPC can be separated into three separate components—a containing vessel (gas box), field cage, and read-out chambers.

A charged particle traversing the TPCs active volume, defined by the field cage, produces electrons and ions through ionization processes in an appropriate medium. This medium is usually a gas although cryogenic liquid TPCs also exist [80]. This ionization is swept toward a readout plane under the influence of a homogeneous electric, or drift field produced by the field cage. The readout plane is constructed much like a conventional MWPC, and schematically shown in figure 4.4. A system of anode and field shaping wires are strung above a segmented cathode plane. This

---

[2] $2.1 < \eta < 3.4$ in dedicated calorimeter runs where the target is placed 6.5 m upstream of calorimeter.

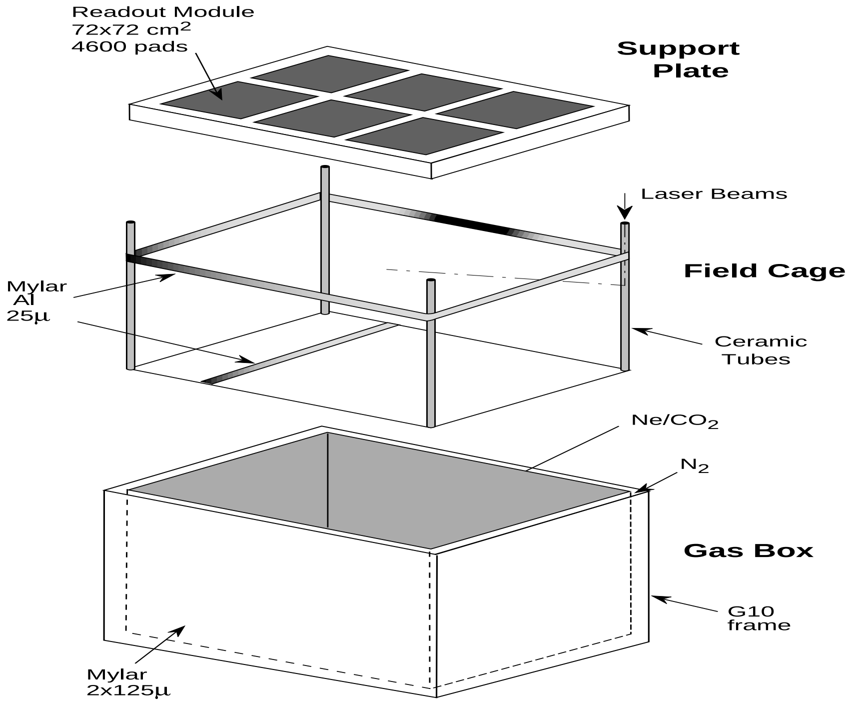

Figure 4.3: A schematic of VTPC showing the three main components of the TPC—the read-out modules, the field cage, and the gas box.

cathode plane is made up of electrically isolated "pads" which are capacitively coupled to the sense wires. Electrons produced by ionizing tracks in the active volume of the TPC drift towards the anode wires and are multiplied in the avalanche process. The movement of the *positive* ions, produced in this avalanche, away from the anode wires, induces a signal on the cathode pads. The localization of this signal on the pad-plane provides two of the three spatial coordinates of a charge cluster (a point on a track). The third coordinate can be deduced from the time it takes the electrons produced by the charged particle traversing the TPC to reach the sense wires.

Although they are not fast detectors and cannot handle high event rates, TPCs have proven to be extremely efficient tracking devices which can easily cover large regions of space. They have performed very well in a wide variety of experimental conditions, examples of which include those at e^+e^- colliders such as PEP-4 [81] and LEP [82]. More recently, TPCs have been shown to be very effective in the high track density track environment of heavy ion collisions as shown by the pioneering EOS collaboration [83], and later by NA35 [72], and NA36 [73].

In the case of NA49, owing to reasons of mechanical stability and construction tolerances, the TPCs have their readout chambers segmented into 72×72 cm^2 modules—6 for each VTPC and 25 for each MTPC. Gravitational effects of wire sagging as well as electrostatic displacement become a concern if the wires are strung over a distance exceeding 1 m. A schematic of the layout of the wire planes in the readout chamber is illustrated in figure 4.4. The grid situated closest to the pad plane contains two types of wires: sense wires, where the amplification occurs, and field wires which shape the electric field lines and decouple adjacent sense wires. The tungsten (W) sense wires ($\phi = 20\mu$m) are inter-spaced with copper-beryllium (CuBe) ($\phi = 125\mu$m) field shaping wires. Both are gold plated. The sense wires are operated at a voltage of $\sim$ 1 kV in proportional mode. This relatively low amplification voltage allows an effective measure of the specific ionization of tracks crossing the chamber, while enhancing the stability and reducing aging effects of

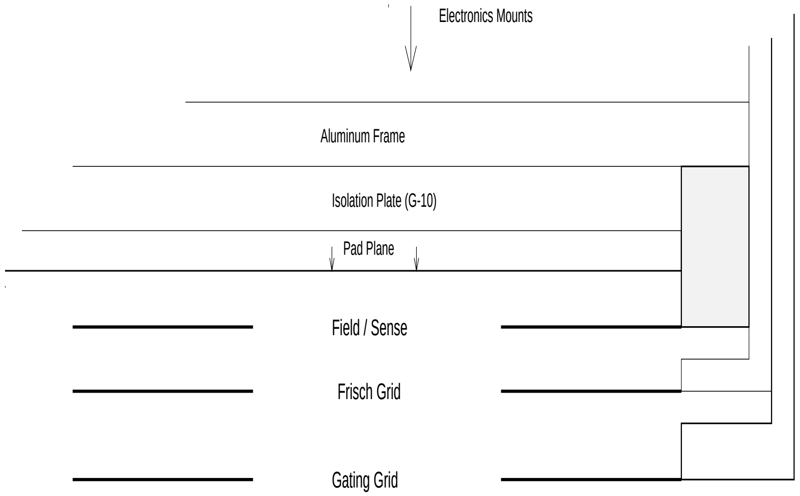

Figure 4.4: A schematic of the wire planes on a readout chamber.

the chambers. The next plane is the Frisch Grid (FG) which is also made of CuBe ($\phi = 75\mu$m) wires. They are at zero potential and serve to separate the drift region from the proportional region. They also serve as a sink to drain the charged ions produced in the amplification process. The next layer of wires is the Gating Grid (GG) (also CuBe, $\phi = 75\mu$m). Its function is to prevent the positive ions, created in the avalanche process at the sense wires, from drifting back into the active region of the chamber. If such a process was left unchecked, the accumulation of space-charge has the potential to cause electric field distortions, which can degrade the position resolution of the device. This is an important consideration in all TPCs but especially for those in an environment of heavy ion collisions where the large number of tracks produces a large quantity of ionization within the chamber. When the gate is open (during event acquisition), the GG wires have a potential such that the field lines of the drift field terminate on the sense wires themselves. In this mode the grid is said to be transparent. Once an event is completed, the gate is switched so that the drift field lines terminate on the GG wires. In this case the ionization can not pass through the gate, from either direction. Electrons from ionization within the chamber will be collected on the GG, and the ions produced in the amplification will be deposited on the FG.[3] The design of the GG is crucial to the successful operation of the chamber. The switching voltages must be chosen precisely so as not to distort the drift field, while allowing the highest possible transmission of the produced ionization. Furthermore switching must be done quickly, so as not to introduce a time dependence in the transmission of ionization through the gate, which will adversely affect ionization information ($\frac{dE}{dx}$). However, during this rapid switching of the GG potentials, a premium is placed on impedance matching because any oscillation in the circuit will be picked up on the pads, increasing the noise. Because of this the data in the first 4 time bins (i.e. .5 cm) of the chambers are lost.

The signal that is developed on the cathode pads can be parameterized by a Gaussian, both in the time and pad directions [85]. The form of the Pad Response

---

[3] A detailed discussion of wire grids is contained in [84].

Function (PRF) will be revisited in chapter 5. It can be a function of many parameters: the voltage on the sense wires, gas properties, pad geometry, sense wire-pad plane spacing, electronics response, as well as track crossing and dip angle of the track creating the ionization. As such the geometry of the wire-planes and pad layout must be optimized depending on location within the detector and expected track density. The pads are inclined at an angle with respect to the beam-line such that they follow the average horizontal deflection of the tracks due to the magnetic field. In VTPC1 pads are inclined from 5-55^o increasing with the distance from the beam line while for VTPC2 the angular range is 3-20^o. In VTPC2 the pad width measured along the pad direction is constant. Although this results in a constant pad response width, it also introduces a slight dependence on the pad area (i.e. $\frac{1}{cos(\alpha_{pad})}$). Although not a problem in VTPC2, the angles in VTPC1 mean that a similar design would result in pads that differ in area by nearly a factor of 2! In order to overcome this, the pads were designed to be of constant area, such that the width decreases with increasing distance from the beam-line. The optimization of the pad-plane geometry is detailed elsewhere [86]. The sense-wire/pad-plane distance was designed in such a way that a signal develops over ~3 adjacent pads. This allows the use of the specific gravity method (or fitting of a three parameter PRF) to determine the position of each cluster. These methods increase the position resolution of a “charge cluster” to better than that of the dimension of a single pad. Making the cluster too large increases the occupancy of the chamber. These two considerations must be optimized. The optimization of the PRF is extremely important because it is intimately tied to the position resolution of clusters and this ultimately affects momentum and Two-Track Resolution (TTR).

All together the TPCs contain a total of 181254 channels, which are distributed as described in table 4.2. Because of the large number of channels and high multiplicity, it is not feasible to read out both the pads and wires as is done in most TPCs [87]. Rather, following an idea pioneered by EOS [83], only the signals induced on the pads are read out and recorded. It is important to note in this case that both the tracking and $\frac{dE}{dx}$ information is deduced from the pad information. An example of the signal induced on a pad is seen in figure 4.5.

NA49 TPC Read-Out Sector Geometry				
	VTPC1	VTPC2	MTPC (HR)	MTPC (SR)
No. of Sectors	6	6	25	25
Pad rows per Sector	24	24	18	18
Pads per row	182-192	192	192	128
Pad Width (mm)	3.0-3.5	3.0	3.13	4.95
Pad Length (mm)	16/28	39	39	39
Sense wire/pad plane gap (mm)	3	2	2	3
Channels	26886	27648	63360	63360

Table 4.2: The NA49 Read-Out Chamber Geometries.

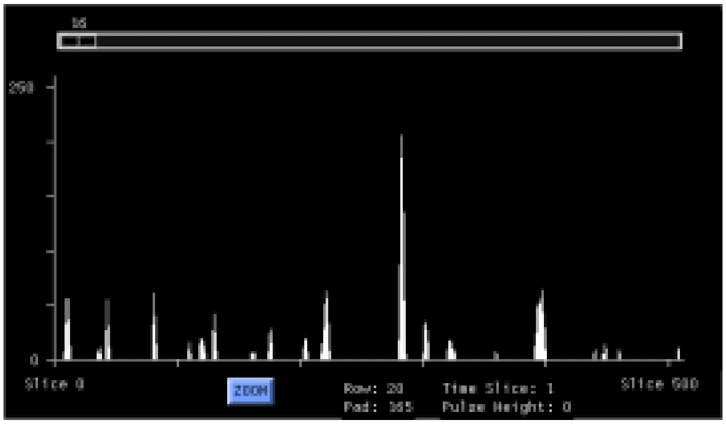

Figure 4.5: Signals induced on a pad in VTPC2 in a real Pb-Pb event. Each peak corresponds to a charge cluster; those at slice 0 occur at the top of the chamber (i.e. zero drift length) while those at large times (slice) are nearer the bottom of the chamber.

4.4.0.1 TPC Construction

All NA49 TPCs are constructed of the same materials, but they differ slightly in design owing to the different environments in which they are embedded. Even though high pressure drift chambers minimize diffusion effects, the chambers were designed to run at atmospheric pressure[4] for several reasons; this negated the need for a pressure vessel, minimized the amount of matter in the path of the produced particles (important to reduce multiple scattering), and maximized the height of the relativistic rise. Minimization of cluster broadening due to diffusion effects was addressed with the choice of the gas mixtures which are discussed later in section 4.4.0.2.

The gas box frame was fabricated with 3 mm thick G-10, a fiber-glass compound[5], because of its insulating properties, mechanical rigidity and strength. Clear mylar[6] foil (t = 35-50 μm; X_o $\sim$.11%) was used for the windows. A problem associated with mylar, and actually any plastic, is that oxygen and water are capable of diffusing through it. This is a concern because both are electro-negative and can absorb the drifting ionization electrons through attachment processes. This can create a drift length dependence on the amount of ionization measured in clusters. In order to overcome this problem, a dual pane window system was designed where two mylar foils were separated by a distance of 1 cm. An inert buffer gas (N_2) was circulated in this region at a high rate ($\sim$300 ℓhr^{-1}) in order to sweep away any water or oxygen before they reached the second window and had a chance to diffuse into the active region. The nitrogen was allowed to exhaust into the atmosphere. Such a system proved very effective in keeping both O_2 and water concentrations very low in all the chambers. The O_2 concentrations have never exceeded 8 ppm in any of the TPCs at any time during normal run conditions. Water concentrations have not exceeded 20 ppm in any chamber. The base of the gas box was a G-10/honeycomb sandwich. It is 10 cm thick because it must isolate the High-Voltage (HV) cathode of the field cage, just 2 cm above the top surface of the bottom plate, from the experimental area. It was also covered with a thin copper foil. This was

---

[4] Actually .5 mbar over atmospheric pressure.

[5] Typically 60% SiO_2 40% epoxy

[6] Polyethylene terephthalate.

done to protect the field cage from ground and to remove the possibility that the fiber-glass could become charged and distort the drift field.

The field cage is fully contained within the gas box and defines the active region of the detector. Its sole purpose is to provide a constant drift electric field in the active volume of the TPC. This is done by means of a HV cathode at the bottom of the chamber. The field is further shaped by potential strips in the vertical direction around the perimeter. These are discussed below. Owing to the different environments associated with the location of the chambers, their respective field cages were designed differently. The MTPCs are both offset from the beam-line and so do not have the Pb beam traversing them. As such, each MTPC has a single field cage defining its active volume. The VTPCs, on the other hand, straddle the beam-line, and have the Pb beam traversing the gas volume. In order to avoid a constant buildup of charge in the active area associated with the ionization produced by the beam (Z=82), two separate field cages were built within each VTPC gas box; one on each side of the beam. Thus the beam was restricted to an inactive region of the detector. In both cases the top of the field cage is defined by the FG. The equipotential HV cathode is kept at a fixed distance from the FG by tungsten plated, ceramic (Al_2O_3) posts ($\phi = 3$ cm) at each corner. The tungsten coating was etched into 13 mm rings that support the field shaping strips. These posts were hollow and allowed a laser beam to be distributed in the VTPCs from mirrors mounted at several different heights in the corner posts.

In order to ensure a constant electric field within the chamber, a linearly decreasing potential is required. This is produced by an array of aluminized mylar strips which effectively define the perimeter of the field cage. This mylar is 25 μm in thickness and cut into strips 12.5 mm in width. This construction produced a field cage which contributed a negligible .1% X_o to the total amount of material in the detectors. They have a pitch of 15 mm, and are strung under a tension of 10 N, to offset gravitational effects. The strips are fastened by a G-10 bracket mounted on a ceramic post by means of CuBe clips which are pressed, not glued, to the mylar. Adhesives or solvents can reduce the elasticity and weaken the strips as well as contaminate the gas volume by out-gassing volatile hydrocarbons.

A linear resistor chain completes the circuit from the FG to the HV cathode. For VTPC1(2) a 13. kV potential difference over the 66.5 (66.2) cm drift length produces a field of 195.5 (196.4) Vcm^{-1} while in the MTPCs, 16. kV over 115. cm produces a field of 139.1 Vcm^{-1}. The same mylar strips that shape the field, also line the HV cathode, with a slightly larger pitch (25 mm). In order to ensure a uniform electric field, the strips must define a planer surface. Since they are strung over a length of 2-4 m, the strips are supported by thin wires at 1 m intervals, that run the width of the chamber, perpendicular to the orientation of the strips; they are also under 10 N of tension. In order to ensure planarity, these wires were adjusted so that the strips had no more than a 20 μm deviation in height between them. Further shaping of the field (for the VTPC) was done at the read-out chambers by Al "skirts" mounted around the perimeter of each read-out chamber. The voltage was adjustable to ensure that the field lines would not bulge or contract at the top owing to the presence of the wire grids.

4.4.0.2 Gas Considerations

The gas enters the detectors at the bottom of the chambers, in the center of their respective field cages. It is distributed by a deflector plate made of stainless steel suspended 3 mm above the top surface of the gas box bottom plate. It was hoped this would create a smooth laminar flow of gas into the chamber and avoid the creation of a stable flow pattern through a single region of the chamber leaving some regions to become filled with stagnant gas. Studies with ^{83m}Kr injected into the gas indicate that although a definite flow pattern within the chambers is established, there are no regions within the chamber where the gas stagnates [88].

Argon-methane gas mixtures are usually preferred in the case of drift chambers and TPCs because they are cheap and the drift velocity has a plateau at a relatively low drift field. However, they are not suitable for chambers subjected to a high track density. This is because these mixtures have a rather large electron diffusion coefficient which limits the TTR. Furthermore, because of its high Z, Ar based mixtures produce large amounts of ionization, typically of the order of 30 $e^{-}cm^{-1}$, and large multiple scattering effects. Multiple scattering reduces the position (and hence momentum) resolution and the large ionization increases the space charge inside the chamber, neither of which are desirable. It was found that adding He or CO_2 reduced the drift velocity as well as the diffusion coefficients appreciably [89]. It was also found that gas mixtures are further "cooled"[7] by the replacement of Ar with Ne. Although Ne has the favorable property of lower atomic number, it is substantially more expensive than Ar. Therefore a two component gas–$NeCO_2$ (90:10) was selected for the operation of the VTPCs because the region they cover is subjected to the highest track density, owing to their proximity to the target. Since the MTPCs have a much larger volume than the VTPCs, and must cope with a somewhat reduced track density throughout most of the chamber, they are filled with a less expensive three component gas—$ArCO_2CH_4$ (91:4.5:4.5). Although the cool gases have favorable diffusion properties, other complications arise with their use. The gas gain characteristics of these mixtures are a *strong* function of their composition and the stability of their concentrations is important. Furthermore the drift velocity is not in the plateau region (with the present drift field) and is subject to small fluctuations of the HV supplies [89]. This places rather rigid constraints on the gas system and on the associated monitoring equipment, in order to provide stable performance of the detectors over the course of a 4-8 week run.

There are four separate gas systems, one for each chamber. Each mixes the gases using gas flow meters and distributes it to the chambers. The gas is recirculated in a closed system, which allows for water and oxygen removal by filters. The gas composition is monitored in two ways—the gas gain and drift velocity are measured by separate proportional tubes within the gas recirculation circuit. These values are continuously recorded by the Slow Control (SC) system and adjustments in the gas composition can be made, if variations become appreciable. They are also available for off-line correction. The gas gain and drift velocity are also a function

---

[7] Diffusion and drift velocity reduced.

of environmental parameters like temperature and pressure. While the TPCs are contained within climate controlled huts where temperature is controlled to a precision of $\pm .1^o$, atmospheric pressure is monitored and recorded so corrections can be done off-line. The circulation rate of the gas in normal operation is 110 $\ell \mathrm{hr}^{-1}$ for the VTPCs and $400 \ell \mathrm{hr}^{-1}$ ($3\ \mathrm{m}^3 \mathrm{hr}^{-1}$) for the MTPCs with 1% fresh gas (by volume) added. This can also be run in "purge" mode which facilitates a rapid exchange of the gas within the chambers. This is 660 $\ell \mathrm{hr}^{-1}$ for all TPCs.

4.5 TPC Electronics and Data Acquisition

In consideration of the number of channels and the associated hardware necessary to read out the detector, a system was custom designed at LBNL [90], and is described in detail elsewhere [91]. The system has the analog readout and digital conversion mounted directly on the chamber. The data is then multiplexed into optical signals for transit to the counting house for further processing and recording. The use of optical signals significantly reduces the number of cables required and decouples the chamber electronics from those in the counting house. This reduces the possibility of spurious ground loops and possibilities for cross-talk and noise. Constraints were placed upon the electronics by the linearity requirement for ionization measurements and pad to pad stability.

The structure of the electronics is seen in figure 4.6. On the chamber, the Front End (FE) cards mount directly to the back of the pad plane. The FE card has four functions—amplification and shaping of the signal developed on the pad, storage of the time evolution of the signal (see figure 4.5), and the analog to digital conversion of the data. The analog pulse height information of each pad is read out over the drift time and stored in a Switched Capacitor Array (SCA). This is essentially a number of sample and hold circuits[8] each which corresponds to a single time bin. The size of each time bin is dependent on a clock rate sampling the data. In the case

---

[8] 512 such circuits in our case.

of 1994-96 runs, the clock rate was 10 MHz, which corresponds to 100 ns per time bin. With a nominal drift velocity of 1.4 cmμs^{-1}, this is approximately 1.4 mm in the drift direction. The charge collected on a pad for a minimum ionizing particle is the order of 5 fC. The pre-amplifier has a conversion gain factor of $\sim$50 mV fC^{-1} which means a 250 mV pulse is generated. Given an rms. noise of $\sim$1100e^{-}, the signal to noise ratio is approximately 30:1. After the pad information has been stored, the analog information is converted to digital via a 9 bit ADC. The conversion time is 10 μs per time bin so all 512 bins are converted in 5.1 ms. These operations are facilitated by two individual chips–one that handles acquisition and storage, the other the digital conversion. Each chip has 16 channels and each FE card has 2 sets of chips for a total of 32 channels. This generates a significant amount of heat (2 W per card) and due to the high density of the electronics, cooling by convection was insufficient. A novel water cooling system is employed where chilled water circulates in aluminium radiator plates placed between the rows of FE cards. In order to avoid leaks in the system, a negative pressure draws water through the system rather than pumping it. An elaborate temperature sensor array is employed that records the temperature in numerous locations around the TPCs. If an abnormal temperature is measured the system has authority to turn off the low-voltage power to the electronics. This is important as not only does electronic noise increase with temperature, but a large heat source on the top of the chamber

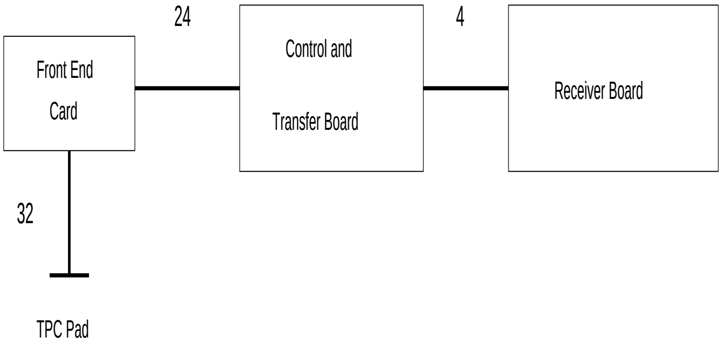

Figure 4.6: A schematic of the electronics chain.

can produce a temperature gradient within the chamber. As the drift velocity in a gas is sensitive to temperature, this could introduce a drift velocity gradient and the linear relation between the vertical (y) coordinate in the chamber and drift time would be lost.

The second component in the electronics chain is the Control and Transfer (CT) board. Each CT board distributes low-voltage power as well as clock and trigger signals to 24 FE cards and controls the transmission of data to the Receiver Boards (RB) in the counting house. After the FE digitization is complete, the CT board converts the data into an optical signal for transfer to the RB. For the 768 channels of a CT board, 62 ms is required for this process.

Each RB has 4 channels—each of which is capable of accepting data from a CT board. In order to read out all 181254 channels, 60 RBs are required. During the 5280 ms of beam spill, the data is buffered into memory. Adequate memory for 32 events per spill is provided ($\sim$ 12 MB per CT board). Because the size of a raw event is nearly 90 MB, it is not feasible (or necessary), to write all this on tape. Here the spill structure of the accelerator works to our advantage. As previously mentioned the duty cycle of the machine is $\sim$28%, which implies the rest of the time may be used for processing and compression of the data. Although 650 ms evt^{-1} is available (based on the acquisition of 32 events per spill), in reality only $\sim$350 ms is actually used. Because the occupancy of the chamber is at most 10%, this means the data can be reduced by as much as an order of magnitude. This compression is the job of the RB.

Each ADC channel (time bin) has an associated pedestal value associated with it, which is stored in the RB memory. It is deduced from reading empty events in dedicated runs (pedestal runs), taken several times per week. This pedestal value is subtracted, channel by channel, in order to reduce the noise. After pedestal subtraction, the data is then parsed in the time direction for each channel. If non-zero ADC values occur in at least two adjacent time bins, the data is kept, otherwise it is suppressed. A Digital Signal Processor (DSP) carries this out, and writes the results to an output buffer. After this processing is complete, the data is combined with that of the other RBs as well as the CAMAC and FASTBUS modules for the auxiliary systems and written to tape. A complete event requires approximately 8-9 MB of space, consistent with the 90% reduction in volume expected. This processing occurs over the entire length of the spill and begins as soon as the first event reaches the RBs input buffer.

The tape drive is a novel high speed recording device–the SONY D-1000 which allows writing at a speed of up to 16 MBs^{-1}. This allows a maximum data rate of 2 Hz DC or 32 events per spill. The magnetic tapes have a maximum capacity of 100 GB which is equivalent to approximately 10k events. This is normally filled in the space of 3-4 hours which defines the length of an NA49 run. With a beam time of about 4 weeks each year, this allows a maximum of nearly 1 million events, assuming an efficiency of 50%.

4.6 Calorimeter, Trigger and TOF

The analysis presented in this thesis is from the VTPCs. However for completeness, a brief discussion of the TOF and calorimeter systems is included. The calorimeter system is important as it is the central component in the trigger system.

The TOF system is made up of 4 separate walls each downstream of the MTPC (see figure 4.2). They are comprised of nearly 2000 channels between the 4 systems. The largest two arrays (TOF-L1 and TOF-R1) each cover an area of 2.2 m^2 with 891 separate channels. Each read-out channel consists of a plastic scintillator (6-$8\times3.4\times2.3$ cm^3) glued to a photo-multiplier. The tiles are arranged in a tile pattern with the smallest tiles placed closest to the beam in order to minimize double hits in the counters. Still, double hits over the area of the complete wall account for approximately 10% of the data. Time resolution of the order of 60 ps is realized from these systems.

Two other smaller arrays (TOF-L2 and TOF-R2) are constructed in a grid geometry [92]. This geometry allows a larger area to be covered per electronics channel with a finer granularity; the only penalty being that the probability for double hits is increased. Forty-eight scintillator bars are mounted in the horizontal direction ($48\times2.5\times2.4$ cm^3) and 45 in the vertical direction ($130\times1.0\times1.5$ cm^3), covering an area of .624 m^2. Photo-multipliers mounted at each end of a bar in order to read out the detector. Approximately 21% of the total number of signals are unresolvable double hits. Time resolution is of the order of 85 ps with this system.

A time interval (TOF) of a particle is measured by starting a clock when an interaction in the Pb target occurs and stopping it when a scintillator in the wall is hit. A common start signal is provided by a small scintillator upstream of the target (S_o which is upstream of S_1 in figure 4.2). The stop signal is produced by a particle's interaction with a scintillator in the TOF wall. Both the pulse height and TOF is measured by standard FASTBUS ADCs and TDCs. Because the TPCs give accurate information of the position of tracks, extrapolation from the TPC to the TOF wall gives a precise position of interaction. This allows a correction for the transit time of the light through the scintillator to be made. This greatly improves the time resolution. Figure 4.7 shows the PID capability of NA49 using specific ionization information from MTPC and TOF in 1994 data. The $\frac{dE}{dx}$ component of the measurement will be further explained in chapter 5.

The ring calorimeter was used in 1994 in a dedicated calorimeter run to first characterize the initial Pb-Pb collisions and to extend measurements made by NA35. It has been used in previous CERN experiments (NA5, NA22, NA35) and is detailed elsewhere [93]. Briefly it consists of a Pb-scintillator electro-magnetic region 16 X_o, and 1 λ_{int} thick followed by an Fe-scintillator hadronic section 6 λ_{int} in length. It is tube shaped with an inner (outer) radius of .28 (1.5) m, segmented into 240 separate cells, 24 azimuthally and 10 radially.

The veto calorimeter, placed further downstream behind a 1 m iron collimator is the main component of the trigger. It is a total absorption Pb-Fe sampling calorimeter separated into 4 separate cells. It has a total length of 16 X_o and 7.5 λ_{int}. Because heavy ions are extended sources, a geometric picture of the collision is possible, and provides a useful means to construct a trigger. A central (violent)

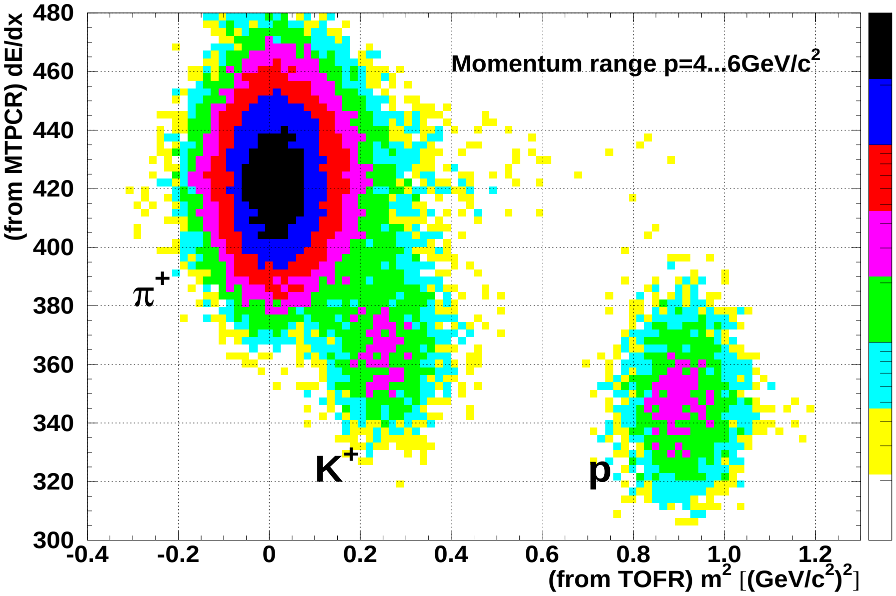

Figure 4.7: PID utilizing both specific ionization (from MTPC) and TOF information.

interaction can be characterized by having a small amount of forward energy, which means most of the energy is distributed in the transverse direction [77]. This is seen in figure 4.8 and allows a rather simple effective trigger design.

The trigger system is shown schematically in figure 4.9. It is made up of several scintillators and the veto calorimeter. An iron collimator placed in front of the veto calorimeter defines a cone in the most forward $.6^o$ about the beam. Because of the low beam flux ($\sim 5\times10^4$ spill^{-1}), particles incident on the target can be observed individually by scintillators in the beam line. A beam particle is detected via coincident signals in S_1, and S_2 and no signal in V_0. S_1, and S_2 are thin (.2 mm) quartz Cerenkov counters.[9] V_0 is a scintillator with a 1 cm central hole where the beam nominally passes. If no interaction within the target occurs, it is expected that 33 TeV of energy (beam energy) will be deposited in the veto

---

[9] For proton running, they are replaced with conventional plastic scintillator.

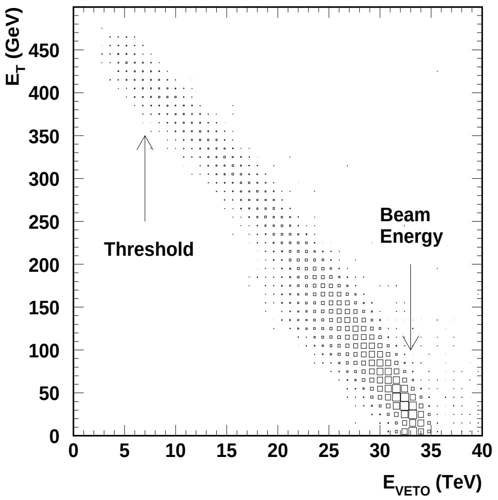

Figure 4.8: Data showing the relation between the Transverse (E_T) and forward (E_{VETO}) energy produced in a heavy ion collision. Full beam energy of 33 TeV is deposited in the forward (veto) calorimeter when no interaction occurs. By setting a threshold on the amount of transverse energy produced, it is possible to select central (violent collisions). The indicated threshold corresponds to interactions with an impact parameter of $\leq$ 4 fm.

calorimeter. If less energy is measured, it can be assumed that an interaction has occurred. Because of the linear relation between the forward or veto energy (E_{veto}) and the transverse energy (E_T), the degree of centrality can be selected according to the veto energy. This is indicated in figure 4.8). When such an event occurs, a trigger signal is generated and distributed to the various detectors and they are read out. Although the occurrence of an interaction is easy to detect, these signals do not determine that an interaction has occurred within the target. It must be remembered that interactions between Pb projectiles and gas molecules within the TPCs (and air outside the TPCs) can fake a valid trigger signal. The amount of material in the beam path is minimized with He bags placed between VTPC1 and VTPC2 as well as in the region between VTPC2 and the MTPCs. Helium reduces the amount of material by a factor of ~12 in comparison with air (i.e. X_o^{air}=.35%m^{-1}, X_o^{He}=.029%m^{-1}), but there still is potential for superfluous interactions. This is the reason for the detector S_4, which is a second interaction

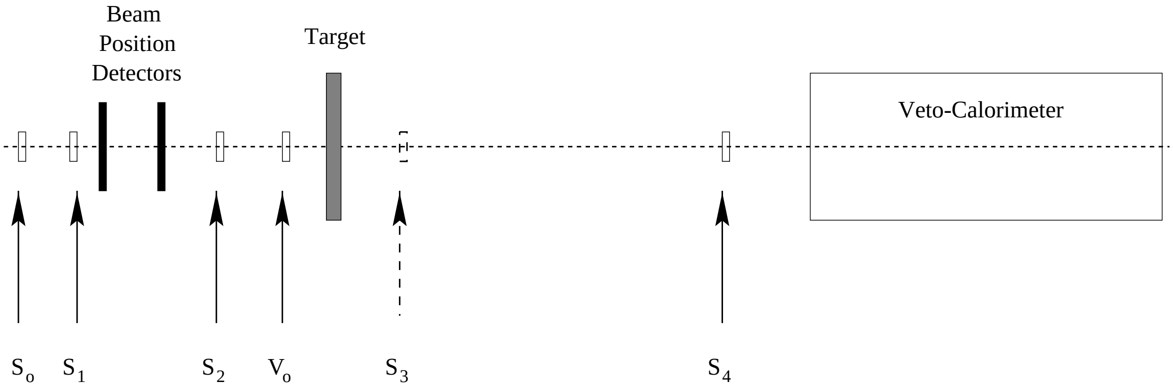

Figure 4.9: The location of beam defining counters in NA49.

detector. It is a Cerenkov counter situated downstream of the MTPCs and is set so it is triggered when a Pb projectile passes through it. As such, it determines when no interaction has occurred between it and the target. Although the veto calorimeter is sensitive to "non-interactions", this counter provides a fast signal for the TOF detectors to clear and reset, because they must be triggered on each beam particle. Because of its location, S_4 also has the ability to discriminate against events where an interaction occurs downstream of it in the 10 m of air between it and the veto calorimeter. In this region, the photo-disintegration of nuclei due to the strong relativistically enhanced electric fields in peripheral ion-atom interactions are quite probable. Because heavy charged fragments are produced, they can mimic the appearance of a central collision and S_4 provides a means to discriminate against such events. So, the trigger logic can be written as:

$$\underbrace{S_1 + S_2 + \overline{V_0}}_{Beam} + \overbrace{\overline{S_4}}^{Non-Target\ Interaction} + \underbrace{\overline{veto}}_{Interaction} \tag{4.1}$$

This is useful to reject background events in very central events, but it is not effective if large impact parameter or peripheral events are required for study. Even with He bags between the TPCs the beam particles have ~20 m flight between the target and interaction counter S_4, and contributions from non-target interactions were appreciable for non-central triggers (as much as ~40%).

In order to extend the capabilities to study large impact parameter collisions, the trigger system, as described above, was replaced at the end of 1995. A helium Cerenkov counter, called S_3, was added just downstream of the target. S_2 was also replaced with a similar Cerenkov counter. This added a negligible amount of material in the beam line while allowing the presence of an interaction counter to be situated very close to the target. An interaction in the target is detected when a valid beam particle is seen (i.e. $S_1 + S_2 + \overline{V_0}$) and there is a signal in S_3 below that expected for a Pb ion. This reduces the contributions from non-target interactions as well as allowing for a simple mechanism to vary the impact parameter. This is controlled by the threshold of the signals seen in the interaction counter S_3. Collisions with impact parameters of up to 10 fm to have been studied with less than 10% background.

Chapter 5

Event Reconstruction

The calibration is the first task carried out in the event reconstruction procedure and it consists of two parts—electronics and gas gain. The purpose of the electronics calibration is to remove any channel to channel variations in electronics response, independent of processes that occur within the detector. The gas gain calibration on the other hand, is intended to remove variations in response due to read-out chamber geometry and mechanical deformities, differences in the HV distribution circuits, etc. [94].

The electronics calibration is carried out by pulsing the field wires with a fixed amplitude signal. This induces a charge distribution on the pad plane, with the total charge being proportional to the area of each pad. In VTPC1 all pads have the same area. However, in VTPC2, the pads increase in area in proportion to the distance from the beam line [86]. After this trivial area dependence is removed, a relative gain can be determined for each channel such that all have an identical response [95]. It should be noted that this procedure assumes each pad (i.e. electronic channel) responds independently, which does not seem to be the case. In fact, as illustrated in figure 5.1, the response of the calibrated chamber retains the Integrated Circuit (IC) structure of the electronics. The seemingly anomalous collective effects in this calibration procedure are an indication that the electronics behave in a non-linear fashion when different loads and current demands are placed upon it, and may render the current electronics calibration procedure ineffective. This is discussed in more detail in section 5.2.1. This may have serious implications for the Solenoidal Tracker at RHIC (STAR) detector because the TPC electronics are based on the same design.

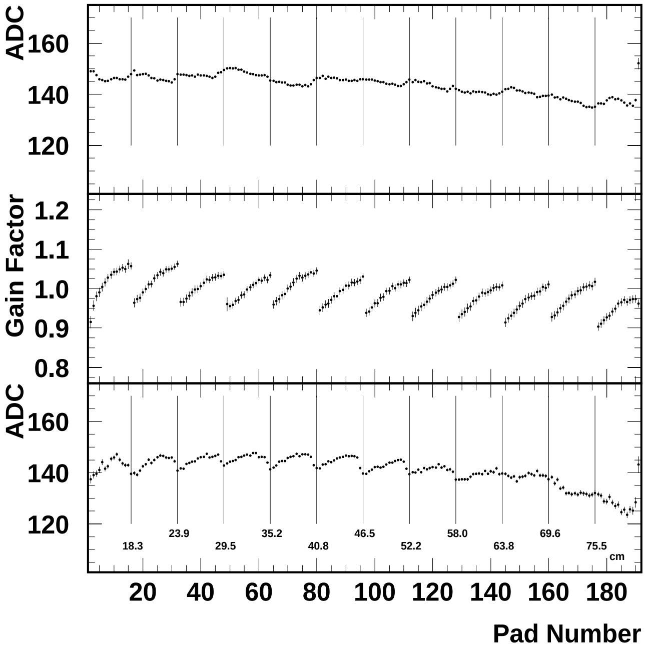

Figure 5.1: The calibration constants and their effect on the chamber for the Jura side of VTPC2 integrated over all z. The top shows the response of the uncalibrated chamber to particle tracks in a central Pb-Pb event. The middle shows the structure of the (multiplicative) electronic gain constants as deduced from the pulser calibration. The bottom shows the response of the calibrated chamber to particle tracks where the IC structure is visible. The boundaries between Front End Cards are indicated with the approximate x coordinates. The apparent slope of the gain factor appears to be an indication of the increasing area of the pads at further distances from the beam line.

The second part of the calibration is designed to correct for the variation in gas gain throughout each chamber. It is determined by measuring the energy spectrum of ^{83m}Kr which is injected into the TPCs. This source provides several useful calibration lines, particularly at 9.4, 12.6, 32.2, and 41.6 keV. Since a minimum ionizing particle deposits approximately 1.8 MeV/g cm^{-2} ($\sim$2.2 keV cm^{-1} in Ne at atmospheric pressure), the source deposits energy within a factor of 2-10 times that expected from real tracks. In order to avoid saturation, the sense wire HV was reduced from that of normal operating conditions. Prior to 1996, the krypton calibration was done only in VTPC2 and the MTPCs. Limited statistics permitted the determination of only one calibration constant for every third of a pad row; one per sixty-four pads in the VTPC, and in the High Resolution (HR) sectors of the MTPCs and one for every forty-two pads in the rest of the MTPCs. Krypton data taken in the 1996 run, with increased statistics (60 decays per channel), allows a finer granularity in the determination of gas gain constants and perhaps will allow for the eventual replacement of the electronics calibration procedure. Work is on-going in these matters and initial results are encouraging [96]. The events analyzed in this thesis are reconstructed using the pulser and Kr calibration in VTPC2 and only the pulser in VTPC1. It is hoped a new calibration procedure, using only Kr will be in place by early next year.

After the calibration constants have been applied and unpacking of the raw data is complete, the tracking algorithms are applied to the event. In NA49 there currently exists two different methods. The first is a conventional cluster finder and track follower (PATREC). The other uses templates which are overlaid on the raw data to find patterns that fit specific track models (TRANS). Although both have been utilized in the past, it is the latter method that is used in the reconstruction of events for this thesis. The two methods are described below.

5.0.1 Summary of Tracking Methods

A track-follower must have a set of space points as its input, and this is produced by a “cluster finder”. The cluster finder currently used in NA49 is a so-called ‘1+1’ dimensional algorithm. It searches the time spectra of each pad, to determine if there is charge (above a certain threshold) in adjacent time bins. When such an occurrence is found, the data is then parsed in adjacent pads, at the same location in time. The geometry of the read out chamber was designed such that clusters occupy between 2-5 pads. The acceptance or rejection of a cluster hinges on tunable parameters. Currently single pad clusters, as well as those that spread over more than 4 pads are rejected. Similar conditions apply in the time direction. These cuts are more fully discussed elsewhere [97]. Once a cluster has been identified, its position and charge are deduced. The charge is simply a sum of the ADC counts in all time bins within the cluster. The largest ADC value from a single time bin within the cluster is also recorded (MAXADC). This is important for establishing the working point of the detector. The position of the cluster is calculated via a specific gravity method in both pad and time directions. Utilizing this method, spatial resolution much better than the width of a single pad (or time bin) is achieved. A typical event contains of the order of 20-30k clusters in each of the VTPCs and 40-50k clusters in each of the MTPCs.

Before the track following algorithm can be used, the cluster positions have to be corrected due to the presence of an inhomogeneous magnetic field (This is not required for the MTPCs). In the presence of an electric and magnetic field, a charged particle will not follow the electric field lines, but rather a helical trajectory which is described by the Langevin equation:

$$\frac{d\mathbf{v}}{dt} = \frac{q}{m}(\mathbf{E} + \mathbf{v} \times \mathbf{B}) - \frac{1}{\tau}\mathbf{v} \tag{5.1}$$

where q is the charge of the particle, m is its mass, $\mathbf{v}$ is its velocity, $\mathbf{E}$ the electric (drift) field, $\mathbf{B}$ the magnetic field, and τ is the average time between collisions with the molecules in the medium. The last term is essentially a frictional force that limits the maximum average drift velocity. The steady state solution (i.e. $\frac{d\mathbf{v}}{dt} = 0$) is given by:

$$\mathbf{v} = \frac{\mu|\mathbf{E}|}{1 + \omega^2\tau^2}(\hat{\mathbf{E}} + \omega\tau(\hat{\mathbf{E}} \times \hat{\mathbf{B}}) + \omega^2\tau^2(\hat{\mathbf{E}} \cdot \hat{\mathbf{B}})\hat{\mathbf{B}}) \tag{5.2}$$

where μ ($= \frac{e\tau}{m}$) is the electron mobility and ω ($= \frac{eB}{m}$) is the cyclotron frequency. A misalignment between the electric drift field and magnetic field, or inhomogeneities in the magnetic field produces a force perpendicular to the electric field direction.

This effect is easily parameterized in the position-time (x-t) relations in conventional drift chambers where the drift distances for the ionization rarely exceed several centimeters. However, in a TPC the ionization may drift distances on the order of *meters*. In the NA49 VTPCs, the maximum drift length is 66 cm. In such cases the distortions of a reconstructed track must be corrected if an acceptable position and momentum resolution is to be obtained. These corrections can be calculated by numerically integrating equation 5.2. However, this requires detailed knowledge of the magnetic field. The field measurement was a project undertaken by the author and is described in detail elsewhere [98]. The precision of the measurement is such that the minor field components are known to a level of $\sim 5{\times}10^{-4}$ of the main field component. This allows tracks to be reconstructed with residuals of the order of 100-200 μm, as illustrated in figure 5.2. Distortions due to mechanical imperfections of the detector also exist, and are corrected, but are small in comparison to those introduced by charge transport through a region of crossed electric and magnetic fields.

After the distortions are removed, the points can then be passed to a track follower. Such an algorithm works by finding a track segment in the furthest downstream part of the chamber and following the expected trajectory, based on a track model, back to the target. Points are added based on the minimization of the χ^2 probability that they belong to the track segment. A track terminates when the border of the detector is reached or no further suitable points can be found. A track must contain at least 9 points. No gap more than 6 consecutive pad rows long within the track is allowed. Furthermore, the track is not allowed to spiral back on itself. This provides rejection of low energy particles; and in particular delta electrons.

The other method of tracking is based on the Hough transform and is described elsewhere [99]. Briefly, it utilizes track templates and compares patterns of charge in the raw data to that expected by certain track models. Of course in this method the "E×B" distortions must be removed in the raw data, which is done via a look-up table. Although this method is a very efficient method for finding vertex tracks, it

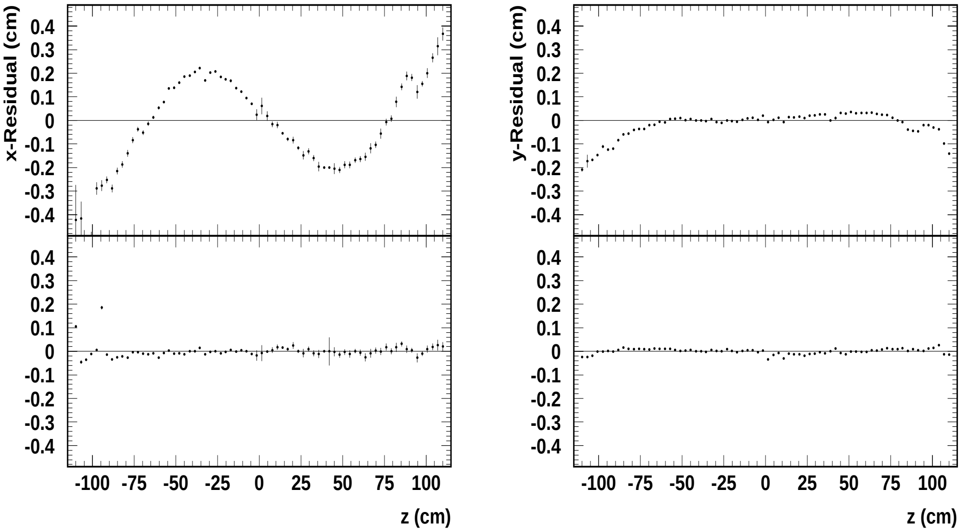

Figure 5.2: Residuals from a straight line fit to laser tracks in VTPC2 in the x (left) and y (right) directions, before (top) and after (bottom) E×B corrections. RMS residuals are below the 100 μm level after correction.

is not useful for daughters of neutral particles that decay downstream of the target (i.e. K^o, Λ, etc.), as this would require an infinite number of templates. Nonetheless, it is vertex tracks that are of interest in correlation studies which is the topic of this thesis.

Once a track is identified, it is possible to search each pad row which the track crossed for charge deposition. The charge is then quantified using a parameterized Pad Response Function (PRF). The PRF defines the integral of the charge induced on a cathode pad based on the detector geometry and electronics. If the electronics response is linear, the PRF is strictly a function of the pad plane-sense wire spacing and the pad width [100]. Under such an assumption, the PRF has been shown to be fairly well approximated by a Gaussian, *but* it is important to note that a cosine damped Gaussian was found to be much more suitable [85]. In fact, only if the width of the PRF (σ) is twice that of the pad width is a Gaussian a good approximation. The shape of the actual PRF is discussed in detail in section 5.2.4. In the case of the NA49 VTPCs, candidate clusters are fitted with a two-dimensional Gaussian in the pad (x) and time (y) directions. The amplitude and mean are left as free parameters while the widths vary as:

$$\begin{aligned} \sigma_x^2 &= \sigma_{prf}^2 + \sigma_D^2 \ell + \frac{d^2}{12} tan^2(\beta) + \frac{\ell^2}{12}(tan(\alpha) - tan(\psi))^2 \\ \sigma_y^2 &= \sigma_{el}^2 + \sigma_D^2 \ell + \frac{d^2}{12} tan^2(\phi) \end{aligned} \tag{5.3}$$

where σ_{prf} is the intrinsic pad response function of the detector (3.0 mm in VTPC1 and 2.2 mm in VTPC2), σ_D is the diffusion coefficient (220 $\mu\text{m}\sqrt{\text{cm}}^{-1}$ for $NeCO_2$ (90:10)), ℓ is the drift distance of the ionization, and d is the spacing between sense wires (4 mm). The rest of the parameters have to do with either the operating parameters of the chamber or properties of the track that create the ionization. If one projects the track onto the pad-plane, as shown in figure 5.3, β is the angle between the pad and track; α is the angle between the track and a line normal to the sense wire; and ϕ (not shown) is an angle analogous to α, but in the vertical plane; that is, it is the angle the track makes with respect to the plane defined by the sense-wires. ψ is the Lorentz angle, given by $\tan\psi = \omega\tau$. In the linear approximation, which is valid for $\omega\tau < 1$, the mobility is independent of $\mathbf{E}$ and $\mathbf{B}$ and the relation $\mu B = \omega\tau$ holds. In the presence of a magnetic field, this is expected to break down when the electron cyclotron frequency (ω) becomes equal to the collision frequency (τ^{-1}) of the drifting ionization. As such it is dependent on the strength of the magnetic field. In the case of the NA49 VTPCs, the cut-off field B_c, is 1.4 T. Thus the linear criteria is met in VTPC2, but it is marginal in VTPC1 for the standard field configuration. Nonetheless, this approximation is used in the calculation of the charge transport corrections and a space point resolution of $\sim$200 μm RMS is attained. For comparison, the cut-off field for the ALEPH detector, which operates in a solenoidal field of 1.5 T is B_c=.23 T.

Once a PRF is fitted to a cluster, its integral is proportional to the charge induced on the cathode pad from the avalanche on the sense wire, and its centroid gives the cluster position. Both are important as the position and momentum

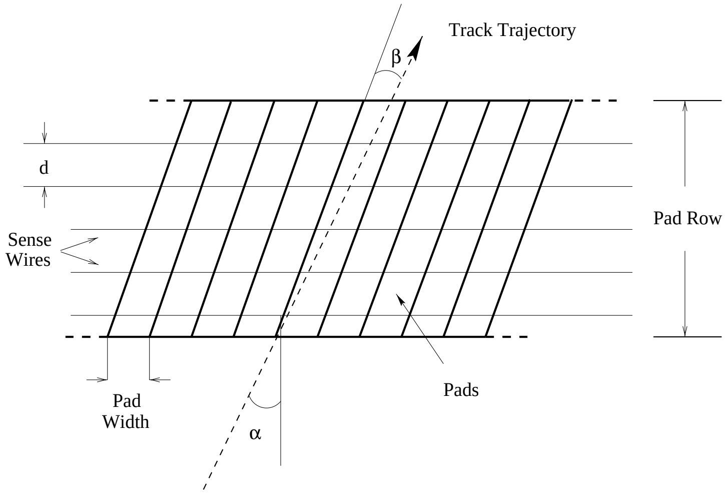

Figure 5.3: The projection, onto the pad plane of a particle crossing a pad row.

resolution are directly related while the charge quantification allows PID via the specific energy loss of the track. This will be discussed in detail in section 5.1.

After tracking is complete, the momentum of each track is found. The equations of motion for a charged particle in a magnetic field are numerically integrated along its trajectory. The constraints of the spatial coordinates and the magnetic field allow the momentum to be determined. In an ideal case where points along a trajectory are equally spaced and no multiple scattering occurs, the momentum resolution is proportional to the spatial resolution of the space points [101]. The momentum spectra and experimental resolutions for each of the VTPCs are shown in figure 5.4. After the reconstruction is complete, study of the energy loss of each track is possible.

5.1 Energy Loss of a Charged Particle

There are two separate approaches one may take in trying to understand the energy loss of a charged particle in medium: the purely theoretical in which ionization yields are deduced through microscopic calculations of the EM interaction of a

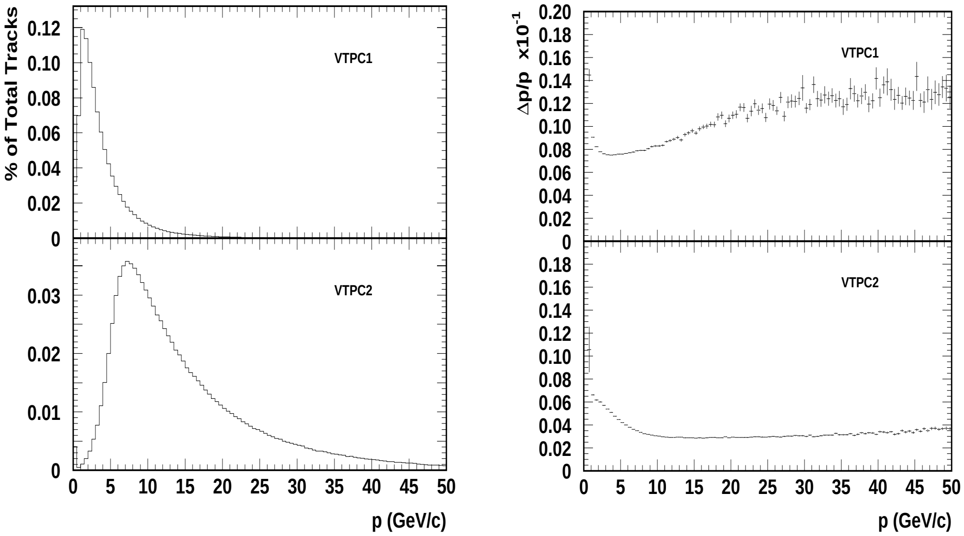

Figure 5.4: Momentum spectra in the two VTPCs (left) and the approximate resolution measured (right). Both are on the same scale for direct comparison.

charged particle with the atomic structure of the media; or the empirical approach where the ionization yields are deduced from experimental measurements. Although a rather elegant theoretical framework exists, it does not describe the data to more than a 20% accuracy. As such, most work in regards to this subject uses theory as a guide, but consistency with other measurements and reproducibility of results, rather than strict agreement with theory is the measure of quality. In the following section both approaches are mixed, rather indiscriminantly, in an attempt to make clear the process of using specific energy loss or $\frac{dE}{dx}$ for PID.

Consider a situation as shown in figure 5.5 where a charged particle is traversing a gaseous medium with a velocity $\mathbf{v}$. The force between a particle of charge ze and an electron of a gas molecule is ze^2/r, where r is their relative separation. If the electron in a gas molecule of the medium can be considered free and at rest, it will

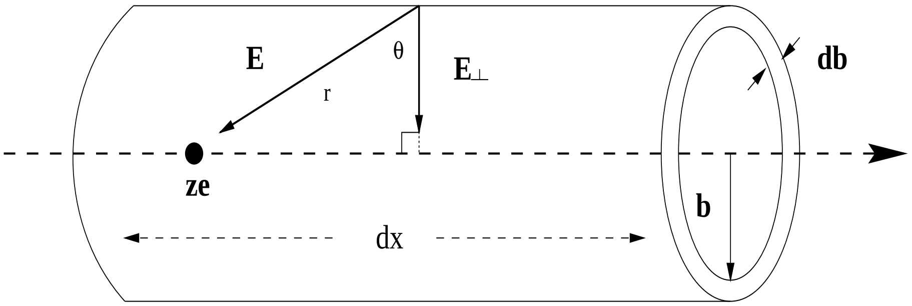

Figure 5.5: An interaction of a charged particle with an atomic electron of the medium.

acquire an impulse:

$$\Delta p = \int_{-\infty}^{\infty} dt \; e\mathbf{E}_{\perp} = ze^2 \int_{-\infty}^{\infty} dx \; \frac{1}{v} \; cos(\theta) \; \frac{1}{r^2} \tag{5.4}$$

The energy transferred to the electron is then given by:

$$\Delta E = \frac{(\Delta p)^2}{2m} = \frac{2}{m_e}(\frac{ze^2}{bv})^2 \tag{5.5}$$

From this equation it can be seen that the energy loss of a charged particle is due almost entirely to its interaction with atomic electrons of the surrounding medium instead of the heavier nuclei. For example, in hydrogen:

$$\frac{\Delta E_{nuc}}{\Delta E_{e^-}} = \frac{m_e}{m_{nuc}} \sim \frac{1}{1840} \tag{5.6}$$

In the cylinder of figure 5.5 there are $2\pi N b \, db$ electrons per unit length dx, where N is the electron density. Thus the energy loss per unit length, dx, can be written as:

$$-\frac{dE}{dx} = 4\pi N \frac{z^2 e^4}{mv^2} \int_{b_{min}}^{b_{max}} \frac{db}{b} \tag{5.7}$$

Using the quantum theory of collisions between a particle and an atom, Bethe showed that the above integral is strictly a function of the velocity of the charged particle and physical properties of the medium [102]. With the inclusion of relativistic effects, the energy loss is given by the Bethe-Bloch equation:

$$-\frac{dE}{dx} = 4\pi N_o r_e^2 m_e c^2 \frac{Z}{A}\rho\frac{1}{\beta^2}z^2[\ell n(\frac{2m_e c^2}{I}\beta^2\gamma^2) - \beta^2 - \frac{\delta}{2}] \tag{5.8}$$

where N_o is the Avogadro number, r_e $(= \frac{e^2}{m_e})$ is the classical electron radius, and ρ, Z, and A are the medium's density, atomic number, and mass number respectively, I is the ionization potential of the medium, and δ parameterizes a "density effect" which describes the saturation of the energy loss at highly relativistic velocities [103].

Equation 5.8, defines the energy loss of heavy charged particles due to ionization. By inspection it can be seen that non-relativistic particles (i.e. $\beta\gamma \ll 1$), lose energy proportional to $\frac{1}{\beta^2}$. As $\beta\gamma$ increases, the energy loss goes through a broad minimum ($\beta\gamma \sim 3$) and then begins to rise. The ionization potential I, in the logarithmic term determines the strength of this rise. The increasing energy loss occurs because the transverse electric field increases in strength at relativistic energies. In vacuum, this increase is strictly proportional to γ. However, in a medium it is not without bounds. The electric field will induce a polarization in the material which effectively screens atomic electrons at large distances from the ionizing particle. As a result the energy loss asymptotically approaches a constant at ultra-relativistic energies (i.e. $\beta\gamma \gg 1000$). Detailed calculations have investigated this effect and a simple parameterization was put forward by Sternheimer and Peierls [104] which is used extensively in particle physics. It will also be used in this analysis, and is of the form:

$$\begin{aligned}
\delta &= 0 \text{ for } (X < X_o);\\
\delta &= 4.606(X - X_a) + a(X_1 - X)^m \text{ for } (X_o < X < X_1);\\
\delta &= 4.606(X - X_a) \text{ for } (X_1 < X)
\end{aligned} \tag{5.9}$$

where $\mathrm{X} = \log_{10}(\beta\gamma)$, $a = 4.606(\mathrm{X}-\mathrm{X}_a)/(\mathrm{X}_1-\mathrm{X}_o)^m$, $\mathrm{X}_a = \log_{10}(1.649/\mathrm{I})$, and $\mathrm{I} = 28.8\sqrt{\rho Z/A}$.

Values for the parameters X_o, X_1, and m are either fit to the experimental data or taken from tables [105]. In general it is preferred to fit the parameters to the data since the values in the table tend to overestimate the height of the rise by 10-20% [106]. This is discussed further in section 5.3.

Although equation 5.8 describes the energy loss for heavy charged particles at the 5-10% level, it does not hold for the energy loss of electrons, since contributions from radiative effects and pair production become quite large. Furthermore, electrons can transfer a substantial fraction of their energy to an atomic electron in a collision and this invalidates the assumptions made for the limits of the integral in equation 5.7. However, even electrons of moderate energy (i.e. $E \sim 1$ GeV have $\beta\gamma \sim 2000$) lie in the saturated region.

The behavior of the energy loss due to ionization is schematically shown in figure 5.6. In solids, liquids, and high density gases, the plateau is only a few per cent above the minimum. At atmospheric pressure in noble gases (and some molecular gases), it reaches values of 40-60%. This variation allows the measurement of a particle's velocity, and in conjunction with its momentum, PID is possible. It is noteworthy that at higher energies (i.e. $\gamma > 4000$) contributions due to radiative processes dominate [107]. Likewise at extremely low energies (i.e the particle velocity is much smaller than that of atomic electrons; $\beta < \alpha Z$), non-ionizing nuclear recoil becomes an important contribution to energy loss which is proportional to the particle velocity (β) [108]. The NA49 spectrometer works in the momentum range of 1-30 GeV as seen in figure 5.4.

Strictly speaking a detector does not measure the energy loss of a particle but rather the energy deposited by ionization processes in a localized volume. The assumption that these quantities are *directly* proportional is implicit in any attempt of PID by specific ionization. The amount of ionization produced is quantified by a measurement of the total number of electrons collected per unit length of track, after appropriate (linear) amplification. The produced ionization has an energy distribution that is roughly $\frac{1}{T^2}$, where T is the kinetic energy. As such, the probability of producing high energy electrons is not negligible [109]. In fact, it is not

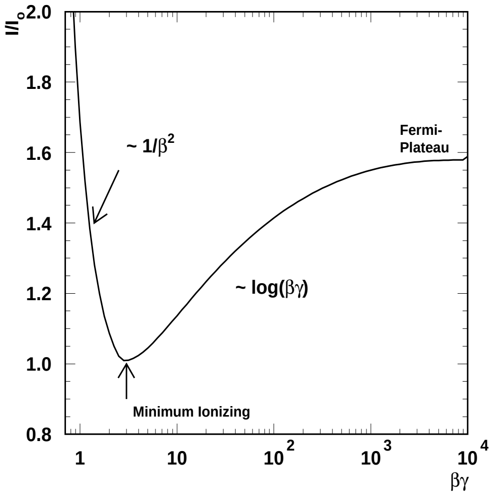

Figure 5.6: Rate of energy-loss for charged particles as given by equation 5.8.

atypical to have such delta electrons with energies of several MeV. The effectively infinite range of such particles results in the energy being carried away from the point of the interaction, and essentially lost. Thus in practice, the energy a particle deposits in a detector is limited to some cut-off value. Such considerations modify the Bethe-Bloch equation slightly [110] and the *measured* $\frac{dE}{dx}$ is better parameterized by:

$$-\frac{dE}{dx}_{meas.} = 4\pi N_o r_e^2 m_e c^2 \frac{Z}{A}\rho\frac{1}{\beta^2}z^2[\ell n(\frac{\sqrt{2m_e c^2\beta^2\gamma^2 E_{max}}}{I}) - \beta^2 - \frac{\delta}{2}] \qquad (5.10)$$

where E_{max} is a parameter defining a cut-off energy. It is typically the order of some 10s of keVs.

From the more phenomenological point of view, if the amount of energy required to create a single electron-ion pair W, is known, the energy deposition can be calculated. Since ionization involves an interaction of a particle with a medium, the mean free path can be used to estimate the number of possible interactions. However, because only a fraction of these collisions transfer an energy larger than the ionization potential of the medium, W is not in practice calculable, and must be measured for all media of interest, *and* for various types of radiation if high precision is required. Usually, W is determined by injecting a particle of known energy into a medium. The amount of ionization produced by particles that lose *all* their energy can be measured by a proportional counter. W is given as the ratio of the incident energy (E_i) to the total number of electron-ion pairs (n) created (i.e. $W{=}E_i/n$). It should be remarked that the ionization potential is generally a factor of 1.5-3 times smaller than W for any particular gas. Because there is a velocity dependence on energy loss (see equation 5.8), extrapolation to relevant energies is necessary. It is curious that for energies exceeding several 10s of keV, the amount of ionization is essentially constant. This is illustrated in figure 5.7. Many measurements of W have been made over the years, and to exceedingly good accuracy [111]. Values for some gases of importance to NA49 are shown in table 5.1.

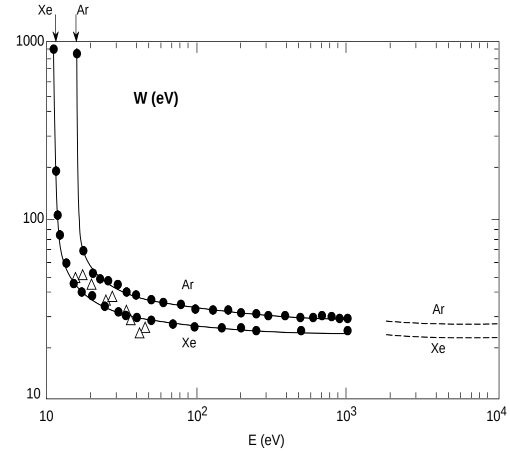

Figure 5.7: Example of measurement to deduce W. Shown is the average energy W spent (in eV) for the creation of one electron-ion pair in Ar and Xe as a function of the incident energy of the ionizing particle (in this case, an electron). Dashed lines are extrapolations to higher energies of interest in the operation of drift chambers. Figure from [112]. Reproduced by permission.

If one looks at the microscopic level of ionization production, it is realized that there are two different components that comprise the total yield (n); primary and secondary ionization. This is schematically depicted in figure 5.8 The ionization produced directly by the incident track is referred to as *primary ionization* and

Ionization Parameters for Some Common Detector Gases

Gas	Z	A	ρ (g cm^{-2})	$\frac{dE}{dx}$ (MeV/g cm^{-2})	W (eV)	$e^{-}_{primary}$ #cm^{-1}
He	2	4	1.66×10^{-4}	1.94	41	5.9
Ne	10	20.2	8.39×10^{-4}	1.68	36	12
CH_4	10	16	6.74×10^{-4}	2.21	28	16
Ar	18	39.9	1.66×10^{-3}	1.47	26	29.4
CO_2	22	44	1.86×10^{-3}	1.62	33	(34)
Xe	54	131.3	5.49×10^{-3}	1.23	22	44

Table 5.1: Properties of gases used in the NA49 TPCs are shown with He and Xe for comparison. Data is from [113].

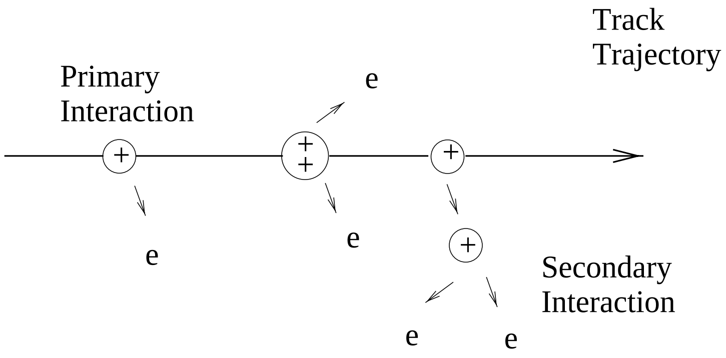

Figure 5.8: Schematic of ionization interactions occurring along a track trajectory showing both primary and secondary production.

is distributed according to Poissonian statistics. The mean number of primaries produced in various gaseous media is shown in figure 5.9. As one can imagine, this primary ionization has an energy distribution, $f(E)$ determined by the energy transfer in the collision. If the ionization is produced in "simple" atom-electron scattering, the distribution will have a E^{-2} profile. Strictly speaking the electrons are not free and a medium dependence on their energy spectrum is expected; that is, $f(E) \rightarrow f(E, Z)$. If any primary electrons have an energy E, above the value required to produce an ion pair (i.e. $E > W$), further ionization, known as *secondary ionization*, can be produced. In fact, most of the ionization produced is

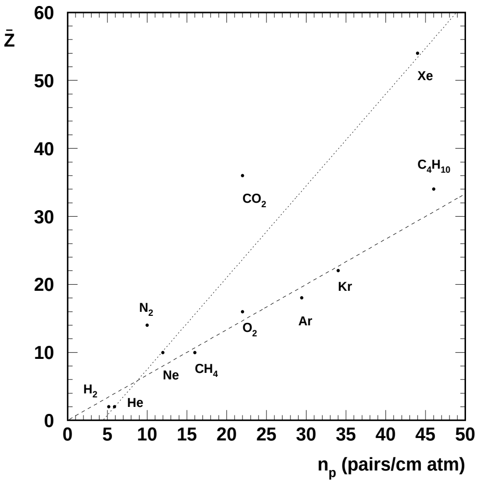

Figure 5.9: Number of primary electron-ion pairs expected per cm·atm for a variety of gases. All fall around a nearly linear relationship with $\bar{Z}$. He, Ne, and Xe seem to define a different Z dependence while N_2 and CO_2 do not seem to follow the simple linear dependences. The lines are a guide to the eye only.

due to secondary processes. Thus the total amount of ionization is a sum of two components—the first fluctuating according to Poissonian statistics, and the second superimposing a $\frac{1}{E^2}$ energy distribution on the spectra. Such a convolution produces large fluctuations that are non-Gaussian in character, even though the ionization process has some sort of statistical average. It should come as no surprise to realize that the number of primaries and secondaries are extremely difficult to measure individually as the observable is the *total* yield; not a single component. Data which exists for primary production (as in figure 5.9) dates back to the 1930s and '40s, although some current measurements do exist [114]. The way such measurements are usually done is to have particles crossing a region with very low pressure gas such that the probability for an interaction is very small. In such a case it can be assumed that *only* primary ionization is produced and the problem is then to count single electrons. In order to extrapolate to normal conditions, one must then assume the form of any pressure or density dependence. These problems are not trivial. However, this is an extremely important measurement because given the number of primaries, it is possible to calculate the $\frac{dE}{dx}$ behavior of a medium. This will be revisited in section 5.3.

Turning back to theory for guidance, Landau was the first to deduce an energy distribution for particles which have lost energy through ionization processes in traversing a layer of matter [115]. This was done making several simple assumptions:

- Successive Collisions are statistically independent.
- Mean energy loss is small compared to the total energy of the incident particle.
- Ionization is the only means of energy loss, and its strength is *fully* determined by the mean ionization potential of the medium.

The Landau distribution $\chi(x{,}E)$, which is the probability that upon traversing a medium of thickness x, a particle will loose an amount of energy between E and $E{+}\mathrm{d}E$ is given as:

$$\chi(x, E) = \frac{1}{2\pi i}\int_{-i\infty+\sigma}^{i\infty+\sigma} e^{sE - x\int_0^\infty \omega(\epsilon)(1-e^{-s\epsilon})d\epsilon} ds \tag{5.11}$$

where $\omega(\epsilon)$ is the rate of energy loss. For this, Landau used an expression given by Livingston and Bethe similar to that of equation 5.7 [116]. The method by which equation 5.11 is deduced is described in an elementary manner by Rief, in the context of collision theory [117]. The Landau distribution was soon generalized by Vavilov who showed that a Gaussian distribution was a special limiting case of a Landau distribution [118].

The form of the Landau and Vavilov distributions are cumbersome to work with because they are in integral form. In the early 1950s Moyal was able to reduce the Landau distribution to a simple, closed, analytic expression using several approximations [119]:

$$M(\lambda) = \frac{1}{2\pi} e^{-\frac{1}{2}(\lambda + e^{-\lambda})} \tag{5.12}$$

with:

$$\lambda(\epsilon) = \frac{\epsilon - \epsilon_p}{R} \tag{5.13}$$

where ϵ_p is the most probable energy loss, ϵ is the actual energy loss, and R is dependent on the properties of the absorbing medium. It is a very good approximation to the Landau distribution and is shown in figure 5.10 with a Gaussian for comparison.

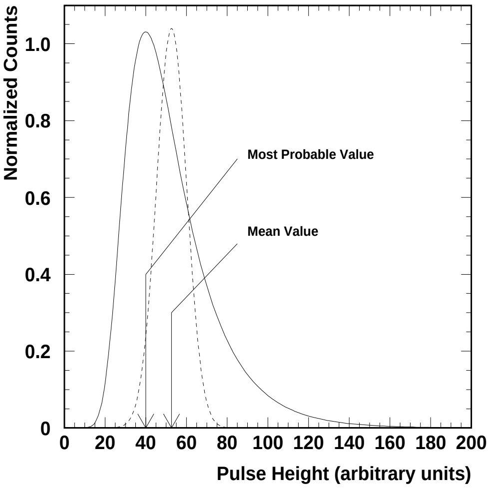

Figure 5.10: Moyal's function, an approximation to a Landau distribution, is shown with a Gaussian about the mean value of the distribution. The error on the Gaussian is that expected from N measurements.

5.2 Considerations in Specific Ionization Measurements

There are two separate concerns in utilizing $\frac{dE}{dx}$ information for PID. The first deals with considerations of how the measurements are made; while the second deals with how to treat the measurement in order to get an accurate, stable characterization of the energy loss.

5.2.1 The Measurement

For a relativistic particle, the height of the $\frac{dE}{dx}$ rise, under the most favorable conditions, is no more than 1.6 times that of a minimum ionizing particle. This means that at any specific momentum, there is little more than a 10% difference in the average energy loss between any particle species. Because of this small difference and the fact that the charge measurement is affected by many parameters, both from the detector and the environment, demanding constraints are placed on any charge measurement.

All energy loss distributions have inherently large widths because of the large fluctuations that are possible in the ionization process. One may think it possible to reduce the fluctuations by measuring energy loss from a thicker sample (i.e. higher pressure gas). Although the fluctuations are reduced, the probability for collisions with high energy transfer are enhanced. The height of the rise also decreases. Furthermore, with higher density layers, multiple scattering increases, reducing the momentum resolution in the detector. With such effects there is little gain in resolution realized with higher density media [120]. For these reasons and the fact that fixed target experiments do not have severe constraints of detector size placed upon them , the NA49 TPCs were designed to work at atmospheric pressure. It should also be mentioned that the separation power, and not the resolution, is the "figure of merit" of a detector. This determines how well one is able to resolve one particle species from one another and is discussed further in section 5.3.1. No matter, a single $\frac{dE}{dx}$ measurement carries little information regarding the average or most probable energy loss and therefore, many individual measurements need be made. This is the reason for the size of the NA49 detectors. For a track that crosses the entire NA49 apparatus, a maximum of 234 individual ionization measurements are possible; 72 in each VTPC and 90 in a single MTPC.

The working point of the detector is also an important consideration. Amplification must be high enough to maximize the signal to noise ratio, but not so high that saturation effects begin to adversely affect the measurement. The HV was fixed in each TPC such that the MAXADC distribution peaked at 25% of the maximum dynamic range of the electronics.[1] This produces a gas gain of $\sim 5\times 10^3$ for the MTPCs and $\sim$1-2×10^4 for the VTPCs. With such a setting, read-out chamber currents (168 sense wires per sector) did not exceed 400 nA. However, the chambers could still operate quite easily with a factor of 2 more current. Gas quality, electronics linearity, power stability, etc. are also important considerations as are the thermodynamic conditions of the chambers and surrounding environment (i.e. pressure, temperature, humidity, etc.). These are all continuously monitored and recorded in order to allow adjustments and off-line corrections to be made.

5.2.2 Corrections

Since each pad row makes a single measurement, it is the most basic unit "cell" to discuss in the context of energy loss measurements. Tracks are emitted in different regions in phase space and must be corrected for their effective length over a cell. The track, as seen in figure 5.3, has a longer effective length across the cell than a track incident in a direction normal to the sense wires. Thus two tracks with identical velocity will deposit different amounts of charge due to purely geometric considerations. This effect can be corrected once the crossing angle of the track, with respect to the sense wires is known. There are two such angles—one in the y-z and one in the x-z plane. These angles (α and ϕ in equation 5.3) are taken as constants instead of being calculated at each pad row. While this appears to be adequate in the environment of VTPC2, it is suspect in the performance of VTPC1 which is discussed in section 5.3.

The next task is to equalize the response of the individual read-out chambers. Although identical in construction, they are supplied by independent high voltage supplies and it is possible that potentials on the sense wires differ slightly. This is important because a difference in amplification voltage of 1 V, can alter the gas

---

[1] VTPC1 was set somewhat lower in order to reduce chamber currents. It should probably be increased in the next run period.

gain by as much as 1%. It is also particularly worrisome because this introduces the possibility of a load dependent gain in the detector. The HV supply does not produce a standing current in the read-out chambers. Rather the chambers draw current only when a signal is developed on a sense wire. This current produces a voltage drop over the current limiting resistor, which has a value of 10 kΩ. Although the measured (integrated) current over the course of a spill is maximally 400 nA, (which corresponds to ΔV$\sim$.004), the real concern is the peak transient current. If this reaches the level of mA (over ns time-scale), this could produce a voltage drop of 10V! This would seriously compromise the capabilities of ionization measurements. The feasibility of replacing these resistors with smaller ones is currently being considered. Nonetheless, because the electronics and ^{83}Kr calibration should remove any gain variations with fine scale structure within a particular sector, a gain equalization should be characterized by a single number. This can be determined by comparing the response of each sector to the same track. Relative gain constants can be determined from tracks that traverse the entire length of each detector. The cluster charge for such tracks can be plotted as a function of each individual sector, and normalized such that each has the identical response. This is shown in figure 5.11. However, the normalization is a point of some uncertainty. If all the cells are of identical length, there is no problem, as is the case for VTPC2. If the cells are not identical in length, as in the case of VTPC1, there is an additional complication. It is known that there is a dependence on the most probable value of an energy loss distribution with differing sample lengths [121]. This is shown in figure 5.12. In essence, this is due to the fact that the shape of the Landau distribution is altered as the sample length changes. For example, in the case of a measurement with an infinite sample length, normal statistics are attained; that is, $\frac{\text{Most Probable}}{\text{Mean}} \sim 1$. As the sample length is reduced, Landau fluctuations return, and the mean and most probable values are no longer identical. In the case of VTPC1, where there is a transition from 1.6 to 2.8 cm cells, this dependence is small and is neglected. However, this may become a concern if the VTPC measurements are to be combined with those from the MTPC where the cell size is 4.0 cm.

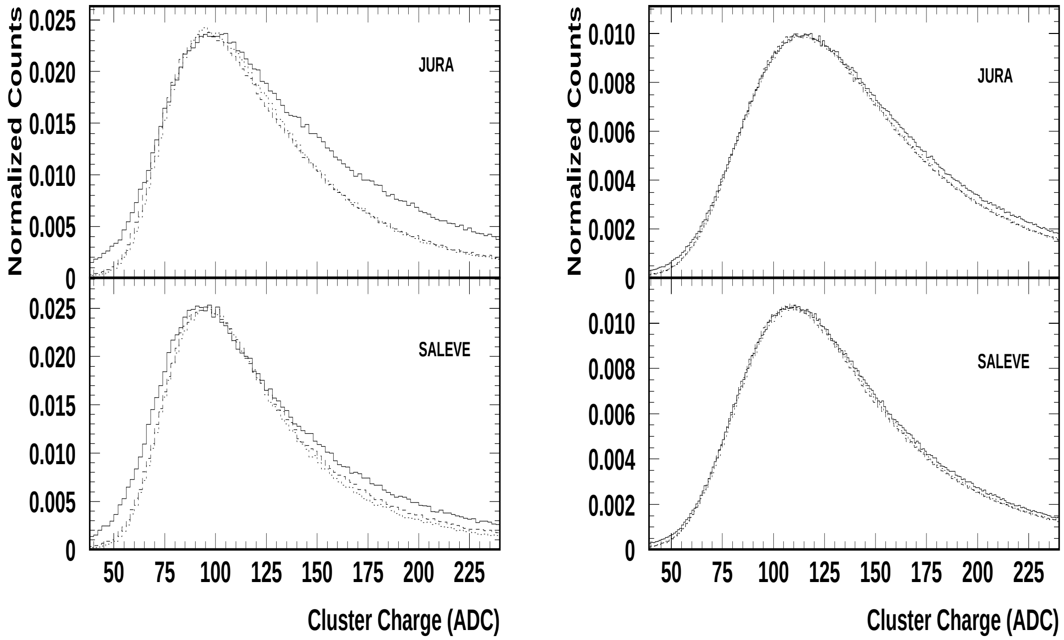

Figure 5.11: Response of VTPC1 (left) and VTPC2 (right) sectors after gain correction has been applied. Sectors 1 and 4 in VTPC1 (the closest to the target) have shorter pads than in the rest of the TPCs. This is evident in the width of the cluster charge distributions as they are somewhat wider than the other sectors which have longer pads. This is a good indication of the relative resolution of each detector.

It is also necessary to correct for charge loss due to the presence of oxygen and water in the gas volume. Small quantities of oxygen and water can enter the chamber via diffusion, and introduce a drift length dependence in the ionization measurements if not taken into account. Both are highly electro-negative and are able to attach free electrons to form meta-stable states, although the effect of water is 1-2 orders of magnitude less severe than oxygen at the same concentration. On the other hand, water has a particularly high rate of diffusion through mylar and was the dominant reason for construction of a double paned window. Water is relatively harmless in concentrations less than 20 ppm, and levels below 5 ppm were observed in all the TPCs. Oxygen on the other hand is a problem in any concentration above

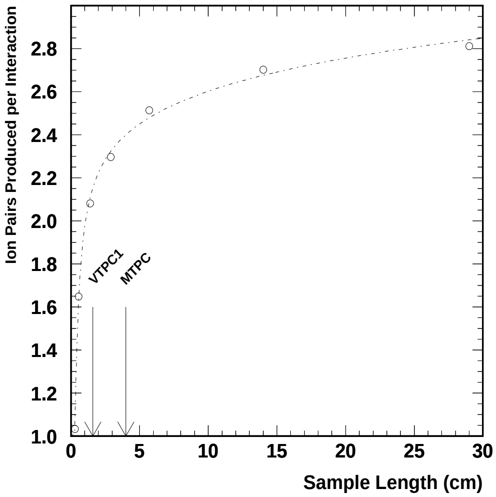

Figure 5.12: Most probable number of electrons produced in a single interaction over a varying sample length. This quantity is weakly proportional to the most probable value of the truncated mean distribution. The pad lengths of the pads in MTPC and the shortest pads in VTPC1 are shown. This data is derived from a calculation discussed in [121].

.2 ppm, especially if CO_2[2] is present in the gas mixture. Measurements made in the NA49 proto-type TPC showed a charge loss coefficient of 2.4×10^{-4} $\mathrm{ppm}_{O_2}^{-1}\mu\mathrm{s}^{-1}$ for a mixture of $NeCO_2$ (90:10). Oxygen concentrations were measured to be ≤ 4 ppm in the VTPCs and ≤ 2 ppm in the MTPCs. Given the operating parameters of the VTPCs, this implies a charge loss of approximately 2% per ppm of oxygen per meter of drift. This is corrected off-line.

Energy loss is also a function of environmental parameters which can vary substantially over the 4-6 weeks of the Pb run at CERN. Temperature variations are not a significant factor in the case of NA49 because the TPCs are housed in a climate controlled environment where the temperature variation is less than $\pm.1^o$. Pressure however, is another matter, since the chambers operate at atmospheric pressure and there can be appreciable variations over the course of a day. The amount of

---

[2] or a heavy hydrocarbon like isobutane: C_4H_{10}.

ionization varies by $\sim$.6% mbar^{-1}.[3] In order to remove this effect, the collected charge is normalized to a pressure of 970 mbar in all chambers for all runs. This has provided exceptional run-to-run stability in charge loss. Small variations still do exist which are most likely due to HV differences when chambers are turned on and off in the course of normal run conditions.

5.2.3 Software Effects

The most serious degradation of charge information is due to digitization. Any digitization involves imposition of a threshold, and the NA49 electronics carry out the digitization directly on the chamber. Since no bipolar information is available, it is difficult to correct for effects of base-line shift and variation of pulse shape. This is a concern for future experiments because there is an increasing amount of data-processing and reduction done "on chamber". Data compression and zero-suppression, which make it feasible to read out the TPCs, further degrade the data quality from a $\frac{dE}{dx}$ point of view. In particular, a significant drift length dependence in charge loss, outside any physical limits due to attachment processes, is observed when using the cluster finder method (PATREC chain) in charge quantification, whereas only a small variation is seen with the template method (TRANS), which fits clusters based on a parameterized PRF. This is seen in figure 5.13.

Utilizing a Gaussian PRF with a variable width (see equation 5.3) allows for a broadening of the cluster due to diffusion effects. Since the cluster finder has no information regarding diffusion, this probably accounts for a major fraction of the effect. However, the complete solution is more intricate since the total observed charge loss *can not* be accounted for by diffusion alone. The current cluster re-fit parameterization uses a Gaussian, which is believed to be a good approximation [85]. However, measurements made in a small NA49 proto-type chamber have

---

[3] Studies with the NA49 proto-type TPC have actually shown a non-linear dependence: $Q=Q_o(1-C\Delta p+.0033C\Delta p^2)$, where $C\sim.6\%$ mbar^{-1} and Δp is the deviation from a reference pressure.

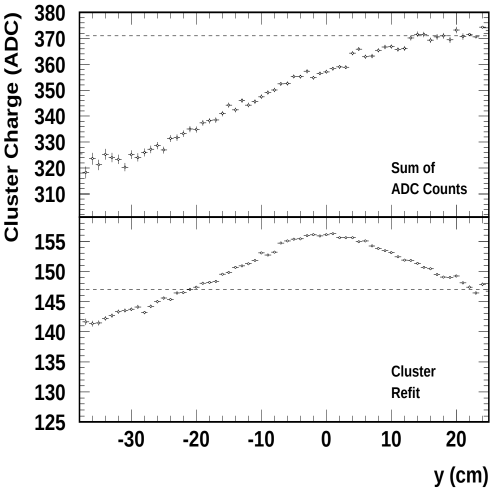

Figure 5.13: A different dependence on charge loss with drift length is seen between the two charge quantification methods. The cluster finder (top) simply sums all the ADC counts within the boundaries of an identified cluster while TRANS (bottom) fits a cluster to a parameterized PRF which allows for effects like diffusion (see equation 5.3). The offset in the cluster charge between the two methods is due to the $\sqrt{2\pi}$ constant that is left out in the calculation of the Gaussian integral with TRANS. The peak at the mid-plane (y=0) in the TRANS data can be identified with highly ionizing particles. See [122] for details.

shown larger cluster sizes (longer tails) than are observed in any of the NA49 TPCs. Figure 5.14 presents the best three parameter Gaussian and inverse cosh fits[4] to a measured PRF. The Endo function is much closer in form to the data than the Gaussian. In fact, the charge density profile that is induced on a cathode pad by an avalanche can be analytically calculated, and is the form of an inverse hyperbolic cosine. If the integral of the charge is calculated by integrating the two functions, the Gaussian fit only measures 93.4% of the charge as measured by the hyperbolic cosine. Also shown in the figure is a threshold drawn at 5% of the peak amplitude. This is a good approximation to the NA49 conditions as a threshold of ∼3-5 ADC counts is set where the MAXADC values generally peak at ∼60 ADC counts. With this threshold, the Endo function measures 96.8% of charge seen if no threshold exists.

---

[4] The inverse cosh is known as the Endo function [123].

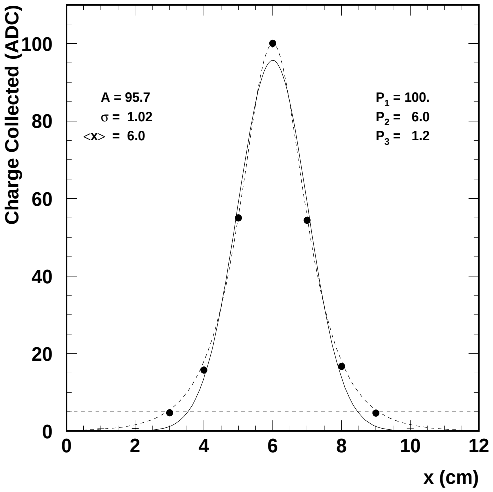

Figure 5.14: The difference between two pad response functions—a Gaussian (solid) and an inverse hyperbolic cosine (dashed) compared to experimental measurement with α particles in a small NA49 proto-type chamber. The fits are done using a conventional χ^2 minimization. Pads are 1.5 cm in width and pad-plane sense-wire spacing is .22 cm. A threshold is indicated at 5% of the value of the maximum signal height. This is a good approximation to the experimental conditions in the NA49 TPCs. Measurement by [124].

The Gaussian measures only 90.8% of the charge. This means that there should be a larger charge loss if a Gaussian form is assumed, unless the fit parameters are intentionally skewed to account for the offset (i.e. artificially increasing the width). This is an overly simplified picture as this refers to the situation of no drift, whereas it is necessary to understand the drift length dependence on charge loss. This is shown schematically in figure 5.15 where there is a fixed charge loss at zero drift and a linear increase in charge loss due to attachment, diffusion, etc. The expected charge losses in the NA49 TPCs are about 4% due to O_2, 4% due to threshold effects, and 2% due to diffusion. Although the data in figure 5.13 is corrected for attachment, the cluster finder charge loss remains at 24% which is excessive, while the losses that TRANS reports are far too small. This is currently under investigation. However, it is interesting that initial problems of low tracking efficiency with TRANS were traced to the rejection of tracks due to an anomalously high fraction of poorly fit clusters; that is, the fitted PRF was characterized by

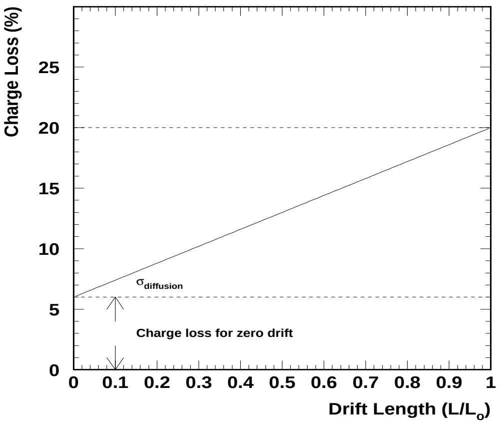

Figure 5.15: In an ideal case, a threshold would define the charge loss at zero drift and additional charge loss would be a linear function of the drift length with the diffusion coefficient defining the slope.

a large χ^2. Furthermore, it is known that the diffusion (σ_D) is dependent on the magnetic field strength [125]. Adding this dependence into equation 5.3 improved the $\frac{dE}{dx}$ resolution appreciably in both VTPCs. However, with the value of $\omega\tau$ in the VTPCs of ∼.6, this is not expected to be more than a 30% effect. No detailed analysis on tracking efficiency or cluster shape analysis was done on these events, so this is little more than conjecture at this point. However, it is interesting to consider that an overestimation of the cluster width may be offsetting the effective charge loss due to threshold effects. Nevertheless, the fact remains that if the PRF is better described by an Endo function,[5] a different amount of charge would be lost due to threshold effects than previously expected [127]. The differences in the $\frac{dE}{dx}$ performance are the subject of a detailed report by the author [122].

5.2.4 Definition of dE/dx

After correction of the charge information, there is a set of N ionization measurements. Currently there is a limited number of quality cuts for the VTPC clusters.

---

[5] and even better by the "Gatti" function [126].

This is because for the extremely short tracks, cutting 2-3 points per track can reduce the number of points by 10-20%. Initially it was thought to be important to keep the maximum number of points, even at the expense of a slight degradation in cluster quality. This is further discussed in section 5.3.2. With N samples, the problem of how to quantify the mean energy loss arises. The distribution of the multiple $\frac{dE}{dx}$ measurements along a track shows the high energy tail characteristic of a Landau distribution as illustrated in figure 5.10. The mean is an unstable characterization of such a distribution because it is sensitive to the large energy fluctuation in the ionization process. Because of the reduced sensitivity to high energy transfer processes in a real detector, the most probable energy loss is easier to characterize in a stable and reproducible manner.

A straight forward average of the N charge measurements that a detector provides will contain the large fluctuations of the Landau distribution and thus is not suitable. The first attempt to reduce these fluctuations can be traced back to 1954 when it was suggested by G. Igo and R. M. Eisberg to use only a subset of the total number of measurements [128]. This was found to reduce the fluctuations considerably. It was also suggested at this time that the mean energy loss could be deduced by use of a logarithmic mean [129], defined by:

$$< \frac{dE}{dx} >= \exp \left(\frac{1}{N}\sum_{i=1}^{N} \ell n(Q_i)\right) \tag{5.14}$$

This has the benefit of retaining all the data. However, its resolution was slightly worse than utilizing a truncation. By the early 1970s, the truncated mean technique was being used almost universally in quantifying $\frac{dE}{dx}$ and was further popularized by CERN work with PID at the SPS [130]. In this method a fixed ratio of the highest and lowest measurements are discarded for each track and a simple Gaussian fit to the remaining distribution. By truncating the larger values in a distribution, this method reduces the sensitivity to large fluctuations. Furthermore, it is computationally inexpensive, and although a single number cannot possibly contain all the information of a distribution,[6] the truncated mean is able to characterize the most probable value of the distribution in a stable and reproducible manner.

There are more complicated prescriptions in which the shape of the ionization distribution is also used in order to facilitate PID [131]. Such methods are based on calculating the maximum likelihood that a particle matches the profile of a Landau (or equivalent) distribution for the case of a pion, kaon, proton, etc. This is generally accepted as the most accurate method of PID. However, it has several drawbacks. Most serious is that for extremely thin absorbers (i.e. < 1 cm·atm), the Landau distribution tends to overestimate the high energy fluctuations [132]. With the form of the probability distribution uncertain, it complicates matters. Secondly, the fitting procedure is computationally expensive and unstable if several hundred samples are not available. The application of this method at NA49 is being studied by the author, but at present the truncated mean method is employed.

The optimization of the truncation ratio is determined experimentally by plotting the resolution, $R\ (=\sigma(\frac{dE}{dx})/<\frac{dE}{dx}>)$ as a function of the ratio, as shown in figure 5.16. Although there are slight variation with different materials, the ratio is generally optimal in the range where the top 60% (0:40 truncation ratio) to the top 40% (0:60) of points on a track are discarded. In the case of the NA49 VTPCs, a 0:50 truncation ratio was used because it had the smallest variation in the mean with the number of points on the track. This is described in detail below. The drawback of the truncated mean method is that a lot of data is left unused.

The resolution of ionization measurements expected from a multi-layer wire chambers filled with pure argon was parameterized by Allison and Cobb and generalized to any gas as [131]:

$$R = \frac{\sigma(\frac{dE}{dx})}{<\frac{dE}{dx}>} = .34N^{-.46}\left(\xi/I\right)^{-.32} \tag{5.15}$$

---

[6] After all, even a Gaussian requires 3 numbers to characterize it fully: amplitude, sigma, and mean.

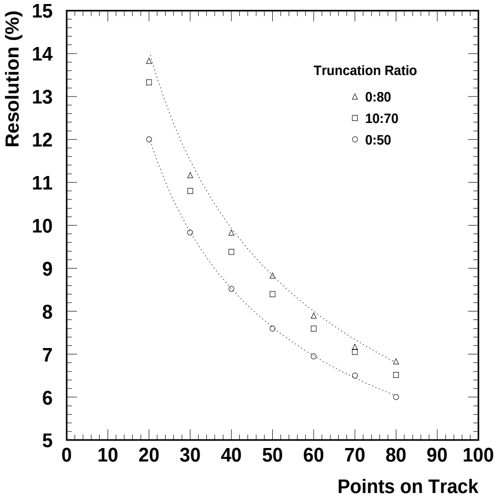

Figure 5.16: Expected Resolution as a function of the number of points on a track for several different truncation ratios.

where N is the number of samples and ξ/I is given numerically as 6.83νxP/Iβ^2 where ν is the mean number of electrons per molecule (∼11.4 for NeCO$_2$ (90:10)), x is the length of the sample (in cm), P is the pressure (in atm) and I is the ionization potential. This is similar to the form quoted by NA35 [133]:[7]

$$R = \frac{\sigma(\frac{dE}{dx})}{< \frac{dE}{dx} >} = .47(P \cdot D)^{-.32}\, N^{-.43} \tag{5.16}$$

except the dependence on the number of samples, N is slightly weaker. This weaker dependence was first found by Walenta who used a truncated mean algorithm in contrast to Allison and Cobb who used the maximum likelihood method [134]. It is noteworthy that the dependence of the resolution on the number of samples in both equations 5.15 and 5.16 differs from .5 that would be expected from a Gaussian distribution. However, it is the maximum likelihood method that most closely approximates Gaussian statistics. The expected resolution R, as given by equation

---

[7] A fit to NA35 data gave a form: R = .41(P·D)$^{-.32}$N$^{-.43}$.

5.16, is shown in figure 5.17 for the different NA49 TPCs.

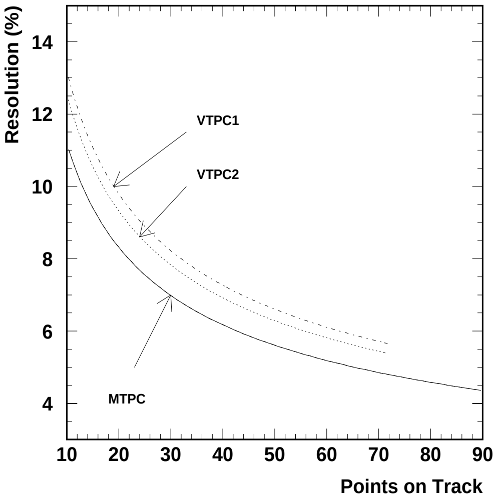

Figure 5.17: Expected resolution in the NA49 TPCs as given by equation 5.16. The same formula predicts a resolution of 3.2% if a particle crosses all possible pad rows (7.34 m·atm).

Because it is expected that the resolution varies with the number of points, it is necessary to ensure that the most probable value given by the truncation method is independent of the number of points. There is little variation in the number of active planes (pad-rows) a particle crosses for mid-rapidity tracks in the MTPC. However, due to the presence of the magnetic field, the number of points on a track varies greatly in the VTPCs, as shown in figure 5.18. This is more severe in VTPC1 than in VTPC2. In fact, the most probable $\frac{dE}{dx}$, as given by the truncation method introduces two effects which are illustrated in figure 5.19. The first is a systematic trend in which the most probable $\frac{dE}{dx}$ is overestimated for the shortest tracks. The second shows up as non-analytic discontinuities or a saw-toothed behavior where an underestimation in the $\frac{dE}{dx}$ by several per cent occurs when a track has a certain numbers of points.

The first effect can be understood purely from a statistics point of view. The ionization along a track is characterized by a Landau distribution which has a different mean and median value. There is a 50% probability of finding a value

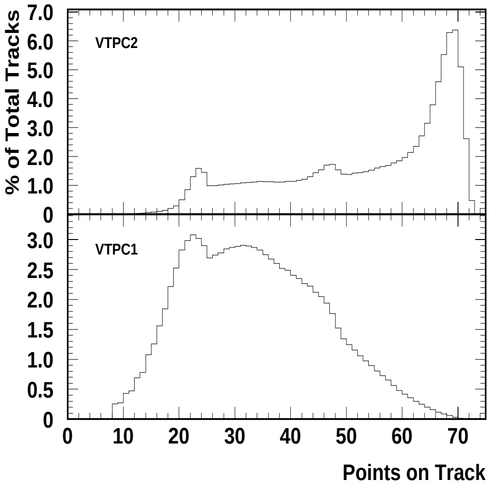

Figure 5.18: Number of points on tracks for the two VTPCs. The sector boundaries are clearly visible in each TPC.

above the median, *but* there is a much larger variance in the values above the median than below it. Thus a short track is more susceptible to large energy fluctuations than a longer track, and consequently a systematically larger $\frac{dE}{dx}$ is measured.

The second effect is a function of the truncation ratio and a consequence of careless handling of integer multiplication. An example illustrates this point. For a truncation ratio of 0:50, a track with $2n$ points will have n points used in the determination of the total charge deposited, and the truncated mean will be given by: $\frac{1}{n}\sum_i^n Q_i$. If another point is added to the track, the number of points used in the determination of the truncated mean should be $\frac{2n+1}{2}$. However, this is not an integer value and it is not possible to truncate a fraction of a cluster, so it is rounded down to n. As such the calculation is carried out as if the track is $2n$ points long in total, but the "extra" cluster can still affect the result. For example, if it has a charge greater than the $\frac{n}{2}^{th}$ largest cluster, it will be dropped in the selection of the $\frac{n}{2}$ smallest clusters, and will not increase the sum of the total charge, (Q_i) on the track, over that of the case if the track was only $2n$ points long. However, if the charge of the "extra" point is *smaller* than the $\frac{n}{2}^{th}$ largest, it will be used and the

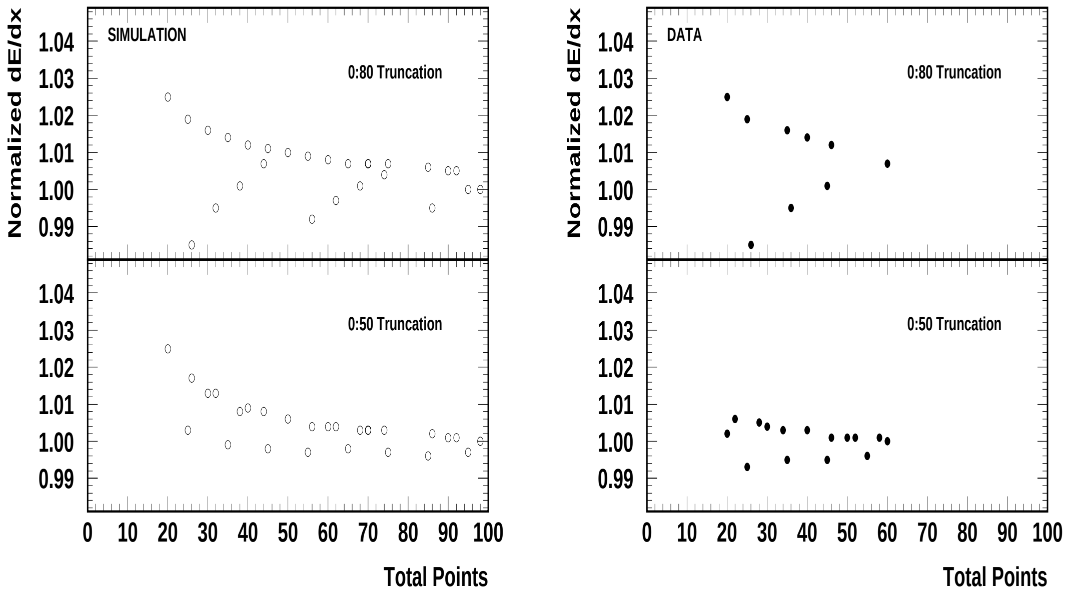

Figure 5.19: Effect of the truncation ratio on the number of points for both simulation and data. The $\frac{dE}{dx}$ is normalized to that obtained from a 100 point track for the simulation and to a 60 point track for the data. By utilizing the 0:50 truncation and using tracks with only an even number of points, less than a 1% variation in the most probable energy loss is attained.

total charge, (Q_i) of the track will *decrease statistically* relative to a similar $2n$ point track. This will consequently reduce the value of the truncated mean. Thus, if the calculation of the number of points to be truncated must be rounded to produce an integer number, the total track charge can be biased to be lower than a similar track that would have with an integer number of points to be truncated without rounding. For example, a 0:50 truncation ratio will introduce such a bias for tracks that possess an odd number of points while a 0:80 truncation does so for tracks where the number of points is not a multiple of five. This is shown in figure 5.19 for both simulation and experimental data. Tracks on which an integer number of truncated points are calculated without rounding fall on a smoothly decreasing curve with an increasing number of points, whereas tracks with any other number of points fall below the curve. Because this effect occurs for every truncation ratio, it is important to handle the “extraneous” points in a proper manner. Although this may be solved using some sort of interpolation algorithms, this is computationally expensive, and in fact, not necessary. In the case of the current implementation of the 0:50 truncation, it is always possible to arrange for a track to have an even number of points by disregarding, at maximum, a single (random!) cluster. This reduces the variation in the mean $\frac{dE}{dx}$ to less than 1% over all different track lengths within the NA49 VTPCs as shown in the bottom right panel of figure 5.19 with no further computational expense.

5.3 Performance

The primary aim of PID at NA49 was to deduce the ratio of kaons to pions ($\frac{K}{\pi}$) at mid-rapidity, and this was to be done in the MTPCs only. Although simulations had shown that a resolution of the order of 4% was necessary in order to separate π's and K's in the relativistic rise, this has yet to be attained. Most experiments, from ISR (ISIS) [135] and SPS (EPI) [130] to LEP [87] have had 100-300 separate ionization measurements available with which to attempt PID. It was not foreseen to utilize the $\frac{dE}{dx}$ information in the NA49 VTPCs on account of the poor resolution expected. However, it is the only method available for identifying electrons produced in the target.

Drift properties of the gas mixtures utilized in the NA49 TPCs were studied prior to data taking [89]. The $\frac{dE}{dx}$ properties are only being investigated now. Much work has been done in the past with Ar based mixtures and these can be used as a guideline. A tabulation of the ionization properties for some selected chamber gas mixtures close to that used in NA49 are included in Appendix D.

To quantify the $\frac{dE}{dx}$ performance of the VTPCs it is first instructive to look at the general properties of the cluster charge distribution within the detectors, and how it compares to simulation. Figure 5.20 shows a comparison of VTPC2 clusters (all tracks) with that expected from a Landau distribution. The Landau distribution is generated as explained in section 5.1 where a Poissonian and a E^{-n} distribution are

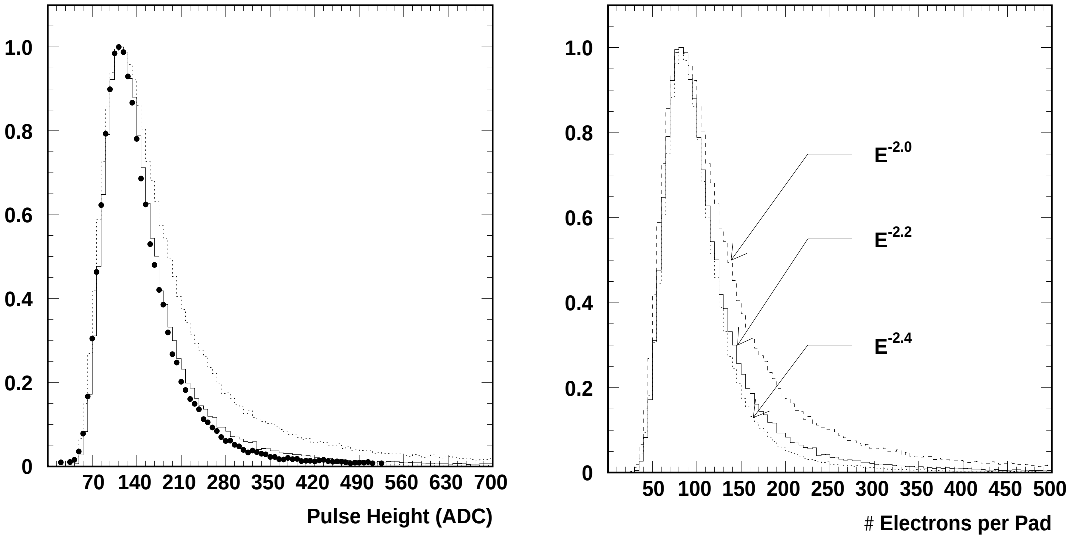

Figure 5.20: Cluster charge from VTPC (NeCO$_2$ (90:10)) compared against that expected for a Landau distribution. The Landau curve generated with a $E^{-2.2}$ seems to fit better than the quadratic. Shown at left is a comparison of several Landau distributions with a variation of the energy distribution as shown.

convoluted [141]. A Poissonian distribution with a mean of 12.4 primary electrons per cm is used (for Ne). If their energy distribution (i.e. E^{-n}) is given by n=2 which matches Ar based mixtures [142], the width of the distribution for the Ne data is overestimated. A much better fit is realized with n=2.2, which means there is a smaller spread in the energy. This is significant because the total number of electrons produced will have a smaller variance, even though the yield is less than in Ar. In principle this will improve the resolution over that predicted by equation 5.16. Thus, even though a better resolution would be expected from the high Z gases (i.e. Ar, Xe), because they produce the largest number of primary electrons (yield$_{primary} \propto$ Z^2), the mean number of electrons is better defined (smaller sigma) in Ne because of the smaller spread in the energy distribution. This seems to be a plausible explanation for the fact that the resolution is not governed by simple counting statistics. More intriguing is that fact that a recent measurement has shown that the energy dependence on the cluster size for He is well fit by E$^{-2.6}$

[114]. This is shown in figure 5.21. If no resolution degradation over that of argon and neon occurs, helium may be very attractive for use in experiments with high track densities (like relativistic heavy ion detectors), because it would minimize space charge in a detector. The main concern would then be gas-tightness of the containing vessel, ultra low-noise electronics, and stability of gas under high gas gain conditions. This is potentially the most serious because the onset of breakdown would render such a system useless. Another recent study has shown that resolution of the order of Ne and Ar is attainable with a He mixture [138].

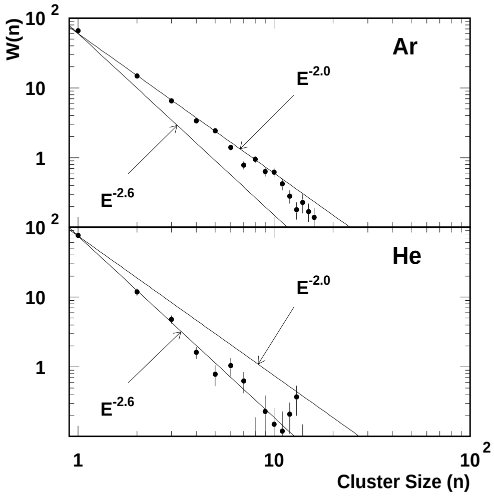

Figure 5.21: Experimental determination of energy dependence on cluster size. This implies that the width of the Landau distribution for He will be narrower than that of Ne. Data is from [114].

5.3.1 Extracting dE/dx

It has already been shown that the mean energy loss due to ionization is a function of the velocity ($\beta\gamma$) of a particle. As such if the $\frac{dE}{dx}$ is plotted in momentum bins, different particle species should separate into distinct peaks, if the resolving power is sufficient. The distributions of the most probable $\frac{dE}{dx}$ given by the truncated mean method in 1 GeV/c momentum bins for VTPC1 and VTPC2 are shown in figures 5.22 and 5.23.

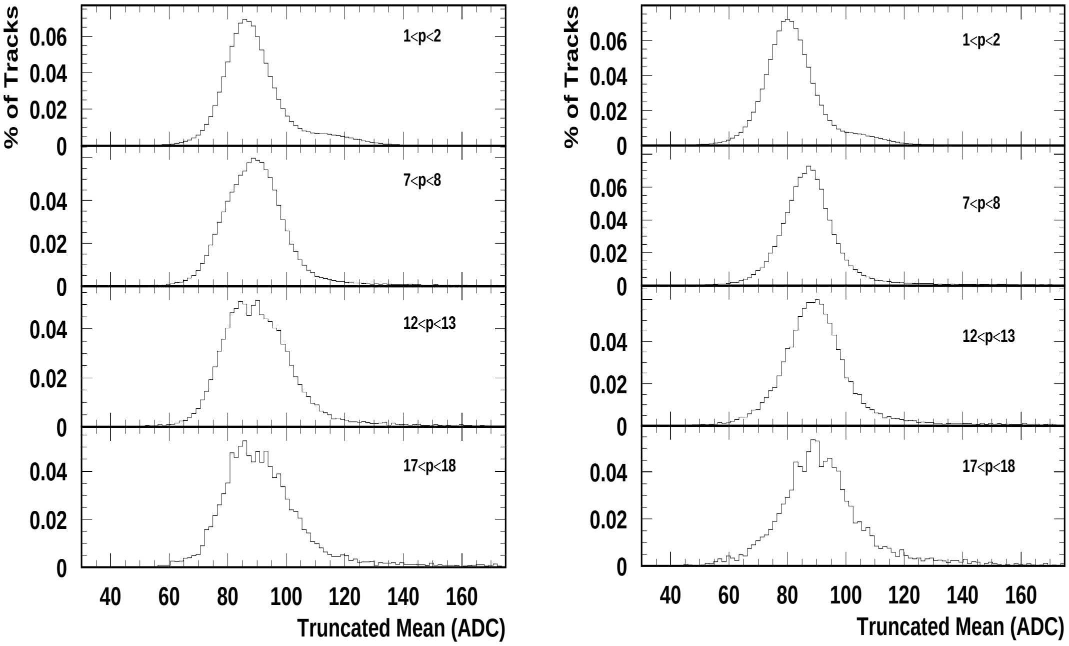

Figure 5.22: The distribution of the most-probable energy loss given by the truncated mean method for tracks within a 1 GeV/c momentum bin for the positive tracks on the JURA side of VTPC1 (left) and the negative tracks on the SALEVE side (right). Positives (negatives) on the SALEVE (JURA) side have been cut because the cluster widths are much wider on account of the oblique angles with which they cross the pads. Protons are evident on the JURA side by the broader distribution.

Although the peaks are not unambiguously separated, it is evident that there is a multi-peak structure. The approach that will be taken for the data analysis in this thesis is that there are three possible peaks, protons, pion, and electrons. Kaons will be ignored for now because the population of pions and protons are much larger and will swamp any signal. In the future, kaons identified with the TOF wall will provide a valuable calibration tool. No matter, with this assumption, any single momentum bin can be fit with two Gaussians. The fit is not expected to be perfect because it is an approximation to several Landau distributions. It is important to remember this because remnants of the Landau tail are still evident in a truncated mean distribution (i.e. a micro-Landau tail), even though a 0:50

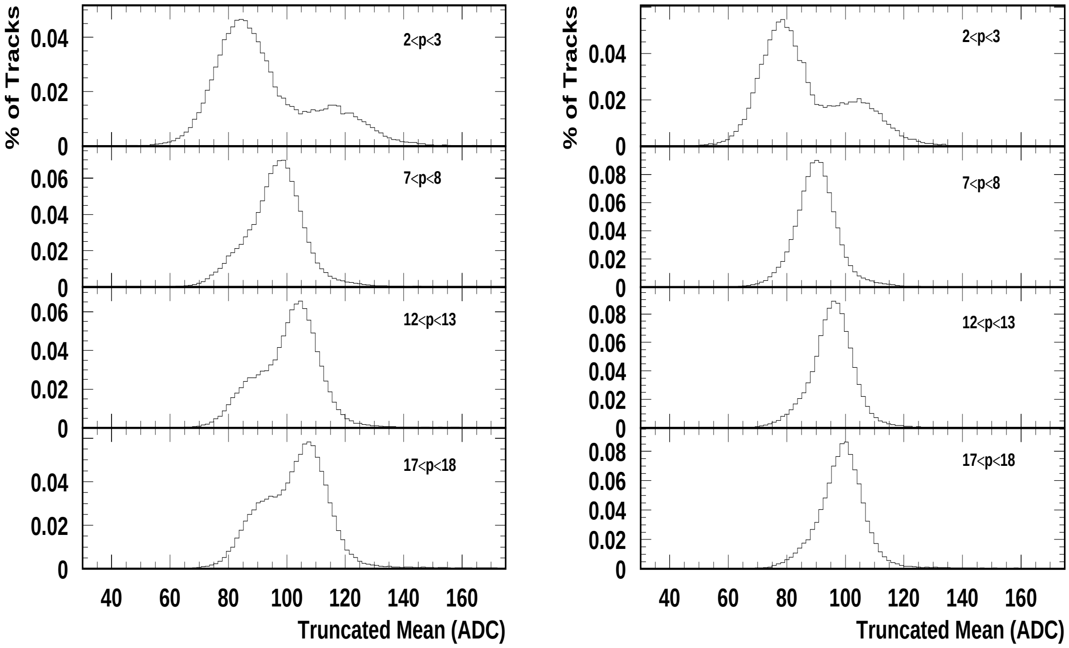

Figure 5.23: The same as figure 5.22, but for VTPC2. Protons are much more apparent in higher momentum bins. Large asymmetric tails on leading edge of the negatives is an indication of anti-protons. Resolution for tracks containing more than 20 points is ~7-8%.

truncation reduces this to a minimal amount. With the presence of such a tail, the Gaussian fitting procedure will tend to underestimate the resolution of one peak, and overestimate it on the other. This is illustrated in figure 5.24. Even in the simulation where the peaks are separated by the Rayleigh criterion,[8] a fit procedure using a χ^2 minimization is not able to extract the actual distribution. This is only expected to worsen if the peaks are more closely spaced. Nonetheless by consistently fitting a fixed number of Gaussians in fixed momentum bins, it is possible to characterize the shape of the relativistic rise in the detector.

For the data, the Gaussians are currently fit with three free parameters—amplitude, mean, and sigma. A two Gaussian fit in three separate momentum

---

[8] Peaks separated by at least 1.63σ.

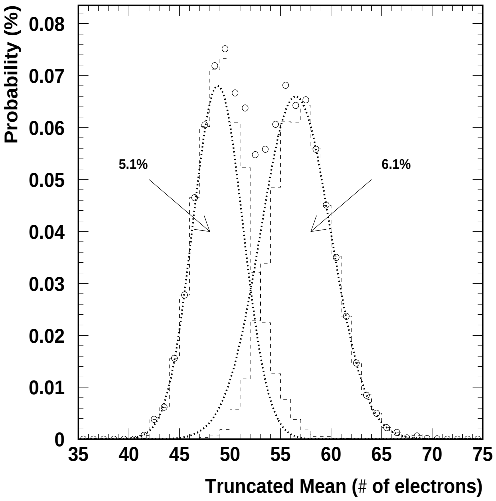

Figure 5.24: Two $\frac{dE}{dx}$ distributions that have a mean separated by 18% are generated with the same resolution. The dashed lines show the extension of each distribution while the open circles show the sum. The bold dotted line shows the Gaussian deconvolution of the distribution. It appears that this procedure is not able to reproduce the individual distributions. Both the leading edge of the first, and the trailing edge of the second distribution are well fit, but the micro-Landau tail skews the second distribution. The Gaussian deconvolution gives relative resolutions that differ by ~20%.

bins is shown in figure 5.25. The width should be constant, as the resolution is (theoretically) only a function of the number of points on the track. However, with the wide variation of track length in the VTPCs, leaving it free is a good check on the stability of the fits. In fact, this quantity does stay relatively constant over the momentum range of the detector. This is shown in figure 5.26.

The value of the truncated mean is assigned as the most probable $\frac{dE}{dx}$ for each momentum bin. This can then be compared to the Bethe-Bloch equation which has been explained in section 5.1. An oft used parameterization for the most probable value of energy loss is followed [143]:

$$-\frac{dE}{dx}_{(mp.)} = \frac{\alpha t}{\beta^2}[\ell n(\frac{m_e \alpha t}{I^2}) + .891 + 2\ell n(\beta\gamma) + \beta^2 - \ell n(\beta^2) - \delta] \tag{5.17}$$

where $\alpha t = .153\frac{Z}{A}\rho\, t$; ρ is the density of the medium (ρt in g cm^{-2} where $\rho = 1.203$ gcm^{-3} for NeCO$_2$ (90:10) and t is the pad length). The ratio $\frac{Z}{A}$ is taken to be .5 for NeCO$_2$;

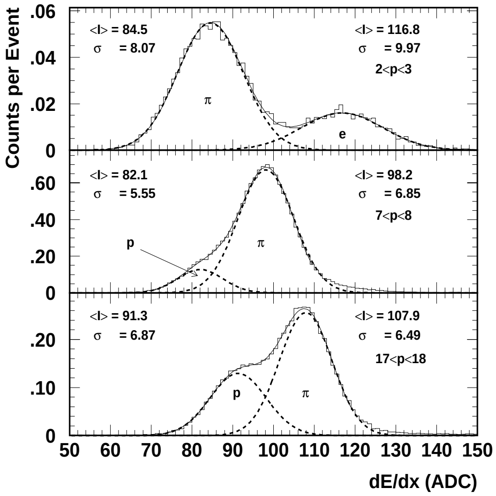

Figure 5.25: Multi-Gaussian fits in three separate momentum bins showing the mean ionization, <I> and the width, σ for each.

and the ionization potential I is 21.6 eV. The parameterization of the plateau (i.e. δ) follows equation 5.9, where $X = \log_{10}(\beta\gamma)$, $X_o = .53$, $X_1 = 3.7$, and $m = 2.22$. X_o parameterizes the onset of the density effect, X_a describes the point at which full saturation sets in and X_1 is the point where the saturation completely cancels the rise. In general, $X_a < X_1$. Results for the VTPCs are shown in figure 5.27.

What is observed in VTPC2 is that the shape of the relativistic rise appears different on the two sides of the detector. This is puzzling because the TPC halves are of identical construction and are contained in the same gas vessel. It therefore raises suspicion that the magnetic field may introduce a spurious effect. In fact, due to the presence of a magnetic field and the crossing angles of the tracks with respect to the sense wires, the width of the charge clusters is expected to be different on opposite sides of the beam. It is due to the presence of the strong radial **E** field of the sense wires and is known as the "wire $E \times B$" effect [84]. It is illustrated schematically in figure 5.28. This is potentially serious if a fixed cluster width, as outlined in equation 5.3 is used in quantifying the amount of charge deposited in each cluster.

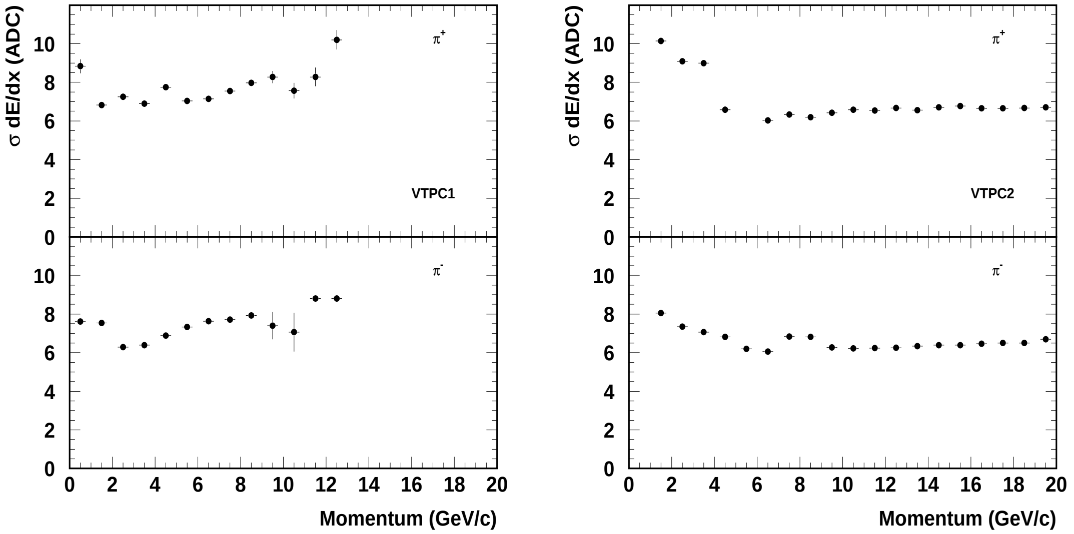

Figure 5.26: The width (σ) of the truncated mean distributions, from an unconstrained three parameter Gaussian fit, for tracks within a 1 GeV/c momentum bin in VTPC1 (left) and VTPC2 (right). The magnitude of the width is sensitive to the selection criteria of the tracks, but the relative differences do not change.

In the active volume of the TPC the drifting ionization (electrons) follow the straight uniform electric field lines created by the field cage. As shown in figure 5.28, the electrons drift into the page towards the pad-plane (x-z plane). Once the electrons pass the upper bound of the field cage—the FG—they come under the influence of the radial electric field of the sense wires which is quite strong ($\sim 10^4$ V cm^{-1}). If the trajectory of the drifting ionization projects onto a sense wire, as those created at point 1 in figure 5.28, the radial electric field will not alter the direction the motion and there is not asymmetry in behavior on opposite sides of the detector. However, if the trajectory of the drifting electrons *do not* project onto a sense wire, as those produced at positions 2 or 3, the radial electric field of the sense wires will cause the trajectory of the ionization to be altered in order for the ionization to be collected on the sense wire. As such the ionization necessarily acquires a velocity component in the z direction and the Lorentz force will either extend or contract the region in which the ionization is collected and amplified on

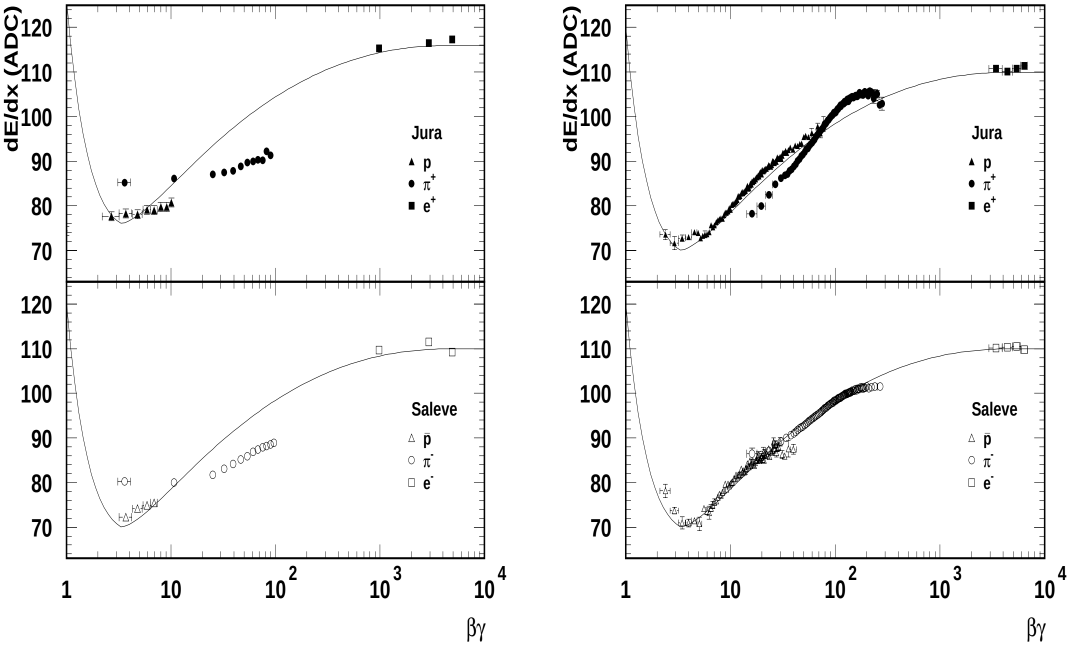

Figure 5.27: The relativistic rise in VTPC1 (left) and VTPC2 (right). The ratio of the peak to minimum is 1.57 for both chambers.

the sense wire, depending on the direction of the magnetic field. This will in turn alter the width of the measured charge cluster. It should be stressed that the altering of the trajectory of the ionization only occurs in the small region between the FG and sense wires, but can be appreciable because of the large values of the electric field in the amplification region.

If the "wire $E \times B$" effect was the cause of the difference in the relativistic rise between the two sides of the detector, the behavior should be reversed upon switching the polarity of the magnetic field. However, this is contrary to what is observed experimentally where the effect stays with the side of the chamber [144]. This also implies that the problem is not a consequence of the asymmetry of the field components, nor the simple deconvolution utilized, but rather an inherent property of the chamber. This is not understood at present.

VTPC1 presents an even more challenging environment to extract $\frac{dE}{dx}$ because of the large variation in track length and its sensitivity to low momentum particles (see

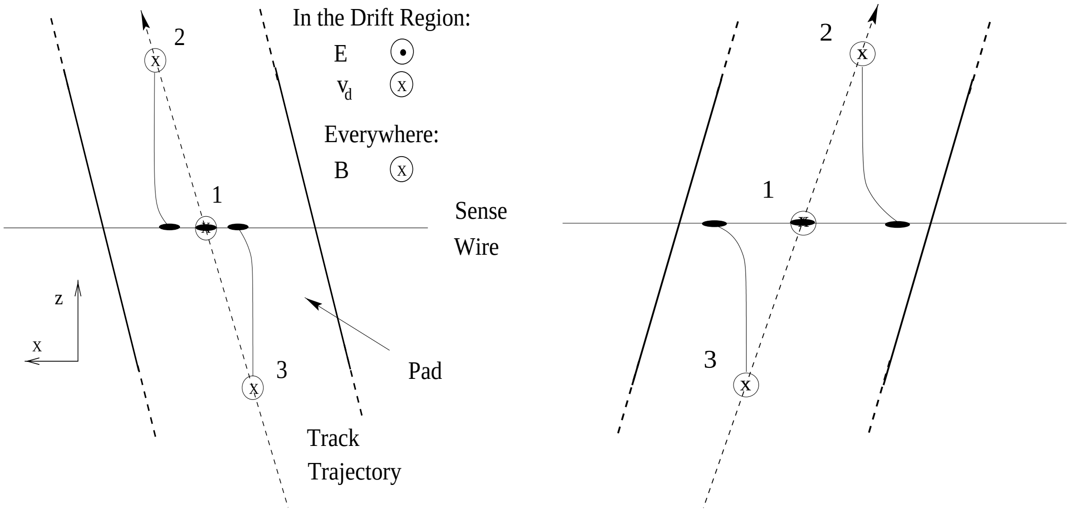

Figure 5.28: The "wire $E \times B$" effect can introduce a systematic difference in cluster width in the presence of a magnetic field depending on the geometry of the read-out chamber and track trajectories. Shown at positions 1, 2, and 3 is ionization produced along a track trajectory that is drifting towards the pad-plane (x-z plane). After the ionization passes the Frisch grid, it changes direction to follow the field lines of the radial **E** field of the sense wires. Because tracks on opposite sides of the beam line cross the sense wires at different angles, the Lorentz force can cause a modification of the cluster width from that expected in a field free region. Currently, the same cluster width is used independent of the detector side.

figure 5.4) which means there is little difference in ionization yields between particle species. It must also be remembered that no krypton calibration was available for VTPC1 in 1995 which also degrades performance. This will be addressed when the 1996 krypton data is fully analyzed. However, even with these problems, an initial goal of low momentum electron identification and rejection is still feasible.

It is possible to see electrons very plainly in the momentum region below 3 GeV/c. Conversions in the target and Dalitz decays are the most likely candidates for such particles. Protons are also evident. However, figure 5.27 indicates that the rise is rather flat. A possible explanation for this is the way the correction for the cell crossing angle was done. The tracking reconstruction assigns two emission angles of the track—β and ϕ as defined in equation 5.3, and these are used as the cell crossing angles. For high momentum tracks measured in VTPC2, these are essentially constant over the length of the track. However, in VTPC1, the magnetic field bends the tracks strongly on account of their relatively low momentum, and the curvature of the track changes a non-negligible amount over its length. This effect will be investigated in the near future.

It should be mentioned that the protons and anti-protons were isolated and fit in both VTPCs using a high p_T cut (i.e. selecting particles with $p_T > 400$ MeV/c). This increases the number of protons relative to the number of pions in a momentum bin. Although the fit values derived in this manner fall on the Bethe-Bloch curve, there is a shift in the $\frac{dE}{dx}$ value as opposed to when no p_T cut is imposed. This is shown in figure 5.29. This has an adverse effect on the pion (and proton) peak as there is a 1-2% shift upward in $\frac{dE}{dx}$ with this cut. The same effect is observed in VTPC2 and has been traced to the crossing angle of the tracks with respect to the pads. There are two classes of tracks and they appear to exhibit different energy loss characteristics. Wrong-side tracks are particles emitted in the hemisphere opposite

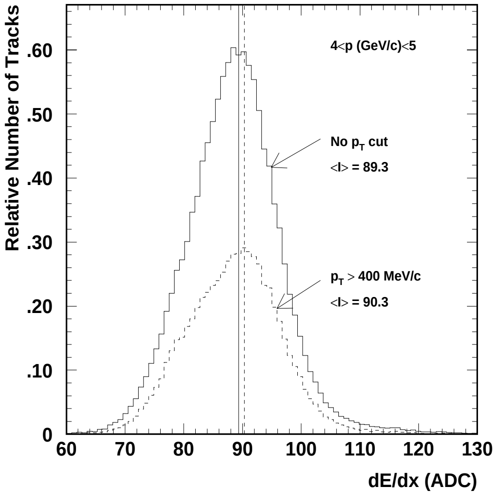

Figure 5.29: The distribution of the truncated mean for all positively charged tracks with the momentum bin of 4-5 GeV/c in VTPC1. The mean value of the distribution as fit by two Gaussians shifts by ∼1% when a p_T cut is imposed. A similar effect is seen in VTPC2 with the shift being slightly larger.

to which they will end up after being bent by the field.[9] Such tracks do no enter the TPC volume at the optimum angle; that is, the angle between the trajectory or the track and the pad (see β in figure 5.3) is larger for a wrong-side track than one emitted in the normal direction because they have traversed a longer path length through the magnetic field and have been bent a larger amount. Because they cross the pads at steeper angles, they leave more ionization and therefore produce a higher $\frac{dE}{dx}$. The question of whether this class of tracks requires separate treatment will have to be addressed soon. With all the subtleties mentioned above, one should not forget that VTPC1 covers the momentum region where the ionization goes through its minimum values which also reduces the separation power. This is illustrated in figure 5.30.

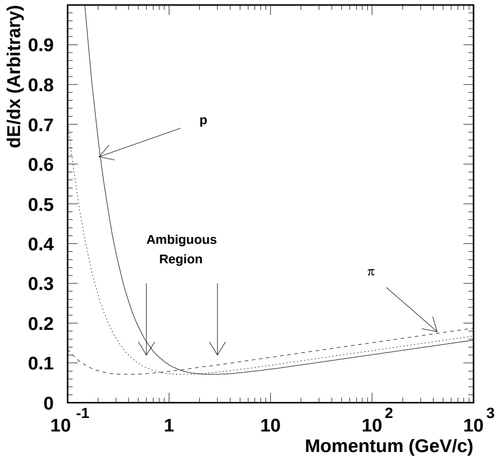

Figure 5.30: Another reasons for the poor response attained in VTPC1 is all the particle species go through a characteristic minimum in its momentum range. Shown is the relative $\frac{dE}{dx}$ for protons (solid), pions (dashed), and kaons (dotted). In the region from .5<p (GeV/c)< 3, there is an ambiguity in PID from $\frac{dE}{dx}$ measurements. It is in this region that TOF information can help resolve the ambiguity as there is acceptance down to p = 2GeV/c.

It is important to realize that the criterion to be optimized in doing ionization measurements is not really the resolution but the separation power; that is, at what

---

[9] Such tracks usually carry a high transverse momentum. Figure 5.35 contains an example of a "wrong-side" track.

confidence level can a particle be identified. Although resolution is closely related to this quantity, it is not the same. The intrinsic resolution of an experiment is basically defined by the operating point of the detector and its geometry. For example, the operating point of the detector (HV) defines the maximum pulse height (MAXADC), and the read-out plane geometry fixes the width of the cluster. This is used in a cluster re-fit algorithm as in equation 5.3. For VTPC1, the results are shown in figure 5.22 where resolution is typically ~8%. Although protons are evident in these plots, the separation power is not very high. We can quantify the pion-proton separation power with:

$$S_{\pi-p} = \frac{(\frac{dE}{dx})_{\pi} - (\frac{dE}{dx})_{p}}{\sigma(\frac{dE}{dx}_{\pi})} \tag{5.18}$$

From this expression the expected separation power in VTPC1 is 2.21 in the momentum bin from 3-4 GeV/c, and decreases to 2.0 for p=4-5 GeV/c. For VTPC2, in the 12-13 GeV/c momentum bin of figure 5.23, a separation power of S=2.48 is found. When a p_T cut is made (i.e. p_T >400 MeV/c), it enhances the number of protons with respect to the number of pions—as shown in figure 5.31. With this cut, the resolution improves to 7% yet only a slightly higher separation power is calculated—2.63.

Similarly, a high degree of electron-pion separation to be obtained in both VTPCs; even VTPC1 where no krypton calibration is available (yet). A separation of S=2.6 in VTPC1 and S=5.0 in VTPC2 is expected. Low energy electron rejection (i.e.<3 GeV/c) should be possible at or above the 90% level in both VTPCs. Of course above this momentum, it will be worse.

One last note. Because VTPC1 covers the low momentum region, it will also supply information on particles in the $\frac{1}{\beta^2}$ region of the energy loss curve. Figure 5.32 shows evidence from a small event sample of low momentum protons (and deuterons) in VTPC1.

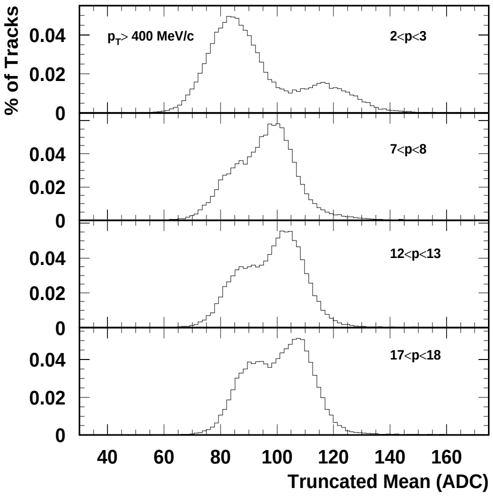

Figure 5.31: Resolution is as much a function of the offline cuts as of the detector operating parameters. Shown is the same plot as in fig 5.23 but with a p_T cut as indicated. Such a cut is useful in isolating a higher purity proton sample. It is evident that the protons are more prominent in these plots.

5.3.2 Improvements

The problem with the steep crossing angles in VTPC1 as well as the lack of Kr calibration constants has already been mentioned. There is also a slight concern with the run to run stability. The only physics reason for such an effect is a varying HV. However, even with no run dependent corrections, the $\frac{dE}{dx}$ of the VTPCs is stable to less than a couple per cent. The inclusion of run to run parameters will need to be addressed shortly. There is also a need to implement a fixed width for the fitting of the truncated mean distributions—once a suitable value is determined. This is dependent on finalizing the cluster re-fitting algorithm.

Currently there is little attention paid to the quality of the clusters on tracks. This includes whether a cluster is merged with another (i.e. clusters overlapping), or if it lies on the boundary of a sector, occurs near a saturated pad, etc. In the next stage of analysis, these quality issues will be of high priority. One of the first is the cluster shape. A simple ratio of the cluster charge to the MAXADC value of the cluster produces an interesting effect, which is illustrated in figure 5.33.

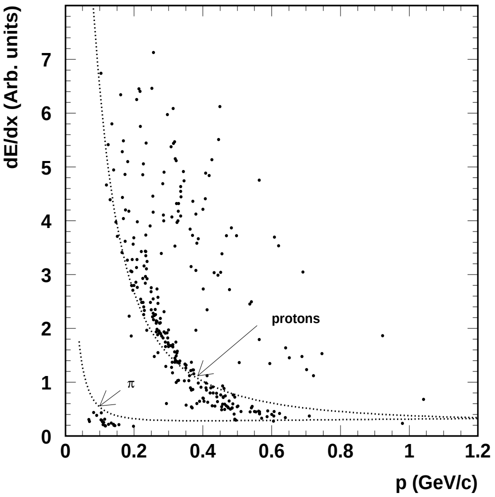

Figure 5.32: The energy loss spectrum in the low momentum region in VTPC1, along with the approximate Bethe-Bloch curves for pions and protons. These event were produced with another analysis chain, but serves to illustrate the capability of low momentum identification.

It appears that there are two distinct classes of clusters. The "suspect clusters", which are characterized by a large value of the ratio G=$\frac{\text{cluster charge}}{\text{MAXADC}}$, make up 2-5% of the total number of clusters on tracks. Although these clusters have a high enough charge that they are discarded in the truncation procedure, they do have a role in determining the number of points to truncate. Cutting these high charge clusters before the calculation of the number of points to use in the truncated mean calculation systematically reduces the $\frac{dE}{dx}$ of tracks by 2-3%. This requires further study.

Global tracking (i.e. track matching between detectors) will allow more flexibility and better precision. Longer tracks will be available which should increase the resolution. There is a concern that combining results from the various detectors may be problematic. However, if corrections within a single detector are done correctly, inter-detector calibration should be characterized by a single number—a relative gain constant. There is little difference between the shape of the relativistic rise in the two gases [145]. The most challenging problem that is foreseen is how to combine the data of VTPC1 and MTPC since there is almost a factor of 2 difference

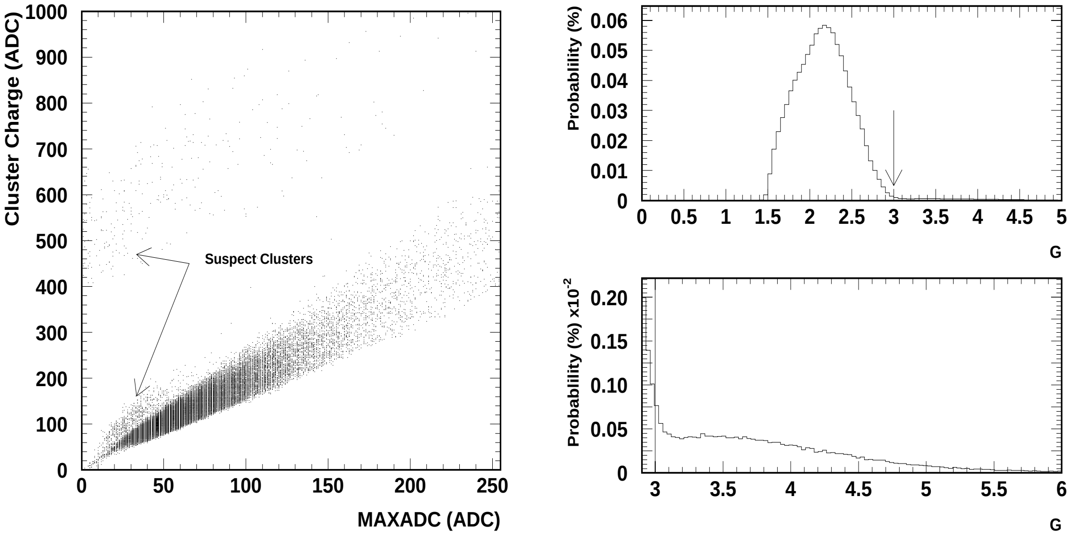

Figure 5.33: Shown at left is the cluster charge versus the MAXADC value. Most clusters fall into a band defining a linear relation between the two quantities, however there are two regions populated with a large total charge for the MAXADC values. Both cluster types are currently used in the truncated mean calculation. At right, the ratio G ($=\frac{\mathrm{ClusterCharge}}{\mathrm{MAXADC}}$) is shown for the same clusters. The majority of the clusters have G $<$ 3. The "Suspect Clusters" at right are identified with G $>$ 3.

in the length of the ionization samples. Because of the larger fluctuations expected for the shorter pads in VTPC1, combination of the detectors will most certainly lead to a reoptimization of the truncation ratio. First results from the global tracking do show a correlation between the $\frac{dE}{dx}$ in VTPC2 and MTPCs. This is shown in figure 5.34 However, with the "flat rise" in VTPC1, more work is required in this area. With the global tracks, TOF information will be available for a certain class of tracks. This will not only allow calibration of the VTPCs with identified particles, but also extend the use of $\frac{dE}{dx}$ information to tracks that have a small number of points in any one TPC, yet have a significant track length when information from all TPCs is combined. This is seen in figure 5.35.

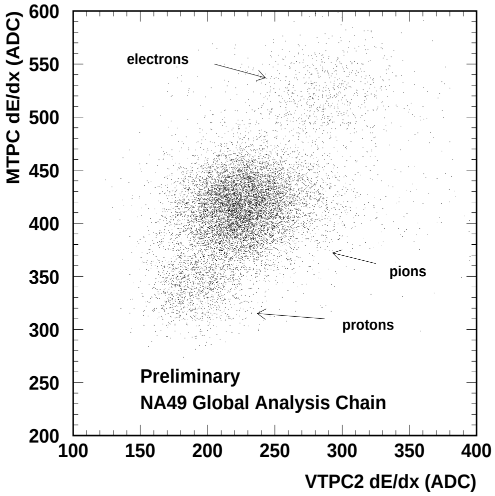

Figure 5.34: The correlation between $\frac{dE}{dx}$ in MTPC and VTPC2. These are preliminary results from the NA49 “Global Chain”. First results shown at [146].

5.3.3 What Can We Do Now?

In terms of identified particles, the least demanding physics quantity that can be extracted is the ratio of yields of particle species. In order to deduce identified particle yields, the Gaussians of figures 5.22 and 5.23 need only be integrated. A ratio removes any need for acceptance and efficiency calculations as it can usually be assumed that these quantities are identical in both channels. Furthermore, PID on a statistical rather than track by track basis is sufficient. As such identified spectra in this context are quite feasible at this stage. For HBT spectra on the other hand, it is necessary to have a measure of the identity of each track. This is much more difficult than statistical identification and at this point in time, it is probably too ambitious to talk of fully identified HBT spectra. However, the present capabilities should allow the analysis of electron free HBT spectra. This is especially important in the backward region of rapidity space (VTPC1). Furthermore ‘$+-$’ correlations, which are used to deduce Coulomb corrections can now be deduced with a reduction in the proton population. It should also be possible to draw qualitative conclusions on effects of PID on HBT spectra and extract preliminary

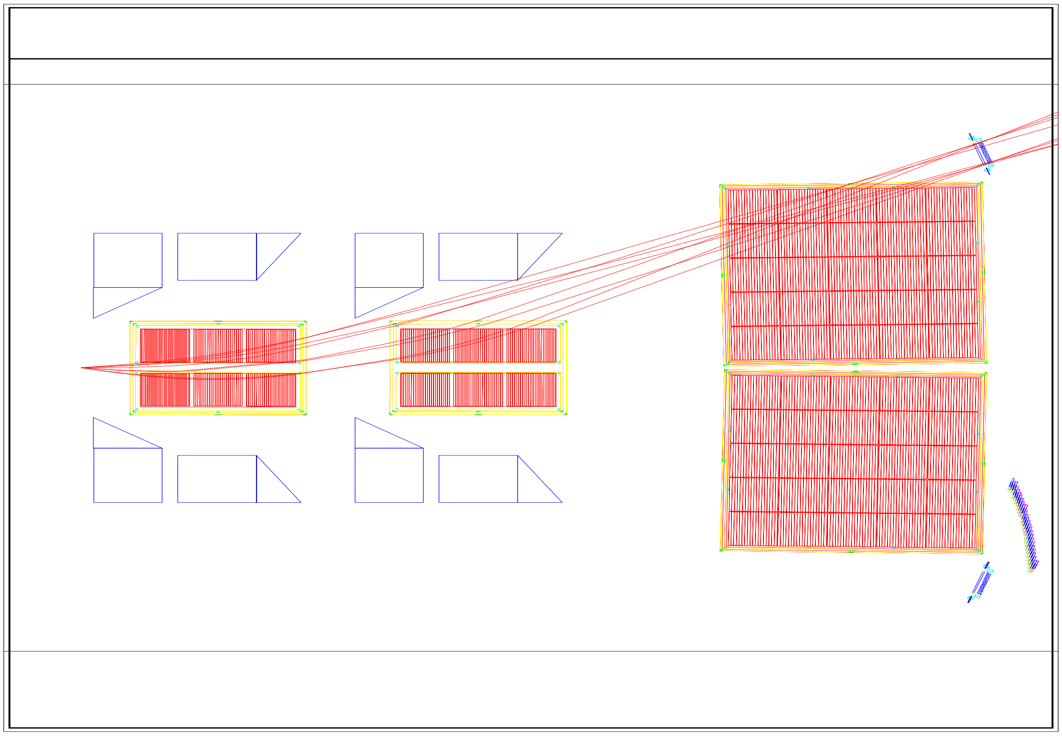

Figure 5.35: Particles for which combining $\frac{dE}{dx}$ information in different chambers will increase resolution dramatically. The TOF-R2 and TOF-L2 walls should enhance particle separation in the 1-3 GeV/c region appreciably. Shown are 2 GeV/c pions with a transverse momentum of 600 MeV/c. Also an example of a "wrong-side" track is illustrated—one that starts off on one side of the beam-line and crosses over to the other.

'++' correlations—both for protons and pions. Although ambitious in scope, the effect of particle composition in large regions of phase space have been hitherto unexplored. As such, it is interesting to make such an attempt; this will certainly not be the last word.

The second goal of the thesis is to put forward a method for extracting correlation radii from single events. Again using PID, electron and proton contributions can be reduced. With no protons, it will be possible to combine the positive and negative pions, doubling the statistics in the numerator of equation 3.12. In any case this thesis will be the first attempt in HBT correlation studies at the event level, which should reach maturity at future experiments; most notably, STAR and ALICE.

Chapter 6

HBT Analysis

The ultimate goal of HBT investigations at NA49 is to produce a meaningful event-by-event HBT radius parameter. The reason this is important is that most observables give information that is related only to the dynamics of a system. These observables include multiplicity, which measures entropy; transverse momentum, which is a measure of the temperature; the $\frac{K}{\pi}$ ratio, which is a measure of the chemical potential, etc. None of the above give information on the geometry, or physical size of the source. This kind of information would allow another type of event characterization to be made in probing for event-by-event fluctuations; after all, volumetric information is very important in characterizing properties of any phase. Nonetheless, before this goal can be achieved, a much better understanding of the correlation functions must be obtained. This centers on how Coulomb effects and particle contamination in the sample (contributions of finite number of "non-identical" particles), affect the correlation function as well as the obvious question of how to physically construct a meaningful correlation function from a single event. This chapter will attempt to illustrate the effects of the Coulomb correction and PID in π-π correlation functions, as well as give the first results from an entirely new method of deducing radii parameters which is not dependent on a fitting algorithm.

6.1 Construction of a Correlation Function

In chapter 3, a theoretical expression for a two particle correlation function was defined in terms of probability distributions of multi-particle spectra. Experimentally, one does not measure probabilities directly, but rather yields or cross-sections. Since these quantities are proportional to the probabilities, one is able to substitute them into equation 3.12 obtaining:

$$\mathbf{C}_{exp}(\mathbf{q},\mathbf{K}) = \mathbf{N}\,\frac{\mathbf{Y}_i(\mathbf{p}_1,\mathbf{p}_2)}{\mathbf{Y}_i(\mathbf{p}_1)\mathbf{Y}_i(\mathbf{p}_2)} \tag{6.1}$$

where $\mathbf{Y}_i(\mathbf{p}_1,\mathbf{p}_2)$ denotes the yield of a pair of the i^{th} particle species with momentum $\mathbf{p}_1$ and $\mathbf{p}_2$, relative momentum $\mathbf{q}$ and average momentum $\mathbf{K}$. The normalization $\mathbf{N}$, denotes a factor such that the correlation function is defined to be 1 at large relative momentum. Because the correlation is defined in terms of a ratio of the number of pairs of particles, it is referred to as *intensity interferometry.*

6.1.1 The Data Set and Event Selection

The data set available for this analysis is approximately 87k events from nine separate runs acquired in the 1995 Pb-Pb run—50k in the STD+ magnetic field configuration and 37k with the opposite polarity (i.e. STD–). The average multiplicity of each event is of the order of 800, so this means approximately 90k pairs of like-sign particles are contained in every event or $\sim 10^9$ pairs in the total sample! As mentioned previously, only tracks reconstructed in the VTPCs will be considered.

After the event reconstruction is completed (described in chapter 5), particles may be selected in order to construct a correlation function. The selection criteria is defined at three different levels; the event level, the particle level, and, the particle pair level. Because we are ultimately interested in constructing a correlation function at the event level, any cuts will be as soft as possible so the maximum number of particles per event is retained. The cuts are described below.

6.1.1.1 Event Level

There are two problems at the event level, the first of which is pile-up. This occurs when more than one interaction occurs within the time that the detector is being read out. In essence multiple interactions are recorded in the span of a single trigger. Particles from different events will not correlate, and this can reduce the correlation strength. If the incident beam flux is of the order of 100k ions per second, the average time between each Pb ion delivered by the accelerator is approximately 50 μs.[1] This is the fastest rate at which real Pb-Pb interactions can occur, and since it takes 52 μs to read out the TPC, this is not a large problem. The second concern is the finite range of the impact parameter in collisions recorded at a single trigger setting. This is more severe in small acceptance experiments where in order to produce a reasonable interaction rate, the trigger threshold must be relaxed. NA49 has the luxury of requiring a very hard central trigger, because the DAQ system is limited to no more than 32 events per spill. Using a 1% target and selecting only the most central events (i.e. $\sim$4% of the inelastic cross section or events with an impact parameter of $\leq$4 fm), 13-24 events per spill are triggered upon. Because of the strong constraints at the trigger level, no cut on multiplicity is required to further reduce the variation in centrality. It is already a factor of 3 smaller than any competing experiment. The multiplicity distributions for a single run of 10k events is shown in figure 6.1. In order to limit any pile-up problem, only events that have a multiplicity more than 3σ above the mean were disregarded. It is important not to make this cut too stringent as to remove events with real fluctuations. However, in the construction of ensemble correlation functions this is not as large a concern as these occurrences should make up a miniscule fraction of the total number of events. Similarly in terms of an event-by-event correlation function, pile-up should be detectable by a reduction in the correlation strength parameter λ. If the correlation function is unable to do this, there is not much hope

---

[1] For the runs under consideration the incident flux varied from 50-85k spill^{-1}.

that it will be sensitive to smaller more subtle effects that may indicate a phase transition to a QGP.

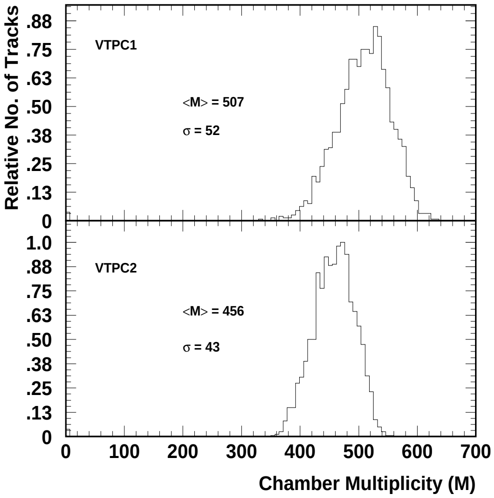

Figure 6.1: The multiplicity distribution in each VTPC in a set of 10k events.

6.1.1.2 Particle Level

The selection criteria at the particle level make up the bulk of the cuts. The most obvious selection is that of charge; only one sign is taken in order to construct the correlation functions. The second is an acceptance cut. The acceptance of the NA49 spectrometer for pions is shown in figure 6.2. If a particle does not fall within the boundaries as defined in figure 6.2, it is removed from the sample. A cutoff at 2 GeV/c in transverse momentum is imposed because the tracking efficiency begins to decline beyond this point. It is also true that the tracking efficiency in VTPC1 is not optimal at this time, and begins to decrease severely in the rapidity region below y_{lab}=2. As such, no attempt was made to construct a correlation function in a rapidity region below this, although it is foreseen in the future. An estimate of the tracking efficiencies are shown in figure 6.3. These are calculated by embedding Monte Carlo generated tracks in the raw data of events and carrying out event

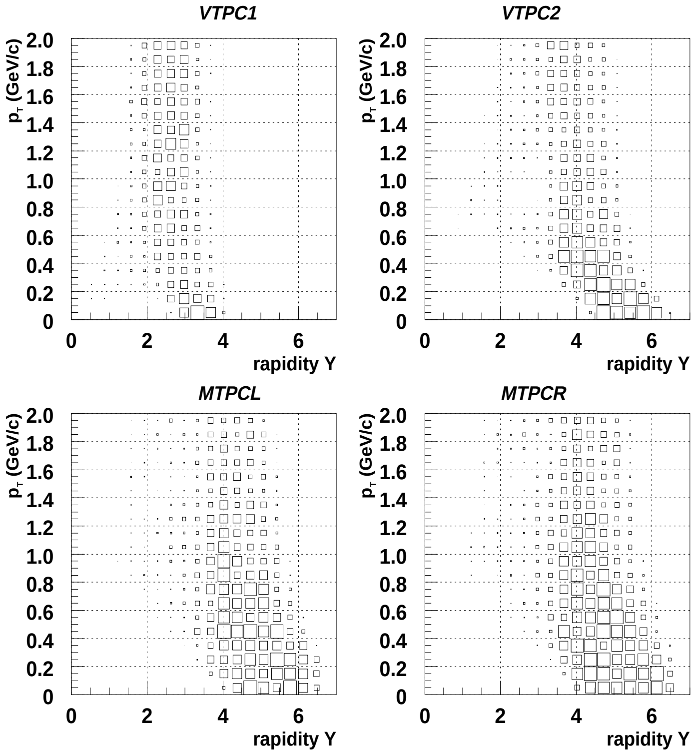

Figure 6.2: The acceptance for charged pions in the standard field configuration (1.5/1.1 T). There is a large overlap between VTPC2 and the MTPCs with the MTPCs reaching a bit higher. VTPC1 covers backward rapidity region exclusively.

reconstruction. The efficiency ϵ, is the defined as:

$$\epsilon = \frac{\#\,\text{of Embedded Tracks Reconstructed}}{\text{Total}\,\#\,\text{of Tracks Embedded}} \tag{6.2}$$

With figure 6.3 as a guide, three rapidity intervals were chosen in which correlation functions were to be constructed: $2<\mathrm{y}_{lab}<3$, $3<\mathrm{y}_{lab}<4$, and $4<\mathrm{y}_{lab}<5$. The first ($2<\mathrm{y}_{lab}<3$) is fully contained in VTPC1, while the last ($4<\mathrm{y}_{lab}<5$) is covered by VTPC2. The intermediate region ($3<\mathrm{y}_{lab}<4$) has acceptance for low p_T tracks (i.e. generally low K_T pairs) in VTPC1 and for high p_T tracks (i.e. high K_T pairs) in VTPC2. This provides a useful check on systematics between two different detectors.

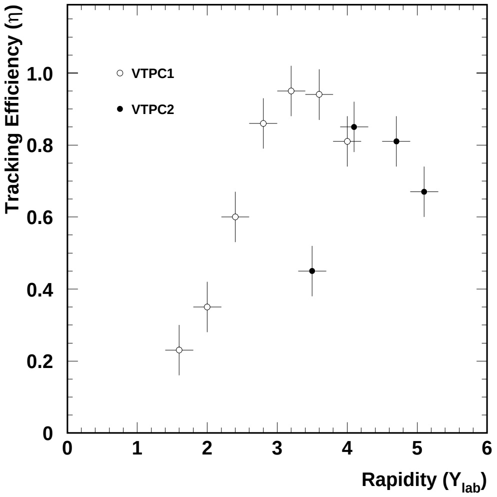

Figure 6.3: The estimated tracking efficiency for TRANS in VTPC1 and VTPC2 for the standard magnetic field setting of 1.5/1.1 T.

A cut is also made to reduce the number of particles that do not originate from the primary interaction in the target. Such "non-vertex" tracks are products of decays and conversions and because they are not produced in the initial fireball, they carry no information regarding the initial source and will only dilute the correlation strength. Shown in figure 6.4 is the reconstructed position of the track in the x-y plane at the target position (z=–580.1 cm). The arrows bound a region which, for this analysis, are considered to be tracks originating from the initial interaction (i.e. vertex tracks). Tracks which fall outside this region are disregarded. This cut corresponds to $\pm 2\sigma$ about the mean value. Note that the coordinate in the bending plane (i.e. x) has a substantially wider distribution than in the vertical plane (i.e. y). The long tails are a result of non-vertex tracks, the finite size of the beam spot (∼3 mm), and the fact that the beam moves in the x-y plane at the millimeter level over the course of a run. It should be mentioned that the decay products for particles with a small decay energy or Q value do not deviate from the original trajectory by a large amount (i.e. for Λ; Q=37.8 MeV), but this has the non-negligible effect of broadening the vertex position distribution. Thus, even though this cut is designed to remove secondary and tertiary decay products, there is a certain inefficiency in this respect which will tend to reduce the correlation strength. Nonetheless, the cuts made in previous HBT analyses were: $x_{mean}\pm$ 5 cm and $y_{mean}\pm$ 2 cm. The harder cuts used here are a result of the increased vertex resolution due to optimization of the detector operating parameters and better distortion corrections which were available for the 1995 data.

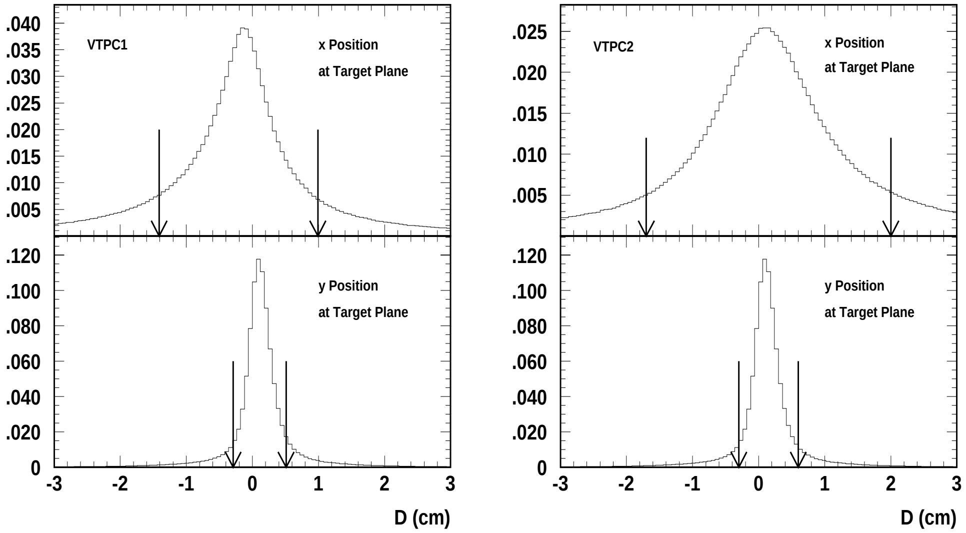

Figure 6.4: Position of the x and y coordinates at the target plane (z=-580.1 cm) as reported by VTPC1 (left) and VTPC2 (right). Arrows indicate the position of the cuts.

A cut on the track length is also important. This is done in an attempt to reduce the population of split tracks. A split track is produced when the tracking routine leaves a single track in one or more segments. This is a serious effect for HBT analysis as two segments of the same track will be very close in momentum space and will lead to an over estimation of the correlation strength at small relative momentum. In order to minimize this effect, a cut on the minimum number of points on a track is employed. Because TRANS uses templates, it is inherently less susceptible to producing such “ghost-tracks” than a conventional track follower.

The length cut is made at 20 points, and while this has a large effect in VTPC1, it is minimal in VTPC2. It was considered to base this cut on the percentage of measured points compared to the maximum number of possible points. However, it was found that this does not discriminate against short tracks. In fact it is the long tracks that seem to miss the largest proportion of points. This is illustrated in figure 6.5. It should also be noted that this cut is related to the Two-Track Resolution (TTR) cut made at the particle pair level which is described below.

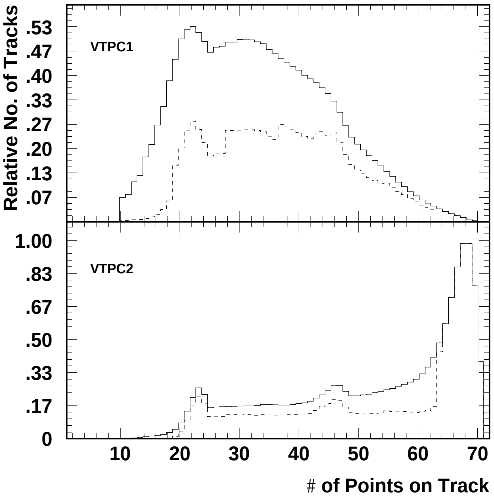

Figure 6.5: The number of points on all tracks in both TPCs (solid), and the number of tracks that would pass a cut where it is required that 90% or more of the total possible number of points lie on the track. The effect in VTPC2 is more drastic as it appears longer tracks are reduced with this cut. The requirement for a track in both TPCs is at least 20 points.

Finally, for identified particles, there is a cut on the specific ionization of the track. Ideally, given a parameterization of the mean $\frac{dE}{dx}$ versus momentum (i.e. equation 5.17), a cut could be made on this value with the window defined by the resolution of the measurement. However, this requires the functional form of the specific energy loss to be known to a high precision. While this seems to be the case for the Saleve side of VTPC2 (see figure 5.27), it is not the case on the Jura side, nor for VTPC1, and this introduces complications in the procedure. In order to cope with this, the most probable $\frac{dE}{dx}$ is plotted for all tracks within a 1 GeV/c momentum bin. The best (multi-)Gaussian fit is then made to the curve and an upper and lower window is made which defines the values of the ionization that will be accepted. The windows are set at a level where the ratio of the desired particle species (i.e. protons or pions) is at a level of 2-3 times that of the contaminant. This is shown in figure 6.6 Although this procedure is effective and very flexible, it is extremely labour intensive as these windows have to be checked on a run by run basis and for each side of each TPC. A good indication on the stability of these cuts is the number of particles accepted per event after the ionization cut is made. It is found that the average multiplicity per event is stable within several per mil over a span of ten runs when the cuts are optimized.

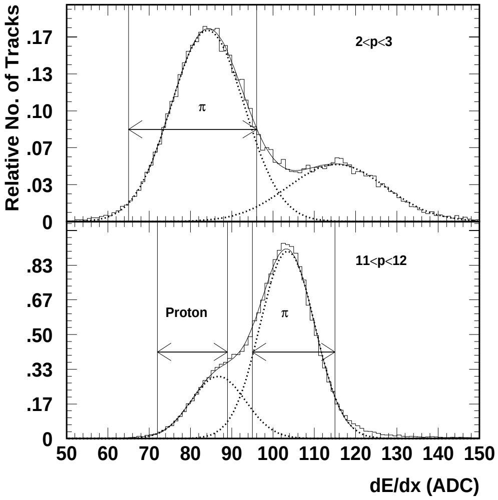

Figure 6.6: The windows for $\frac{dE}{dx}$ cuts which define PID in two momentum bins.

6.1.1.3 Particle Pair Level

It has been thought that the single most important criteria for an experiment that investigates HBT interferometry is its ultimate TTR. The logic behind this is that if two particles are close in configuration space, they will also be close in momentum space, and thus will strongly correlate. NA49 was designed with the aim of attaining a TTR of 10 mm, utilizing the $\frac{dE}{dx}$ information within the chambers, but this is not yet implemented. Shown in figure 6.7 is the relative tracking efficiency as a function of the separation distance between a particle pair. The separation distance is calculated as follows. Three equally spaced reference planes are selected in the TPC; the first pad row, the middle of the chamber, and the last pad row. The distance between the tracks is then calculated at these planes. If the tracks do not physically cross these planes, they are linearly extrapolated. The average of these three values is what defines the two-track separation. The tracking efficiency η, is calculated as the ratio between the number of tracks with a separation distance, D found in a single event compared with that of pairs from mixed events with the same separation distance.

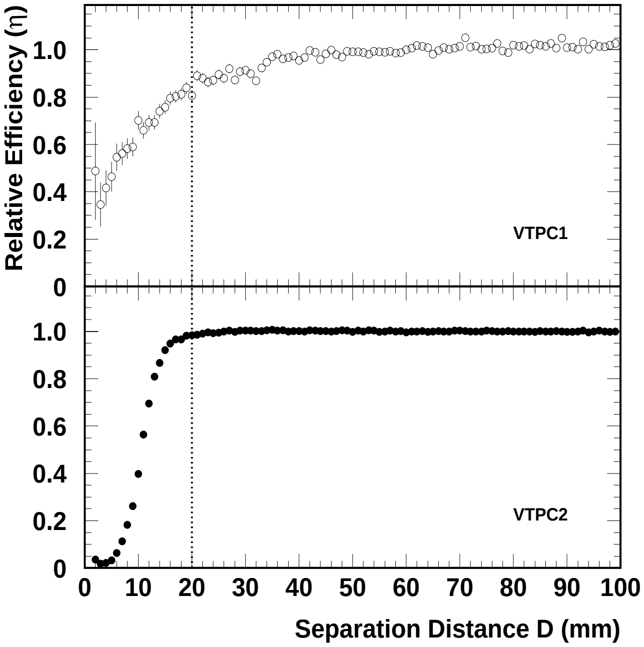

Figure 6.7: The relative tracking efficiency for VTPC1 (top) and VTPC2 (bottom) as a function of track separation distance D, as described in the text.

The effect of this cut on the data is interesting. Shown in figure 6.8 is the correlation between Q_{inv} of a particle pair and their separation distance D for 1000 events. Also indicated is the nominal cut at 20 mm, as well as a cut at a minimum

Q_{inv} of 5 MeV/c which is explained below. It is interesting to note that very few tracks are affected with this cut. In fact, a correlation function was constructed excluding pairs with a two-track separation of less than *5 cm*, and the extracted radii parameters did not deviate by more than the uncertainty in the fit parameters.

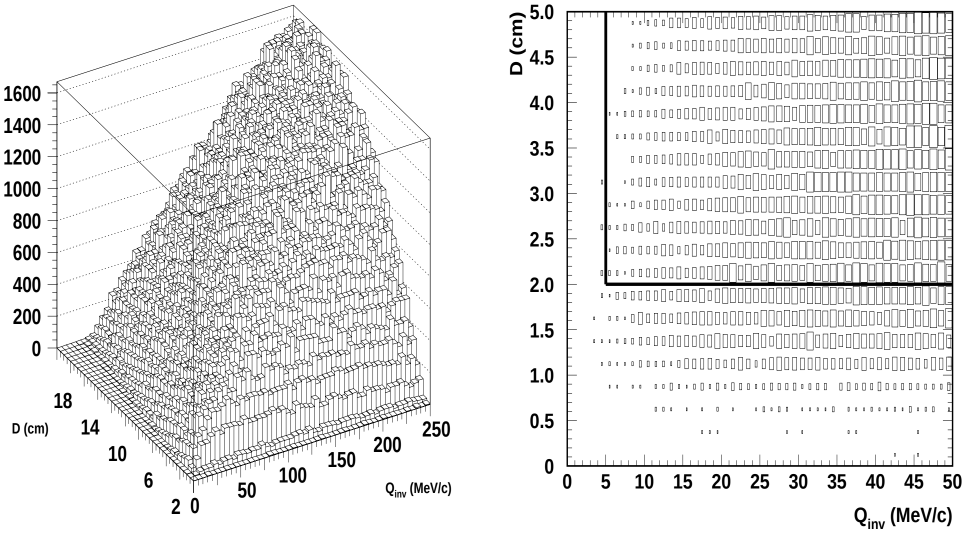

Figure 6.8: Relations between Q_{inv} and the two track separation distance D. Shown at right are the cuts at the particle pair level; pairs with <5 MeV/c difference in Q_{inv} and a two track separation distance of <2 cm are disregarded.

The last cut that is made is on the minimum Q_{inv} that a pair may have. This is a cut that can be traced to NA35 [57] and is designed as a "clean-up" to remove conversion electrons that are not rejected with a vertex cut (or $\frac{dE}{dx}$), as well as split tracks. This cut is 5 MeV/c for VTPC2 and 15 MeV/c for VTPC1 on account of the (slightly) poorer momentum resolution. It has a rather small effect on the data because the multiple scattering effects within the target are at the 7-8 MeV/c level and as such, this cut is below the absolute momentum resolution of the detectors. This consideration is also important for determining the bin size of 10 MeV/c. Although a smaller bin would be more sensitive in revealing detail of the shape of the correlation function, which is an issue of some importance with the integral method described in section 6.2, it is below resolving power of the spectrometer.

Once the particles are selected according to the above criteria, the correlation function is constructed. The data presented will be in the Longitudinally Co-Moving System (LCMS) as described in equation 3.20 of chapter 3. This is a reference frame in which the longitudinal momentum of each particle pair vanishes. This determines the decomposition of the momentum difference of the particle pairs. The correlation signal, or the numerator of equation 6.1 is deduced within a single event from all possible pairs that survive the cuts outlined above and assigning them to the appropriate momentum bin. A correlation is defined as an enhancement in yield over that expected from purely kinematical considerations, so the signal must be normalized against a "non-correlating" background. The uncorrelated background has several requirements: It should contain the residual correlations present in the event due to energy and momentum conservation but neither Bose-Einstein correlations nor "quasi-correlations" from resonance contributions. The way the background is constructed is through event mixing. That is, the denominator is determined in a similar manner to the signal but the pairs are constructed from particles in different events. Although event mixing does not incorporate energy-momentum correlations, this should not be a serious concern with the large multiplicities in heavy-ion collisions. That is, there is so much missing energy (i.e. neutral particles) that the kinematics of the complete event can not be determined and thus momentum conservation can be absorbed by the unobserved particles. Obviously, different events do not contain any Bose-Einstein correlations, nor do they contain contributions from resonances. It should be remarked that it is not possible to discriminate against pions that are produced from the decay of "long lived" resonances (i.e. ρ, ω, etc.) by any method, and these will dilute the correlation strength, but this is in the construction of any $\pi\pi$ correlation function. It has been suggested that the shape of the correlation function is strongly affected by the non-correlating resonance contributions, and this led to the current attempt of quantifying the shape information of the correlation function [67].

Although the above discussion outlines a suitable framework in which to construct a correlation function, effects due to the Coulomb interaction must be taken into account, before any useful information can be extracted.

6.1.2 Coulomb Effects

Since the correlation functions that will be presented involve charged particles, it is necessary to correct for the correlation introduced by the Coulomb interaction. Up until recently, most correlation functions were corrected by weighting each pair with a factor derived from the inverse Gamov factor. The Gamov factor is the square of the relative Coulomb wave-function of a particle pair at zero separation in configuration space. It has the form:

$$G(\eta) = \frac{\eta}{e^{\eta} - 1} \tag{6.3}$$

with:

$$\eta = \frac{2\pi m_{\pi}}{Q_{inv}} \tag{6.4}$$

where m_{π} is the pion mass (or whatever particle is under investigation), and Q_{inv} is the invariant 4-momentum difference of a pair. While the assumptions of a non-relativistic and point-like source made in the formulation of this factor are perhaps appropriate for the sources investigated in $\mathrm{e}^{+}\mathrm{e}^{-}$ or pp collisions, they are certainly not valid for the sources created in the current relativistic heavy ion experiments at BNL and CERN. In fact it has been shown that the use of an inappropriate Gamov correction results in an underestimation of the source size [147]. This is the reason for the apparent saturation size of 4 fm observed in the first round of relativistic heavy ion collisions that was mentioned in chapter 3.

Although some experiments still utilize the Gamov correction, [148], the majority rely on some other means of calculating or parameterizing the effect of the Coulomb interaction. This has left a void in the community as there no longer exists a standard Coulomb correction. This complicates comparisons between experiments, because each correction introduces slightly different systematic effects. There is presently a flurry of theoretical activity in terms of understanding the effects of various Coulomb corrections [149].

One of the more popular "post-Gamov" corrections is that of Pratt [150]. It involves the calculation of two body Coulomb wave-functions and assigns weights to pairs based on their relative momentum difference Q_{inv}.[2] There are two main concerns with this approach. First there is no account of multi-body Coulomb effects, and second, no allowance for source dependent effects is made. These are not really oversights of the model. It is simply intractable to carry out a many body Coulomb calculation. It is equally difficult to evaluate source dependent effects. If one had enough information about the source to carry out such a calculation (essentially the emission function), there would be no need to make the measurement. The non-existence of suitable calculational tools to adequately address these questions speaks to the need to find some sort of phenomenological or effective correction.

NA35 was the first experiment to extract the effects of the Coulomb interaction from *measured* particle spectra [152]. This involved the measurement of the correlation between "+−" pairs (i.e. C^{+-}). Because opposite sign pions do not exhibit a Bose-Einstein correlation, any signal obtained in C^{+-} may be interpreted as due to the Coulomb effect. Thus if it is postulated:

$$C^{+-} \sim -C^{--}_{Coul} \tag{6.5}$$

an effective Coulomb correction can be used in lieu of model dependent calculations. The reason this was possible is that NA35 was a large acceptance spectrometer and had the ability to measure the positive and negative particle spectra *simultaneously.* NA49, like NA35, is in a unique position to make a similar measurement. It should

---

[2] Coulomb corrections are dominantly parameterized in terms of Q_{inv}. Schönfelder attempted to base the correction on Q_{Tout}, Q_{Tside}, and Q_{Long} components with little difference in results from that of the procedure described here [151].

be remarked that at the present time, NA49 is the only heavy ion experiment able to deduce a correction in this manner. The virtues and problems with this method are detailed below.

6.1.3 Effective Coulomb Interaction

The most serious criticism of this method revolves around the asymmetry in the interaction time between like and unlike sign particles. Oppositely charged particles attract, and so will be closer for a longer period of time. Therefore, the maximum strength of the interaction is felt for a longer time in this channel than in the case of like sign particles under the same conditions. Thus the *effect* of the Coulomb interaction is not completely identical in the different channels, and this may introduce an asymmetry. If the particles are highly relativistic, this should be a small effect. However, it should become much more important with heavier particles. With regards to this question, studies of the correlation functions for kaons and protons identified by the TOF walls are now underway.

Any further asymmetry in the two channels must have its origin in the strong interaction. This basically reduces to a question of the validity of charge symmetry, and it is known that it holds to the several per cent level in nuclear physics and is broken by the presence of the Coulomb interaction.[3] In fact, even the much stronger assumption of charge independence is not a bad one. Another asymmetry may occur due to the net isospin carried in the Pb-Pb system. Pion-nucleon scattering can be described by two basic interactions—the isoscaler (i.e. π^-p and π^+n) and the isovector (i.e. π^-n and π^+p). Although the amplitudes in the different channels are identical, the number of possible interactions (i.e. rescatterings) that occur in a Pb-Pb system is not the same, and this may generate an asymmetry. If this difference is large it should be visible in the difference between the radii reported by π^+-π^+ and π^--π^- pairs.

---

[3] Actually a more fundamental reason is due to the mass difference of the u and d quarks.

With these considerations, the NA49 Coulomb correction is based on the correlation function of the "+−" pair spectrum in the variable Q_{inv}, subject to the same cuts used in the construction of a conventional correlation function. The Coulomb correction is then parameterized in an analytic form such that weights for each pair in terms of their Q_{inv} can be assigned. Phenomenologically the correction is in the spirit of the Yukawa potential which is essentially an exponentially damped Coulomb potential. The deviation from the r^{-2} form is the origin of finite range of the potential. Likewise the NA49 phenomenological Coulomb correction is taken as an exponentially damped Gamov factor, given by:

$$(G(\eta) - 1)e^{-Q_{inv}/Q_{eff}} + 1 \tag{6.6}$$

where G(η) is the Gamov factor as defined in equation 6.3, and Q_{eff} is a parameter that is fit to the data. The exponential damping modifies the Q^{-2} dependence which is characteristic of a point source. The damping parameterizes the multi-body Coulomb interactions and source dependent effects, into an effective correction. In the limit that $Q_{eff} \rightarrow \infty$, the correction approaches the Gamov factor—a point source, while in the opposite limit as it approaches zero, the function goes to 1—an infinite source. Thus Q_{eff} has some physical relation to the source. Although this correction parameterizes a myriad of effects, they are all real, and most importantly, experimental observables. This is perhaps the biggest argument in favor of this type of correction because model calculations of the Coulomb interaction will undoubtedly change. However, the NA49 correlation functions are simply particle ratios weighted by the correlation seen in "+−" pairs, and this is independent of any model assumption! It must be remarked that comparisons between the Pratt code and the C^{+-} method are quite compatible [154].

Figure 6.9 shows the results for C^{+-} with comparison to the Gamov factor in different rapidity intervals for 5k events. A rapidity dependence on the magnitude of the correction is observed which is not unexpected. The source that is created in a Pb-Pb collision has a net charge of ~164 e. Since the central region has the highest particle density (see the $\frac{dN}{dy}$ distribution in [62]), if the fireball does play a role in modifying the momentum spectra of particles via the Coulomb effect, it would be expected that these effects be strongest in the central region. It is interesting to note that this is not accounted for in any calculational model.

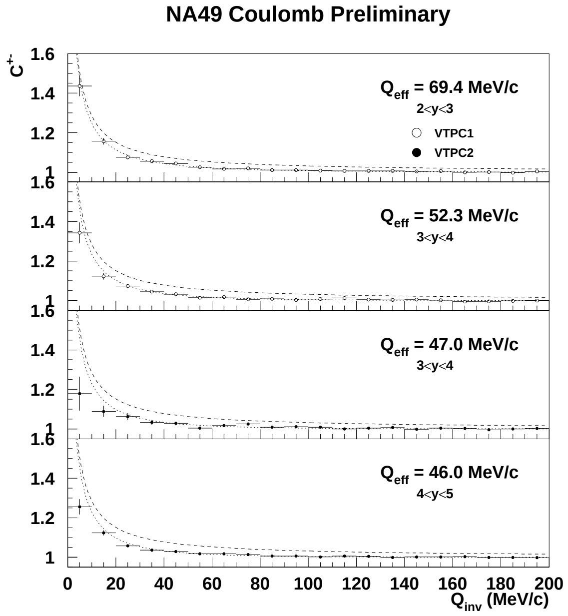

Figure 6.9: Coulomb correlation deduced from 5k events with no PID. The data is fit to the single parameter function as given in equation 6.6 and shown with the dotted line. For comparison purposes the Gamov correction is shown with a dashed line. Although the modified Gamov factor is a better fit, it still does not describe the data very well at small Q_{inv}.

Although intriguing, figure 6.9 shows the weakness of low statistics and a single parameter fit. Specifically the fit is very poor in the low Q^2_{inv} region, and this will skew the correlation function at small relative momentum. Although this may be satisfactory for extracting parameters from a fitting procedure (which will be discussed in section 6.2), any shape information contained in the correlation function is lost. It is possible to obtain a better fit by introducing a second parameter in the fit. The form of equation 6.6 is retained but the pole in the parameter η can be shifted from Q_{inv}=0 to a finite value; that is:

$$\eta \rightarrow \eta^{'} = \frac{2\pi m_{\pi}}{(Q_{inv} - Q_{o})} \tag{6.7}$$

where Q_o is an additional free parameter fit to the data. The introduction of a second parameter allows a better fit to the data in the high rapidity region as shown in figure 6.10. A decrease in the χ^2 of the fit up to a factor of 3 is observed. This changes the form of the rapidity dependence of Q_{eff} quite appreciably from a monotonically decreasing function with increasing rapidity to one that is more symmetric about mid-rapidity. This is an indication that the source does play a role in modifying the momentum spectra of particles via the Coulomb interaction. Since VTPC1 has acceptance in this region for low K_T pairs and VTPC2 for high K_T pairs, the difference between VTPC1 and VTPC2 in the rapidity region 3<y_{lab} <4 is an indication of a K_T dependence This is not unexpected as high K_T pairs should be less affected by the Coulomb interaction than those with smaller momentum.

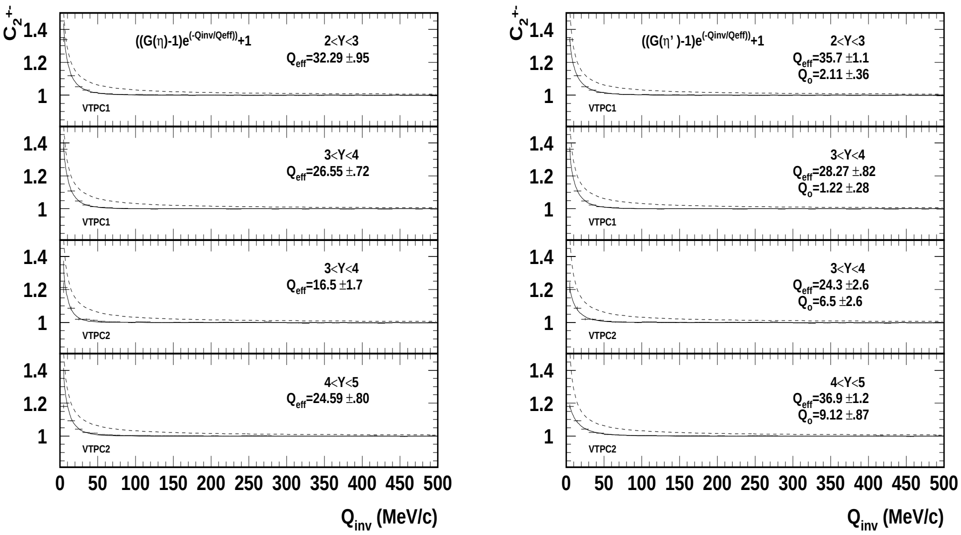

Figure 6.10: The Coulomb correlation function C^{+-} deduced from 40k events (i.e. $\sim 10^8$ pairs. Shown are results for the single parameter (left) and the two parameter fits (right) as described in the text. The fits in the single parameter fit seem to get worse in the high rapidity regions.

The main difference in the two functions is that the slope at small relative momentum is much softer. This has the effect of minimally disturbing the shape of the correlation function. This is discussed in detail in section 6.2. It should be remarked that the functional form of the correction is not of overwhelming importance. Although it is obviously desirable to attach a physical significance to the parameters (i.e. Q_{eff}), in this case the most important criterion of the function is that it describe the shape of the measured "C^{+-}" correlation function in the best possible manner.

Although there are small subtleties observed between the different corrections, the main question is what effect does this have on the observables—namely the correlation functions. In order to answer this, one-dimensional projections of correlation functions will be presented in the rapidity interval from $4 < y_{lab} < 5$ with different Coulomb corrections. The reason this region is chosen is that it is well documented and comparisons can be made with a wide variety of experiments. One dimensional projections are shown because they visually convey shape information most easily. Shown in figure 6.11 are correlation functions as a function of the variable Q_{inv} for two different Coulomb corrections along with the best Gaussian fits and results from the new integral method which is described in section 6.2. The most striking feature of the plots is that correlation function with no Coulomb correction has a profile that is described extremely well by a Gaussian. This will be quantified in section 6.2. It also appears that the modified one-parameter Coulomb correction distorts the shape of the correlation function a great deal. It should be remarked that because the Gamov factor imposes an even larger weight to pairs at small relative momentum, it will introduce a much larger distortion. The two parameter Coulomb correction has the desired effect of increasing the weight of low Q pairs, but without the pathological behavior of destroying the shape of the correlation function.

Although the introduction of a second fit parameter in the Coulomb correction of equation 6.6 does not allow the direct comparison of the Q_{eff} parameters, it is perhaps enlightening to compare the slopes of the correction factors at various

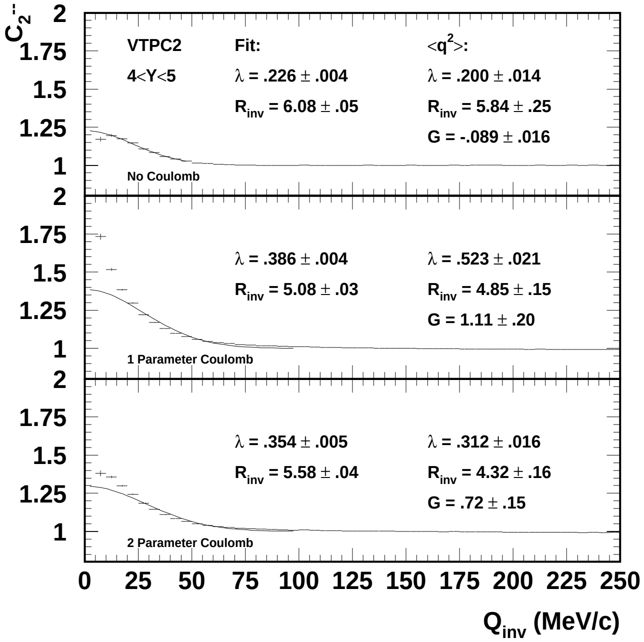

Figure 6.11: Correlation functions in the rapidity region 4<y<5 with no (top) Coulomb correlation, the one parameter (middle) Coulomb correction, and the two parameter (bottom) Coulomb correction. Also shown are results utilizing a conventional χ^2 minimization and the integral method. The parameter G describes the deviation from Gaussian behavior where a perfect Gaussian would have G=0. This is described in the text.

values of Q_{inv}. This is shown in figure 6.12 for the rapidity intervals of interest in this thesis. It must be remembered that a cut on the minimum Q_{inv} of 5 MeV/c (15 MeV/c) is made in VTPC2 (VTPC1). The introduction of the second parameter is shown to soften the slope significantly. This appears to reduce the distortions in the correlation function.

It should be remarked that the above Coulomb correlation functions were constructed with h^+h^- pairs. This means that protons (and anti-protons) also contribute. It is expected that using identified spectra will have a significant effect on the λ parameter of the $C^{\pm\pm}$ correlation functions, so it is reasonable to expect that identified spectra will alter the Coulomb correlation function (i.e. C^{+-}) as well. In fact, constructing the correlation function by selecting only pions does produce a measurable effect, which is illustrated in figure 6.13. The slight shift in the param-

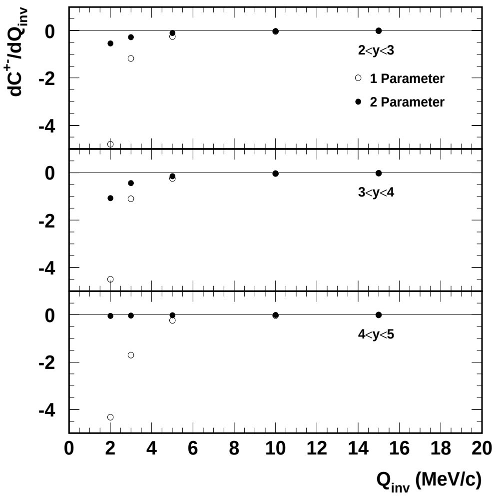

Figure 6.12: Slopes of the one and two parameter Coulomb corrections. The singularity at Q_{inv}=0 is evident in the decreasing value of the slope for the single parameter function while it is absent when the two parameter function is utilized. The small variation in slope results in a significantly reduced distortion in the correlation function, as well as reduced radii parameters.

eters indicates that the measured h^+h^- interaction is different from that of $\pi^+\pi^-$. This is illustrated in figure 6.14. The Coulomb behavior of the identified spectra shows a symmetry about mid-rapidity. It is interesting to note there is a significant effect on the parameters in all regions of phase space with the use of identified spectra.

From the above considerations, two separate Coulomb correlation function will be constructed in each of the three rapidity intervals; one using PID and one without. Any K_T dependence will be neglected. The two parameter modified Coulomb correction will be used in order to parameterize this function and assign weights to each particle pair in the signal, as opposed to those in the background [147]. Following equation 6.5, the same correction will be used for the $\pi^+\pi^+$ pairs as for $\pi^-\pi^-$.

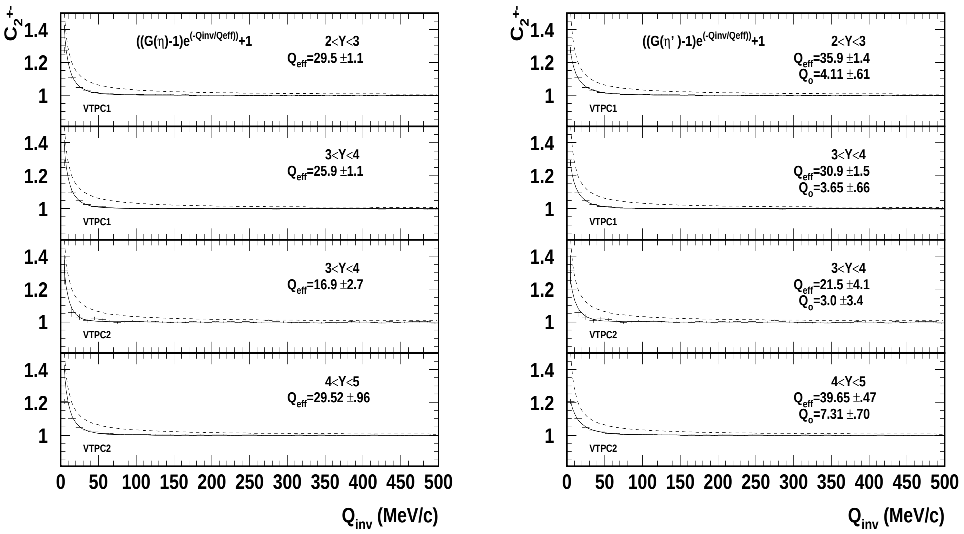

Figure 6.13: Same as figure 6.10, but with identified pions—$C^{\pi^+\pi^+}$. The reduction in the number of protons (anti-protons) and electrons (positrons) in the sample give parameters that are very similar but show a slightly better reflection symmetry about mid-rapidity, especially when compared with the non-identified spectra of figure 6.9.

6.2 Extraction of Radii Parameters

Two different procedures for extracting the width of a correlation function will be compared. Until this point in time, all experiments have exclusively used the conventional method of fitting the correlation function to presupposed shape—usually a Gaussian. Recently there have been some concerns that a Gaussian does not adequately describe the shape of the correlation function, and in fact, an exponential is found to be a much better fit in Q_{inv}. Referring to figure 6.11, it can be seen that this may be an artifact of the Coulomb correction, if one is not careful. It has been suggested that long-lived resonances contribute to the distortion of the shape of the correlation function [67]. This led to the proposal of extracting the width of the correlation function by calculating its second order moment numerically instead of relying on a fit algorithm. This has the added advantage that the shape of the function, or rather the deviation from Gaussian behavior may be quantified

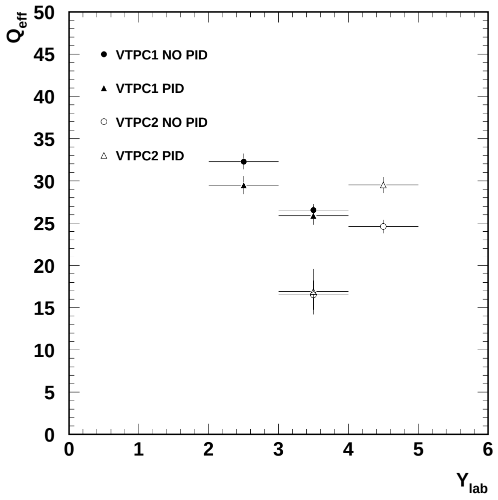

Figure 6.14: Coulomb correction factor Q_{eff} from the single parameter fits as a function of rapidity. A significant shift in the parameters is produced with the implementation of a $\frac{dE}{dx}$ cut.

in a systematic manner through its fourth order moment or kurtosis, as defined in equation 3.22. The problem with this method is that it is statistically hungry and very sensitive to the errors of each bin. For our purposes, the n^{th} order moments are calculated via a numerical integration routine. The uncertainty in the results become quite large if the statistical error on each bin is not small. Because of the large statistical samples available to NA49 in ensembles, this is not a limitation to moments in a single dimension. However, this begins to become a concern in multi-dimensional analysis. This is an important point to keep in mind when considering event-by-event correlation functions because the statistical uncertainty is quite a bit larger than in ensemble functions. This will become evident in section 6.6.

Shown in the following figures 6.15–6.17 are the radii parameters for h^-h^- one-dimensional projections of multi-dimensional correlation functions produced with the two parameter Coulomb correction. In each figure, the best Gaussian curve that can be fit to the data is shown as well as the parameters extracted from both the conventional Gaussian fit (Fit:) and the new integral method ($<q^2>$:) as described in chapter 3. By conventional fit it is meant a χ^2 minimization is utilized.

The integral is calculated bin-by-bin with increasing Q starting at Q=0. A bin will contribute to the integral if the error is not larger than its contribution to the 0^{th} order moment (i.e. $[C(q) - 1] > \delta C(q)$). When this condition is satisfied (at the "cross-over" point), the calculation stops and the value of the radius is calculated. The arrows in the plots indicate the cross-over point. From these figures it appears that the values deduced from the two methods do not have the same interpretation as the radius parameters. Those that are extracted from the Gaussian fitting procedure are systematically 10-20% larger than those from the integral method. Note that the errors are an order of magnitude smaller as well. The decrease in the radius parameters can be understood in terms of what part of the correlation function each method is sensitive too. The fit is sensitive to a very localized region; the first 8-12 bins (in our case) and especially in the area immediately around the inflection point of the function (i.e. Q∼65 MeV/c). This is why narrow correlation functions are so sensitive to the Coulomb correction because

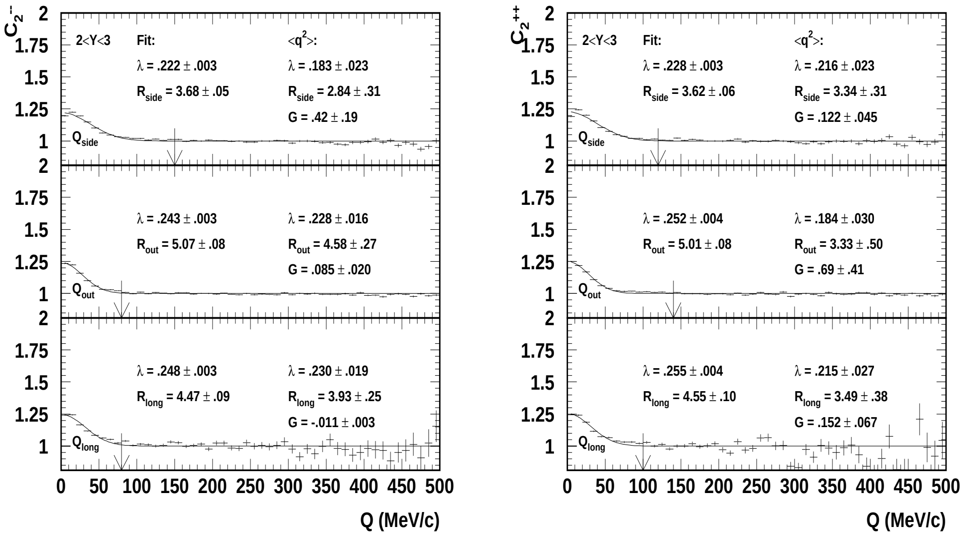

Figure 6.15: One-dimensional projections of the 3-d correlation functions and the extracted radii parameters from the fit and integral methods. Shown are results from 2<y<3 region for unidentified negative (left) and positive (right) pairs. The curve is the Gaussian function that is fit to the data.

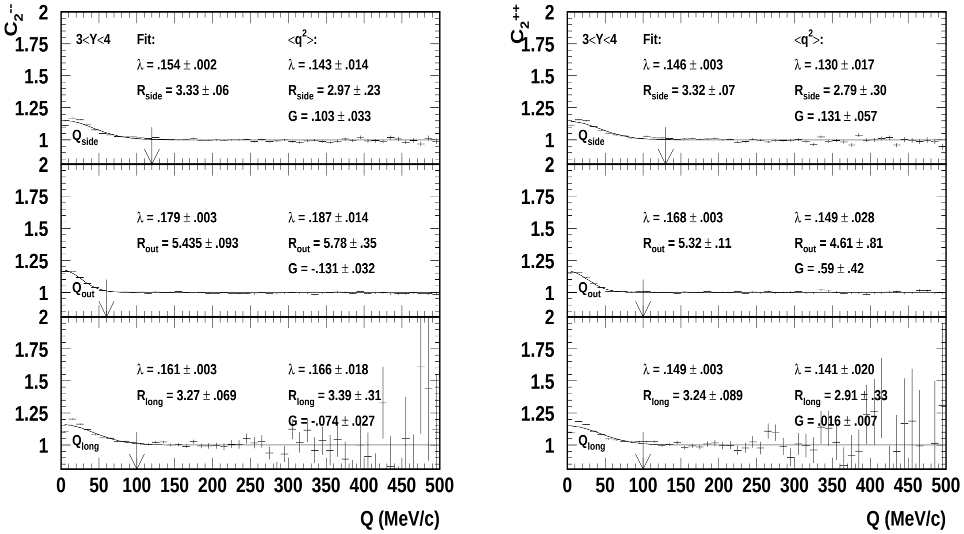

Figure 6.16: Same as figure 6.15 but the rapidity region from 3<y<4 in VTPC1.

this is the region where the correction factors begin to diverge. Because the Gaussian fitting procedure is sensitive to a small region of the correlation function, the radii deduced from this method are relatively independent of whether the first 10, 20, 30, or 40 bins are used. Furthermore, there is very little sensitivity to the very small Q bins (i.e. Q_{inv} <15 MeV/c), because the errors are usually an order of magnitude larger than the points at larger relative momentum. As such, whether these points are or are not included in the fit is rather academic. This has generally been regarded as a good thing because although the correlation strength is maximal in this region, it also carries the largest uncertainty. This is a result of the experimental difficulties in measuring closely separated tracks—either in momentum or configuration space. In a large acceptance experiment like NA49, one has to be careful with split tracks that can mimic low Q_{inv} pairs and overestimate the yield in this region. Conversely a small acceptance experiment is hurt by the fact that they need to generate a large event sample to be statistically competitive. In order to do this, a thick target is usually employed to increase the trigger rate, but it also degrades the momentum

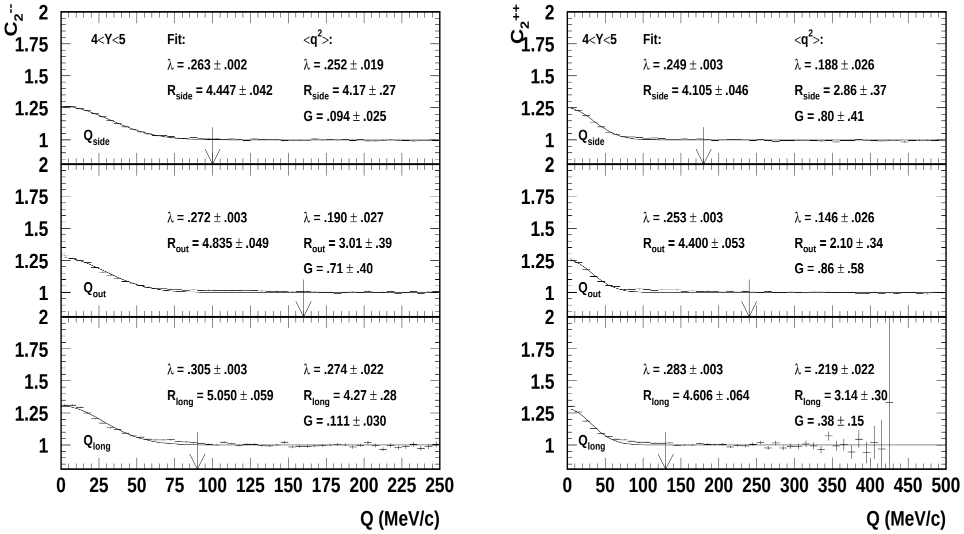

Figure 6.17: Same as figure 6.15 but the rapidity region from 4<y<5 in VTPC2.

resolution and distorts this region of the spectrum. For example NA44 used a Pb target of 4% interaction length which is ∼2.7-3.4 g cm^{-2} [155]. NA49 on the other hand utilizes a 224 mg cm^{-2} target. As such NA49 expects a 7-9 MeV/c uncertainty in momentum of a single particle due to multiple scattering effects in the spectrometer of which 95% is due to interactions within the target. NA44 on the other hand expects an uncertainty of nearly 15 MeV/c due to multiple scattering in the target alone. On the other hand, NA44 does not have to be concerned with split tracks in their detector which are a serious concern in the TPCs of NA49. In either case, it can be seen that this region is a cause of rather large uncertainty! It is somewhat ironic that the region where the correlation is strongest is weighted the least in the extraction of radii parameters.

Although the Gaussian fit method is only sensitive to the localized “bump”, the integral method is sensitive to a more extended region both at small and large relative momentum (Q). Small momentum bins make a large contribution because the correlation function has its largest values in this region. Large relative momentum bins also make a sizable contribution to the integral of equation 3.21 because, even though the value of the correlation function is small, it is weighted with Q_i^2 of the bin. So, in a sense, the integral method is more democratic because it uses a wider range of the correlation function, but it also demands that the errors be small and well understood; otherwise the uncertainty becomes unmanageable. The minimum Q_{inv} cut that is made in the data poses a bit of a problem, but is solved by a linear extrapolation of the correlation function to the lowest Q bin. This procedure is not entirely satisfactory and is a major cause of systematic uncertainty in this method! Using the criterion of the error on the bin being smaller than its contribution to the 0^{th} order moment implies that large Q bins will be used when statistical error is small. With an increasing number of large Q bins the value of the 2^{nd} order moment will increase. Since the value of $<q^2>$ is inversely proportional to the radius parameter, the radius will appear smaller, as observed. A subtle effect that leads to larger discrepancies between the fit and integral methods is the fact that the Coulomb correction introduces a slope in the correlation function. This is seen in figure 6.18 and it is not an effect of physics, but rather solely due to the shape of the Coulomb correction. It is most serious with the Gamov factor and although it appears to be substantially reduced with the new 2 parameter modified Coulomb correction, it is still evident in the correlation function. This is a relatively minor annoyance if the radii parameters are extracted via a fitting procedure because of its limited sensitivity to the large Q bins. However, it is important in the case of the integral method because of the large weights in the higher moments at large relative momentum. This is truly non-Gaussian behavior and the integral method is sensitive to this. This effect is the main reason for imposing an arbitrary truncation of the integral at the “cross-over” point. While the imposition of this cut is a very artificial criterion, it highlights the point that as more sensitive methods are used to extract information from the correlation functions, small systematic effects that were previously ignored will have to be addressed. This is very important in light of some recent proposals looking into “Fourier ripples”, structure in the profile of the correlation function and real multi-particle (i.e. >2 particle) correlations [156].

It is noteworthy that in cases where the integral is cut off at a relatively small Q value, the agreement between the two methods is much better. This is shown in detail in the figures of Appendix E, where the Q_{inv} spectra with and without the two parameter Coulomb correction are shown along with the Transverse (Q_T) and Longitudinal (Q_T) one-dimensional projections of 3-d Pratt-Bertsch correlation functions. These figures demonstrate that the transverse direction is affected to a much larger extent by the slope introduced by the Coulomb correction than the Longitudinal direction, independent of rapidity region.

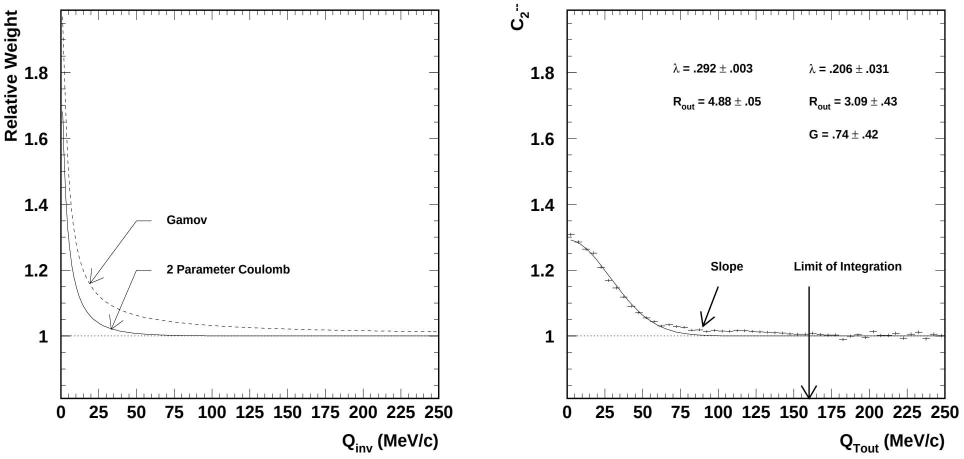

Figure 6.18: A slope introduced into the correlation function by the Coulomb correction leads to an artificial increase in the number of bins integrated. This slope is not a Gaussian feature and shows up in the rather large G parameter.

Although the width of the correlation function is quantifiable using $<q^n>$ moments, it poses a problem in terms of extracting a value for λ and again, a rather artificial solution is employed. A Gaussian ansatz, not unlike that made in the fitting procedure, is made. With this assumption and the values for the 0^{th} and 2^{nd} order q moments, its amplitude, or λ can be calculated as outlined in equation 3.23. Using this method, the λ parameter is the order of 10% smaller than the value extracted by the Gaussian fitting procedure. It makes little sense to talk of λ deduced from this method unless it is possible to quantify the extent that the function is Gaussian or its “Gaussisity”.[4] This is quantifiable in terms of equation 3.22 which defines the value of G. For a true Gaussian, G is zero while a non-zero value reflects non-Gaussian behavior. Referring again to figure 6.11, it is possible to say the correlation functions are closest to a Gaussian profile when no Coulomb correction is done. When a single parameter correction is used, a large distortion in the correlation function is seen. This is conveyed quantitatively in the value of G. While the two parameter Coulomb correction retains a much more Gaussian profile of the correlation function, the slope introduced by this correction is not negligible, and G is once again sensitive to this. What is clear in figures 6.15–6.17 is that there is a correlation between the differences in the radii parameters as given by the fit and integral methods and the G parameter. This is illustrated in figure 6.19. It should also be noted that the integral and fit radii values tend to agree when the fit is truncated at a value of Q<80 MeV/c, or the region which the fit method begins to loose sensitivity. This will be revisited in section 6.6. It is important to emphasize that one must be careful not to confuse the non-Gaussian behavior of the correlation function with the non-Gaussian behavior introduced by the Coulomb correction. This is especially critical in the interpretation of a correlation function in terms of Q_{inv} [157]. If the Coulomb correction is parameterized as a function of Q_{inv}, the correlation function in the same variable (i.e. Q_{inv}) will be maximally distorted.

6.3 Effect of PID

One of the largest uncertainties in the construction of correlation functions is the effect of contamination of “non-identical” particles. All correlation functions shown thus far have been based on $h^{\pm}h^{\pm}$ spectra and it is relatively unknown whether contamination due to “non-pion species” alter the radii parameters that are extracted. NA44 had the ability to measure identified particle correlations

---

[4] name suggested by U. Wiedemann.

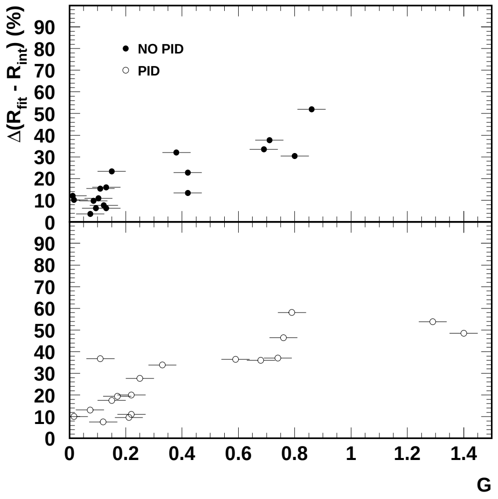

Figure 6.19: The "Gaussisity" parameter G increases with increasing difference in the radii parameters deduced from the fit and integral methods. The data is from the 1D projections over all rapidity intervals. PID will be discussed in section 6.3.

[155]. However, this detector covered only a small region of phase space. As such, the results had to be corrected for "residual correlations" that occurred in the supposedly uncorrelated background. No attempt at identified HBT spectra has ever been made over a large solid angle in heavy ion experiment before.

Comparison between h^-h^- and h^+h^+ correlations from figures 6.15–6.17 show differences up to 20% in the parameters extracted—most notably in the correlation strength (λ) being smaller in the positive channel. Although it may be argued that it is not an important consideration because of the ambiguity in this parameter, it is not immediately obvious that λ and R_i are independent.[5] In fact it will be demonstrated that this is not the case.

The main theme of chapter 5 was the PID capabilities of the VTPCs. Figure 6.6 indicates that electrons can be identified quite effectively. Since electrons are the main contaminant in the "$--$" channel, a particle sample with a signifi-

---

[5] In fact, it is the height of the correlation function (i.e. λ) in pp correlations that is proportional to the volume of the emitting source.

cantly enhanced purity should be possible with the use of PID. Furthermore, it is also feasible to attempt $\pi^+\pi^+$ correlations. These have previously been untouched because of the unknown effect of proton contamination. Preliminary work indicated that electrons have a rather large effect in HBT correlation functions if they are not removed [158]. Because of the large bending power of the magnets, electron contamination in VTPC2 is small because not many low momentum electrons produced in the target actually reach the chamber. The majority of electrons are produced by conversion downstream of the target, and a target vertex cut is able to reduce their number considerably. Furthermore, not many high momentum electrons exist. The problem is more acute in VTPC1 because there is a large number of electrons produced within the target and a vertex cut does not remove them. It has been shown that these particles have a large adverse effect on the parameters extracted from the correlation function [158]. The first attempt in reducing the electron contamination was made by imposing a large cut in the minimum Q_{inv} required (i.e. Q_{inv} >35 MeV/c). Contrary to expectations of reducing correlation strength (cutting 40% of the signal region) λ actually *increased.* Although a small cut is still employed in the current analysis (15 MeV/c in VTPC1 and 5 MeV/c in VTPC2) this is not a cut that anyone would advocate for reducing particle contaminants. It will certainly not work for protons. Results show that electron contamination is as high as 20% in low momentum region of interest in the TPCs (see figure 5.22). In order to test the capabilities of PID, a proton-proton correlation function was constructed. Particles were selected based solely on the ionization of the tracks as measured in VTPC2. The selection is based on the procedure outlined illustrated in figure 6.6. The rapidity region covered is from 3<y<5 and the results are shown in figure 6.20. No Coulomb correction is made. What is seen is typical behavior of such a function where the correlation function begins to turn positive at at Q_{inv} of about 40 MeV/c, reach a peak, and turns negative, approaching zero at Q_{inv}=0.[6] After the rather hard cuts were made, an average of ~15 tracks per event remained.

---

[6] For a comparison see [159].

Even with this small sample, there is evidence that multi-dimensional analysis can be done at NA49 on pp correlation functions. Although these functions are not usable from a physics points of view (yet!!), they demonstrate that PID based on $\frac{dE}{dx}$ is useful in terms of selecting particles for correlation functions. Furthermore when full use of all detector subsystems (i.e. VTPC/MTPC/TOF) is made, high statistic correlation functions with identified particles of high purity will be possible.

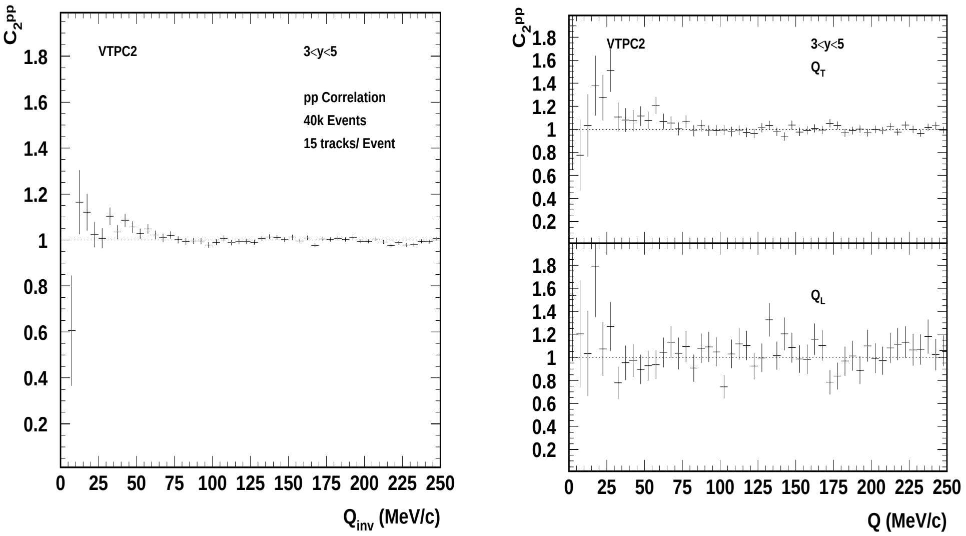

Figure 6.20: Proton correlation function constructed only from $\frac{dE}{dx}$ information in VTPC2. No Coulomb correction was done

6.3.1 Correlation Functions with PID

For completeness, the analog of figures 6.15–6.17 with identified particles are given in figures 6.21–6.23. It is interesting to note that both the λ parameter and the radii are systematically larger when PID is utilized. The increase is of the order of 5-10% but it should be remembered that the correlation strength (λ) is diluted when a multi-dimensional correlation function is projected into a single dimension. The projection was ±30 MeV/c. There is also an increase in the difference between the radii parameters extracted from the integral and the fit methods with the use of identified spectra. It appears that the reason for this is an increase in the number of bins integrated when PID is used. This can be attributed to a much smoother shape of the correlation function—again indirect evidence that the use of identified particle spectra does affect the correlation function in subtle ways.

It should be remarked that the cuts based on PID can not be made overly harsh. A correlation function was constructed with a cut of the mean $\frac{dE}{dx}$ of each momentum bin $\pm .25\sigma$ instead of the nominal $\sim 2\sigma$. By using such a strong cut it was believed that the probability of accepting any contaminants would be almost zero which would maximize λ. Instead, the λ parameter decreased by a factor of 2 and the uncertainty in the radii parameters increased. If the effect of such a harsh cut can be related to a severe decrease in tracking efficiency, it leads one to believe that the random loss of many tracks over a large region of phase space is reflected in the parameters extracted from the correlation function. This is an important point to keep in mind for correlation studies at large tracking based detectors. However, this has not been reproducible in simulation [160].

At this point, the discussion on 1-dimensional correlation functions will be terminated, as they provide a very limited view of the fireball. A single dimension in Q_{inv} is suitable if the source is static, as in the historical case of stellar interferometry. However, the emitting source produced in a relativistic heavy ion collision exists only for a brief instance during which time matter is severely heated and compressed, reaches a quasi-equilibrium state (maybe), expands, cools, and finally hadronizes. As such, it seems that the source is a highly dynamic system that can not be examined in sufficient detail by a single variable—thus we move to multi-dimensional correlation functions.

6.4 Multi-Dimensional Correlation Functions

Because the statistical power of current heavy ion experiments has become so large, it is possible to make highly differential measurements of a correlation func-

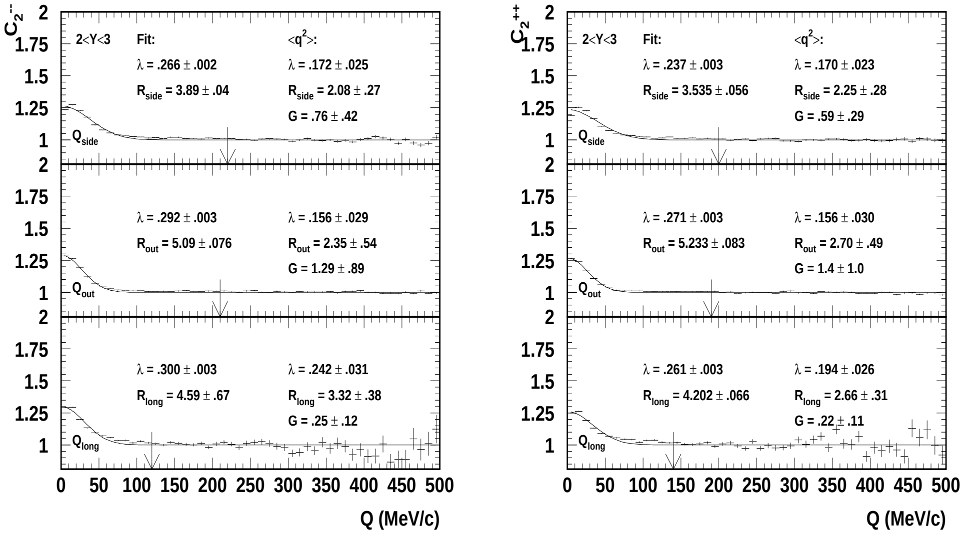

Figure 6.21: One-dimensional projections of the 3-d correlation functions and the extracted radii parameters from the fit and integral methods for identified particles. Shown are results from 2<y<3 region for negatives (left) and positives (right).

tion. That is, a decomposition of the relative momentum difference can be made in terms of the transverse and longitudinal directions. The evolution of the radii parameters with the pair's transverse momentum can also be studied. These measurements give insight into the different dimensions of the source as well as uncovering effects of ordered expansion [161]. By simultaneously fitting radii parameters in a multi-dimensional space, as outlined in equation 3.18, a much better characterization of the source can be obtained. Single dimension correlation functions are easily visualized and hence convenient for illustration. However, the bulk of information regarding the fireball comes from multi-dimensional analysis. The following section will attempt to illustrate the effect of PID on multi-dimensional analysis in a large acceptance experiment, and also the abilities and limitations of the integral method. Since the integral method produced systematically smaller radii parameters in the single dimensional analysis, it is expected this will carry over into multi-dimensional analysis.

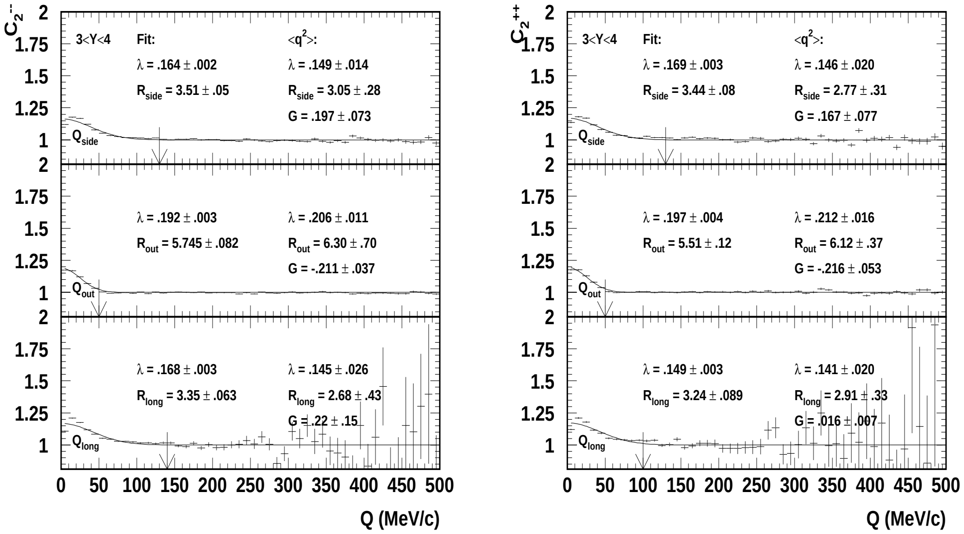

Figure 6.22: One-dimensional projections of the 3-d correlation functions and the extracted radii parameters from the fit and integral methods. Shown are results from 3<y<4 region for negatives (left) and positives (right) in VTPC1.

The parameters deduced from a fit are again from a χ^2 minimization. Extracting parameters from the integral method is slightly more contrived in the multi-dimensional case. Initially values were deduced by simply numerically integrating the 3-d function as done before in the one dimensional case. Although this was possible, there was an uncertainty in the extracted parameters of between 50-150%, which made the values more-or-less meaningless. The origin of this large uncertainty is two-fold. First, even with 87k events, there is a shortage of statistics. Recall that from the 1-d correlation functions the errors from the integral method were an order of magnitude larger than the fit method. Second, there is a rather large uncertainty in the cross terms of the tensor in momentum space (i.e. $< Q_i Q_j >$; see equation 3.16). These terms (and associated errors) are very large because the cross terms in configuration space (i.e. $< R_i R_j >$) are very small, and as such they dominate in the calculation. In order to circumvent these problems and extract parameters utilizing the integral method, the 3-d correlation function was projected into two

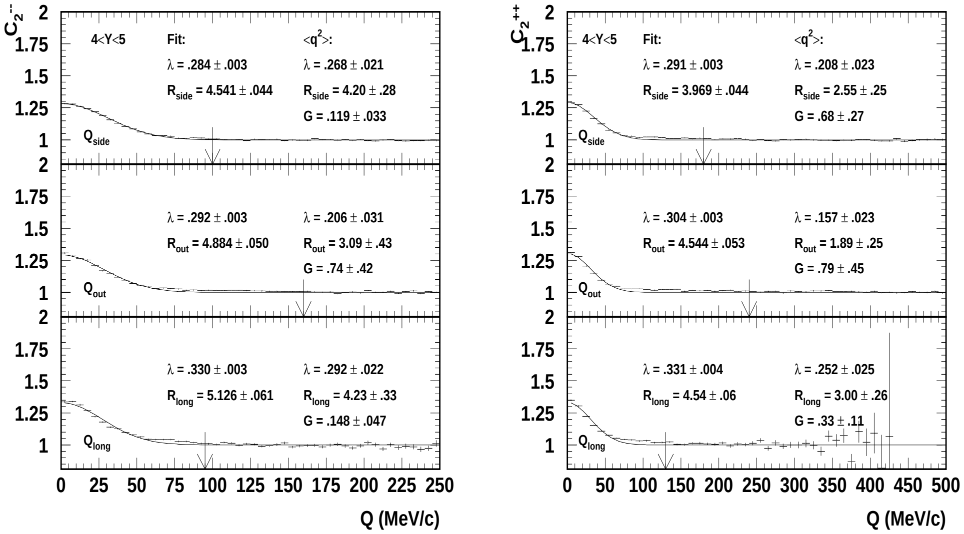

Figure 6.23: One-dimensional projections of the 3-d correlation functions and the extracted radii parameters from the fit and integral methods. Shown are results from 4<y<5 region for negatives (left) and positives (right) in VTPC2.

dimensions. Three projections are made: Q_L-Q_{Tside}, Q_L-Q_{Tout}, and Q_{Tout}-Q_{Tside}. This is shown in figure 6.24. The average number of entries per bin are calculated and a bin is used if it contains more entries than .9 of this value. This approximates the cut-off at the "cross-over" point as used in the one-dimensional case. The normalization, as in the Gaussian fit procedure, is taken from the correlation function in Q_{inv}. In order to simultaneously constrain the three radii parameters as is done in the fit method, the ratio of R_{Tout}:R_{Tside} is fixed by the projection Q_{Tout}-Q_{Tside}. R_{Long} is determined by the mean of the two values given by the Q_{Long}-Q_{Tside} and Q_{Tout}-Q_{Long} projections. Each projection defines its own cross term. There still exists a rather large uncertainty in the parameters, again attributable to the statistics and size of the cross terms, but they are well below the 100% level.

The first result to be presented from a 3-d correlation function is the value of the λ parameter in figure 6.25. The correlation function is constructed from 5k events with the single parameter Coulomb correction (see figure 6.9) and in

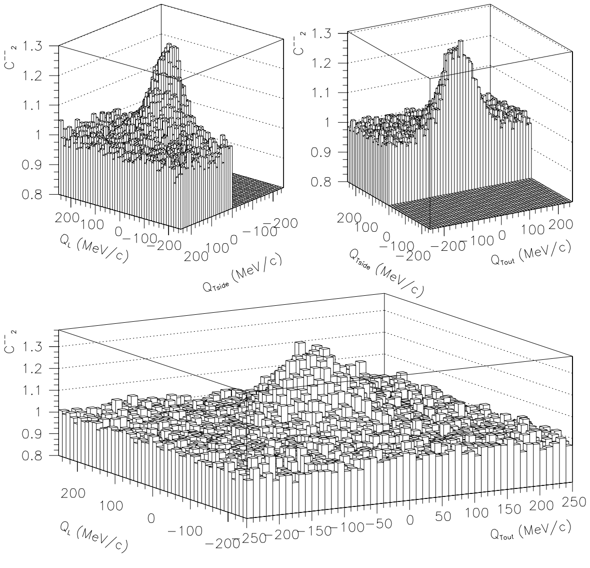

Figure 6.24: The three 2-d projections made to deduce the radii parameters using the integral method.

separate rapidity bins (Δy=1) using particle pairs independent of their transverse momentum or K_T. No PID is used. It is immediately obvious that there is a large systematic offset in λ between the two different VTPCs, when no PID is done. This may be attributed to the electron-positron contamination in VTPC1 which is not as prevalent in VTPC2, as explained previously.

Shown in figure 6.26 is the result of the current analysis when the 2 parameter Coulomb correction is used for the integral and fit method. Points deduced from data in which identified particle spectra were utilized are denoted by the triangle markers. There is a definite increase of the correlation strength with the use of identified spectra. This is seen in both the fit and integral methods. It is also interesting to note that the factor of 2 difference in λ as shown in figure 6.25 is reduced substantially. However, it seems that there is a systematic trend in all measurements made thus far that indicates a real K_T dependence on λ; that is, it decreases with increasing K_T. One may ask the question if the behavior of λ is an

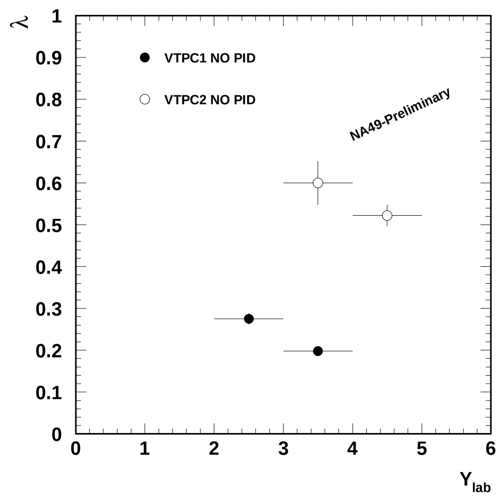

Figure 6.25: First attempt to extract λ from a correlation function. Data set is 10k events and 1 parameter Coulomb correction from figure 6.9 is used.

important because of the ambiguity in this parameter. Still, there appears to be a relation between it and the radii parameters, and if particle contamination distorts the value of λ, it is also likely that it distorts the value of the radii. This will be elucidated in the following discussion.

Shown in figure 6.27 are the radii parameters deduced from a multi-dimensional correlation function constructed from negative pairs with and without PID from the fit and integral methods. The analogous plots using positively charged pairs are contained in Appendix F. Like the λ parameter, there is an increase in the values by about 5-15% when PID is utilized. There is a small difference in the rapidity region 3<y<4 as reported by VTPC1 and VTPC2 but this due to the K_T dependence of the parameters. It will be shown in section 6.5 that there is a large and definite dependence of the radii on the pair transverse momentum. Again the values given by the integral values are of the order of 20% smaller than those obtained through a Gaussian fit procedure. There is no strong rapidity dependence in the radii parameters as observed in S–S collisions, as measured by NA35 [133]. The results from the S–S interactions revealed source sizes that peak at mid-rapidity.

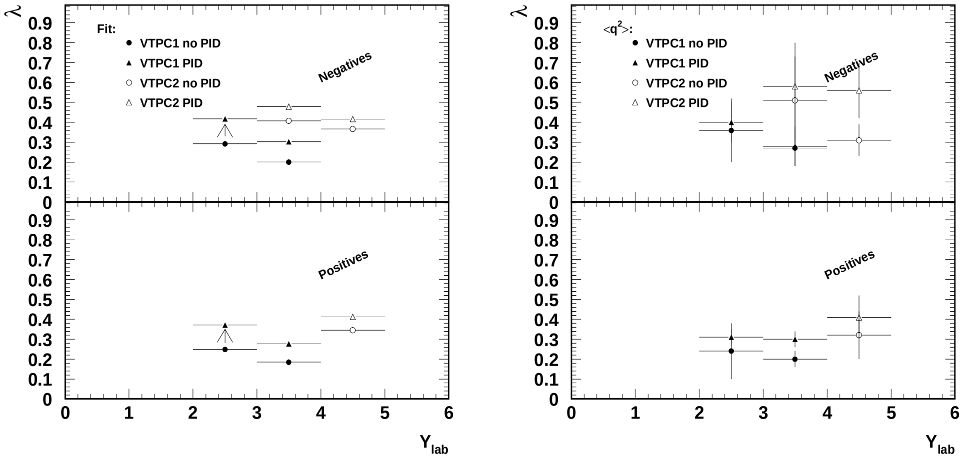

Figure 6.26: Comparisons of the λ parameter for the fit (left) and integral (right) methods for the 3 dimensional correlation functions. The effect of PID is also illustrated with an enhanced λ when identified particles are used.

The absence of such a peak in the Pb-Pb data leads one to believe that a more isotropic emission of particles occurs in larger systems. This flat dependence is also seen in the positive particle correlation functions (figure F.1), albeit the radii are systematically smaller. It should be remarked that the radii are of the order of a third smaller than previously reported [147]. This can be understood in terms of the different Coulomb correction that is being used in the present analysis. If the single parameter Coulomb correction is used, larger values, consistent with previous analysis are obtained [158]. Still, the relative differences between the parameters shown here should be of interest even if direct comparisons of the absolute values are not possible. More importantly, this underlines how dependent the results extracted from correlation functions are on the Coulomb correction. Because of the increase of the value of the parameters with the use of PID, it alters the interpretation of some physics. For example, it appears R_{Tside} is not affected to the same extent as the other radii. Thus when PID is utilized the difference between R_{Tout} and R_{Tside} (i.e. R_{Tout}–R_{Tside}) increases. Because this value is proportional to the duration to the time of particle emission, the lack of PID will underestimate the emission time. It is again a small effect, but not negligible, especially if one is searching for a small effect. It should also be pointed out that the difference in R$_{Tout}$ and R$_{Tside}$ as reported by the integral method is smaller that the Gaussian fit method, but still positive.

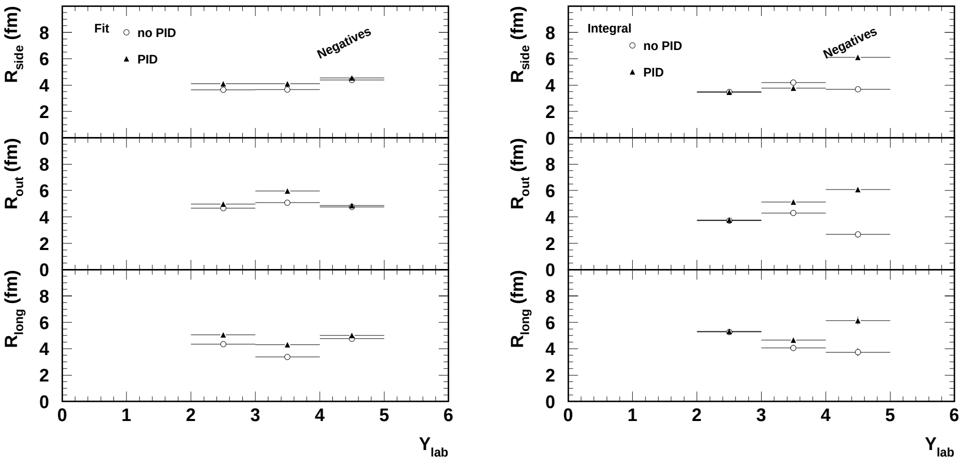

Figure 6.27: Comparison of the radii parameters extracted from the fit (left) and integral (right) methods, along with the effects of PID for each. This is strong evidence that PID does affect the correlation function in a non-negligible manner. The analogous plot for positive pairs is in appendix F.

The behavior of the cross term in the fit is shown in figure 6.28 (figure F.2 for positives). This term characterizes the asymmetry of the source in the transverse and longitudinal direction [162]. It vanishes at mid-rapidity and if the source is longitudinally boost invariant, the R$_O L$ term is expected to disappear in all regions of phase space. Strictly speaking a finite source is never *exactly* boost invariant as is evident by the finite term in the forward (and backward) rapidity region. Boost invariance would also show up in a flat $\frac{dN}{dy}$ spectrum which is not observed [62]. The cross-term approaches zero at mid-rapidity, and changes sign in the backward region, both with and without PID in the case of the negative particles, suggesting that electrons, although important in considering the value for λ, do not distort the cross-term to a large extent. The positive spectra shows the expected behavior only when PID is used. This suggests that the proton contamination does produce a measurable effect in the correlation function. The integral method is unable, in either case, to reproduce the correct behavior of the cross term. The other cross-terms (i.e R_{os} and R_{ls}) are expected to vanish in the limit that the source is cylindrically symmetric. In the case of the Gaussian fit, this is observed. The integral method predicts that the R_{os} terms vanishes, consistent with the Gaussian fit method, but the R_{ls} term is found to be of the same magnitude as R_{lo}. It is curious that G, the parameter that reports the deviation from Gaussian behavior, is found to be quite small. Furthermore, it is always as negative for the $Q_{Long}Q_{Tout}$ projection while positive for the others (i.e. $Q_{Long}Q_{Tside}$; $Q_{Tside}Q_{Tout}$). Upon closer inspection, it is found that at small relative momentum bins , the G parameter is very large. At a point of approximately 50 MeV/c, the parameter abruptly changes sign, becoming positive. Thus when the integral is computed, it is a rather small number; the sum of a large positive and a large negative number. Although the final number is small, it is clear that the functions are not Gaussian, and it would be unfair to report G as being small. In order to better quantify this value, further studies need be carried out.

6.5 Evolution of the Radii Parameters ($\mathbf{m}_T$ Dependences)

The evolution of the radii parameters with the pair momentum (K_T) is important because model studies have shown this to be sensitive to ordered flow effects. Figures 6.29–6.37 show the evolution of all the HBT parameters with m_T, where m_T=$\sqrt{K_T^2+m_\pi^2}$. Up until this point in time, such results have been reported as a function of K_T even though formalisms deduce source expansion in terms of m_T.

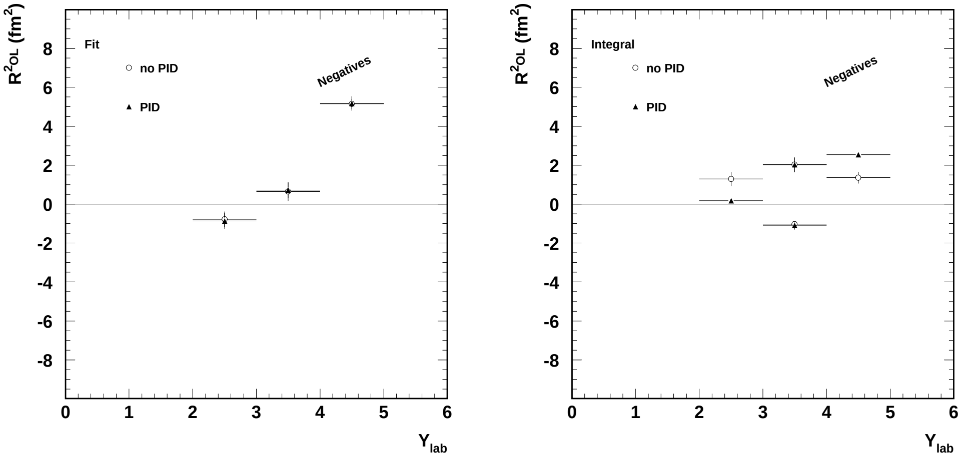

Figure 6.28: Comparison of the cross term R$_{ol}$ extracted from the fit (left) and integral (right) methods, along with the effects of PID for each. There is relatively little effect of PID. This is not the case for the positive pair correlation function (C^{++}) which is contained in appendix F.

For example:

$$\begin{aligned}
R^2_{Long} &= \tau^2 \frac{T}{m_T}[163] \\
R^2_{Long} &= \tau^2 \frac{T}{m_T} \frac{K_2(\frac{m_T}{T})}{K_1(\frac{m_T}{T})}[164] \\
R^2_{Long} &= \tau^2 \frac{T}{m_T}[1 + (\frac{1}{2} + \frac{1}{1 + \frac{m_T}{T} v^2}) \frac{T}{m_T})[165] \qquad (6.8)
\end{aligned}$$

where τ is the lifetime of the source, T is the freeze-out temperature, v is the flow velocity, and K_1 and K_2 are modified Bessel functions. Although non-identified particles may justify the presentation of the evolution in terms of K_T, identified particles allow the use of the variable m_T so direct comparison with theory can be made. The separation of the radii parameters into m_T bins acts as a wave-length filter in order to look at different regions of the source. Experimentally it is found that the radii appear smaller with increasing m_T. This evolution is found in models that assume a non-static source with hydrodynamic flow (see equation 6.8). If flow is non-existent the radii are expected to show no variation with m_T [67]. This is an important observation because single particle spectra convolute temperature and flow effects in a non-unique way. With a superposition of an ordered flow velocity field *and* random thermal motion, the inverse slope of single particle spectra can not be interpreted by a straight forward application of Hagedorn's thermal model. An ordered flow field will tend to blue-shift the temperature extracted from the slope of single particle spectra [166]. This is why in chapter 2 it was said that a first order phase transition could probably not be uncovered by a simple plot of event $<\mathrm{p}_T>$ versus event multiplicity without strong assumptions—the assumption being the absence of ordered flow. In order to deduce a measure of the thermal energy, one must do a simultaneous fit of the m_T dependences of single particle and two particle (correlation function) spectra.[7] Of course this procedure is highly model dependent, but it presents a more accurate picture of reality—the existence of thermal (random) and flow (ordered) motion. This interpretation is also able to account for the increasing slope parameters with particle mass; that is, $\mathrm{T}_\pi < \mathrm{T}_K < \mathrm{T}_p < \mathrm{T}_d$ [62]. If a freeze-out temperature of approximately 120-150 MeV is fixed and a flow velocity in introduced, m_T scaling returns [166]. Such simultaneous fitting of single and two particle spectra is currently underway at NA49 at this time and will be reported in an upcoming publication.

The m_T evolution of the radii parameters is presented in the following figures in three rapidity bins for negatively charged particles. The corresponding plots using positive particle pairs are given in Appendix F. In the rapidity region from $2<\mathrm{y}<3$ it is seen that PID has a significant effect on the λ parameter. This is shown in figure 6.29. The errors in the integral method are, as expected, much larger than the errors in the Gaussian fit method. For positive particles (figure F.3) there is a definite K_T dependence visible. The lack of this in the negative spectra indicates this may be due to problems with the PID. If one refers to figure 5.27, this is not hard to imagine. Furthermore, it is expected that at high momentum (high K_T) separation power will decrease. This appears to be evident in the behavior of λ.

---

[7] Of course, this still assumes the absence of temperature gradients.

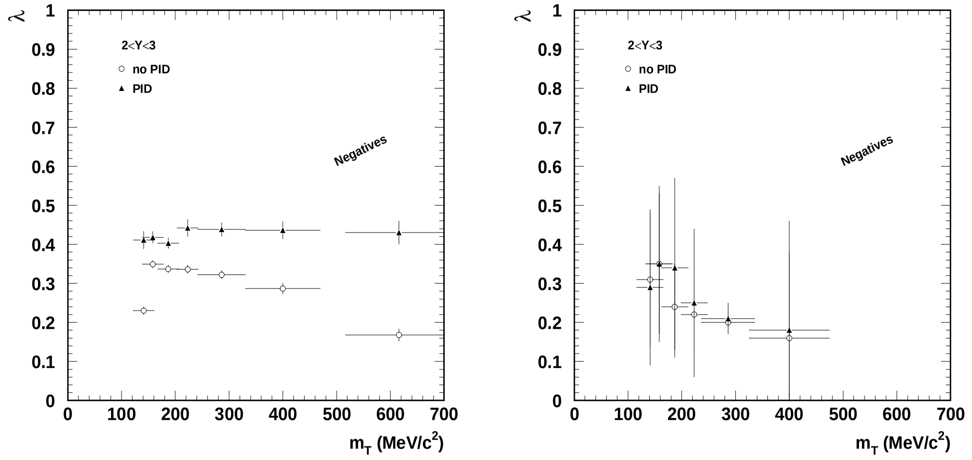

Figure 6.29: Comparison of λ extracted from the fit (left) and integral (right) methods, along with the effects of PID for in the rapidity interval 2<y<3. The effect of PID is larger with increasing K_T. The positive pair correlation function (C^{++}) is contained in appendix F.

In terms of the radii parameters, a characteristic decrease in radii with increasing m_T is observed. This is evidence that the point of emission of particles and their momentum are not independent. Mathematically it can be said that the emission function, S cannot be factored into a space and momentum component:

$$S_i(\mathbf{x},\mathbf{p}) \neq A(\mathbf{x}) \cdot B(\mathbf{p}) \tag{6.9}$$

Model calculations show that the result of the inability to factor these components result in an ordered velocity field or flow. The severity of the fall-off of the radius parameter with increasing m_T is proportional to the flow velocity. In a popular model due to Maklin and Sinyukov [163] the onset of idealized hydro-dynamic flow is given by $R(m_T) \propto m_T^{-\frac{1}{2}}$. At large densities (1500 particles emitted from a volume of a few hundred cubic Fermi's) the onset of hydrodynamic flow is not surprising. It can be seen that the much steeper decrease in R_{Long} than R_{side} indicates that flow is much stronger in the longitudinal than in the transverse directions, again consistent with Bjorken's model of scaled expansion [167]. Since there is no possibility

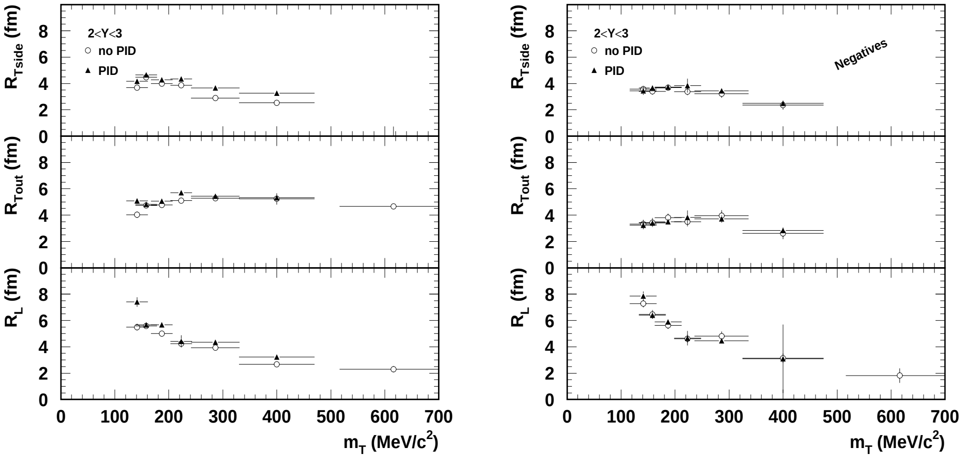

Figure 6.30: Comparison of radii parameters extracted from the fit (left) and integral (right) methods, along with the effects of PID for in the rapidity interval 2<y<3. The effect of PID is larger with increasing K$_T$. The positive pair correlation function (C^{++}) is contained in appendix F.

to differentiate the two transverse directions at zero average momentum, the two transverse radii are equal at K$_T$=0, as expected. As observed with the λ parameter, PID gives the largest deviation of radii at large m$_T$. It is also the case that modifications to the radii parameters due to the inclusion of π resonances modify the correlation parameters [168]. However this is believed to be a small effect for K$_T$ < 600 MeV/c. It appears that the change in radii (or regions of homogeneity) are more affected with the inclusion of PID than that expected from long lived resonances. Also note the increase in R$_{Tout}$ to a point of K$_T \sim m_\pi$. This is expected in the model of Chapman et al. [165] where R$_o(m_T)$ evolution is governed by:

$$R_o^2(m_T) = \frac{R^2}{1+\frac{m_T}{T}v} + \frac{1}{2}\tau^2(\frac{T}{m_T}\frac{K_T}{E_K})^2 \tag{6.10}$$

where E_K is the kinetic energy of the particle pair. The second term allows for an increasing radius parameter up to the scale defined by $\frac{K_T}{E_K}$—approximately the particle mass. Thus we see the increase of R$_o(m_T)$ in all the following plots until

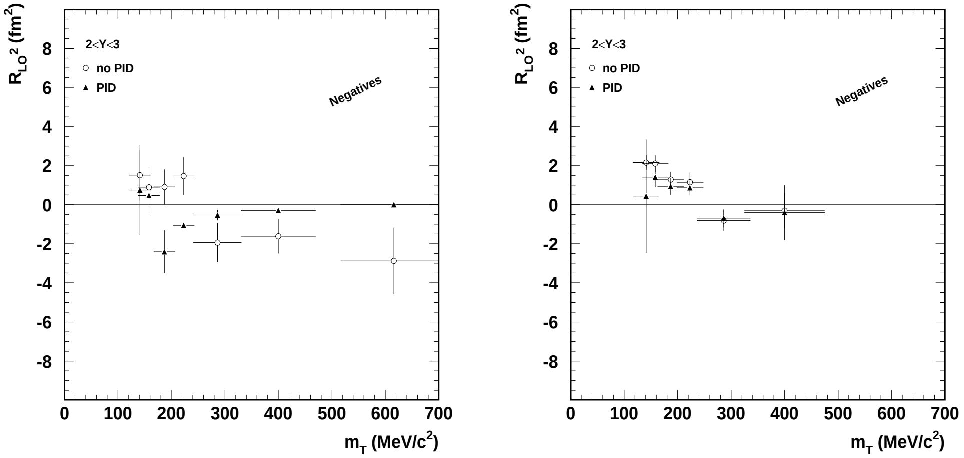

Figure 6.31: Comparison of cross term R_{ol} extracted from the fit (left) and integral (right) methods, along with the effects of PID for in the rapidity interval 2<y<3. The positive pair correlation function (C^{++}) is contained in appendix F.

the value K_T=m_π is reached and then it begins to decrease. It is not as dramatic in the case of the positive pairs. It appears that R_{Long} and R_{Tside} are the most affected by PID.

An interesting point is the cross-term in this region. It is expected to be zero when K_T vanishes (i.e. $m_T = m_\pi$). When PID is utilized, it is indeed consistent with zero. In the case of a non-boost invariant source, the term is expected to be finite. Because this region is backward of mid-rapidity, it is expected to be negative. This was observed in figure 6.28, but figure 6.31 shows its m_T evolution. In fact, it is negative at large m_T but appears positive a small m_T, albeit only when PID is not used. This seems to indicate that PID increases in importance as more differential measurements are made and that the physics interpretation of parameters can be altered if one is not careful about the particle composition. The integral method reports a positive value at small m_T, contrary to that of the fit results, but the cross term does also appear to be systematically negative at large m_T. Because the symmetric Pb-Pb source is expected to show symmetry about mid-rapidity, the cross term should be completely anti-symmetric with that in the rapidity interval 3<y<4.

As for the positive particles (figure F.5), the cross term appears positive at small m_T and negative at large m_T but appears to be diverging instead of approaching zero. Since the cross-term for the negative particle only shows the correct behavior when PID is used, this may be attributable to the quality of PID because it is known the separation power is not as good in the positive channel. It should be remembered that in the case of the negative particles, electrons are really the worst contaminant whereas the positive channel has protons in addition to the positrons. This implies, as suggested in section 6.2, that although e-π separation is possible in VTPC1, π-p discrimination requires significant improvement.

Figures 6.32–6.34 are the combined results from VTPC1 and VTPC2 in the rapidity region 3<y<4. There is a slight increase in the magnitude of λ with increasing m_T in the case where the fit method is applied. The effect of misidentification is largest in the region of low K_T. This is not surprising if one considers that VTPC1 is sensitive to the low K_T region and it seems to indicate that electrons are the most serious form of contamination to the h^-h^- spectra. The shape of the radii evolution follows qualitatively the form of those from the rapidity region 2<y<3 with again a slight increase in the values of the parameters when PID is utilized. Noting that the difference between R_{Tout} and R_{Tside} is very small over all K_T, it can be concluded that the lifetime of the source is also small. As expected R_{Tout} and R_{Tside} are equal at $K_T = 0$ where it is impossible to distinguish the two transverse directions. The cross term, as mentioned previously, is expected to show anti-symmetric behavior with respect to the rapidity interval 2<y<3. The values obtained from the fit do indeed show this behavior. The positive pairs (figures F.6–F.8) show a better agreement with the negatives in this rapidity interval, with the exception of R_{out} which appears to increase with increasing m_T. However, the integral method is unable to reproduce the profiles that the Gaussian fit procedure produces.

Figures 6.35–6.37 show the same evolutions in the rapidity region from 4<y<5, where there is very little change in the λ parameter with increasing m_T. Only at high K_T does λ begin to decrease. Again, this is expected if it is an effect due to PID because the separation power is degraded at high momentum (K_T). It is also

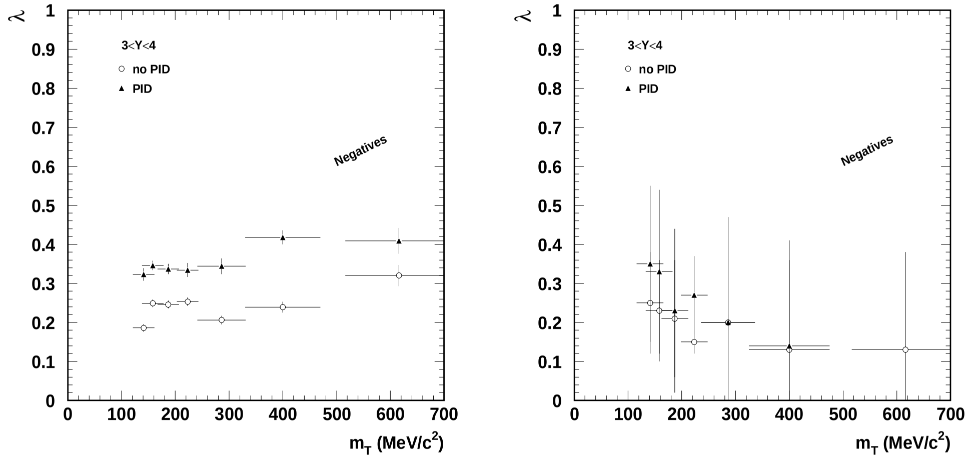

Figure 6.32: Comparison of λ extracted from the fit (left) and integral (right) methods, along with the effects of PID for in the rapidity interval 3<y<4. This combines VTPC1 and VTPC2 data. The effect of PID again appears to be large. The positive pair correlation function (C^{++}) is contained in appendix F.

noteworthy that there is about a 20% decrease in the value of λ over that deduced when a single parameter Coulomb correction is used (see figure 6.25). As expected the two transverse radii are equal at small K_T, and as in all the other cases, the evolution of R_{Long} with K_T is the strongest. In fact, this is even evident with the integral method. The behavior of the cross term is exactly what is expected. This is the first time it is seen to be consistent with zero at K_T=0. The integral method does not reproduce the small K_T behavior very well. In terms of the positive hadrons (figures F.9–F.11) the shapes of the K_T evolution are qualitatively the same as for the negatives with the exception of the cross-term. It is noteworthy that PID has little effect in this region except in the case of the integral method where there is a substantial difference. The same qualitative features are found as the previous rapidity regions.

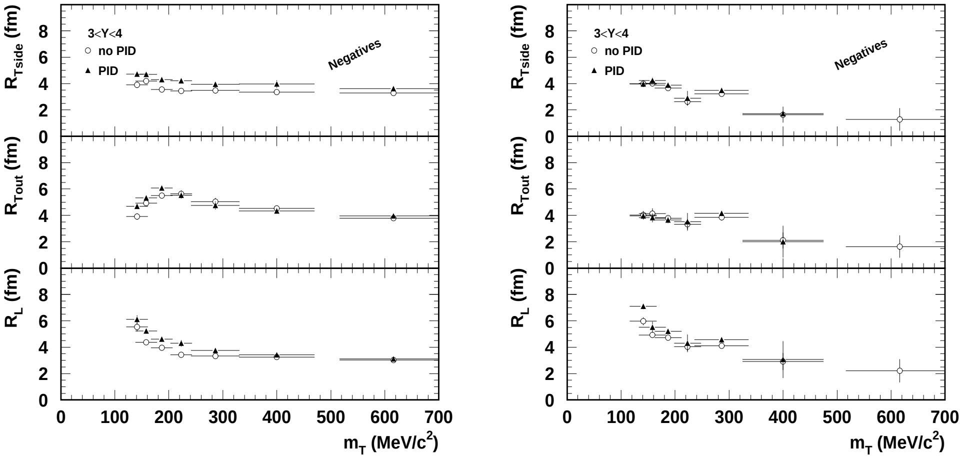

Figure 6.33: Comparison of radii parameters extracted from the fit (left) and integral (right) methods, along with the effects of PID for in the rapidity interval 3<y<4. This combines VTPC1 and VTPC2 data. The positive pair correlation function (C^{++}) is contained in appendix F.

6.6 Event-by-Event Possibilities

NA49 was designed with the goal of doing physics at the Event-by-Event level [169]. The philosophy of this analysis was discussed in chapter 2, but just to reiterate, its main purpose is to identify non-statistical fluctuations in physics observables. Although this analysis is in its infancy and the work presented here is by no means the last word, it is now possible to get an idea of the basic properties of single event correlation functions.

The most interesting question regarding correlation functions on an Event-by-Event level is how to construct the background. There is always the possibility of constructing a generic background from an ensemble of mixed events. In fact since the goal is to search for fluctuations from average event properties, this may be very suitable. However, the use of a quantity deduced from an ensemble seems to violate the spirit of such analysis. Using the lessons from Goldhaber et al. [49], who found evidence of the Bose-Einstein correlation in comparison of the opening angle distribution with like and unlike sign pairs within a single event, it is possible to

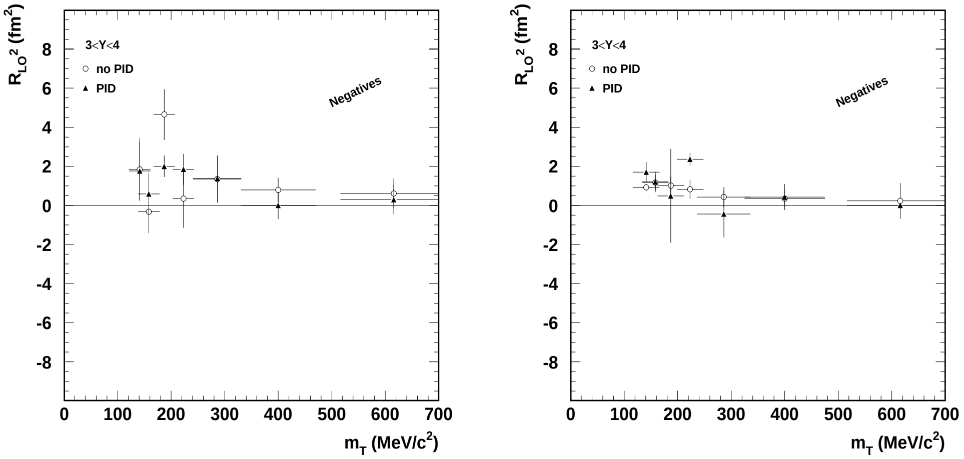

Figure 6.34: Comparison of the cross term R_{ol} extracted from the fit (left) and integral (right) methods, along with the effects of PID for in the rapidity interval 3<y<4. Anti-symmetry with the respect to figure 6.31 is observed, as expected. The positive pair correlation function (C^{++}) is contained in appendix F.

construct both the signal *and* background from a single event. That is, the signal can be constructed from the like-sign pairs, and the background can be constructed from the opposite sign pairs as in equation 6.11:

$$C_{ebe} = \frac{Y(h^-h^-)}{Y(h^+h^-)} \tag{6.11}$$

In contrast to the event mixing procedure for determining the background, this method will contain kinematic correlations due to energy-momentum conservation of the event while excluding any Bose-Einstein correlations. Moreover, correlations due to resonance decay will be implicit in this background.

The first attempt using this approach utilized only the negative pairs for the signal and all the mixed ("+−") pairs for the background, that fell within the acceptance of the VTPCs [158]. No other cuts were made in order to keep the maximum number of particles. Since the correlation function was calculated in terms of the historical variable Q_{inv}, no Coulomb correction was done. However, considering

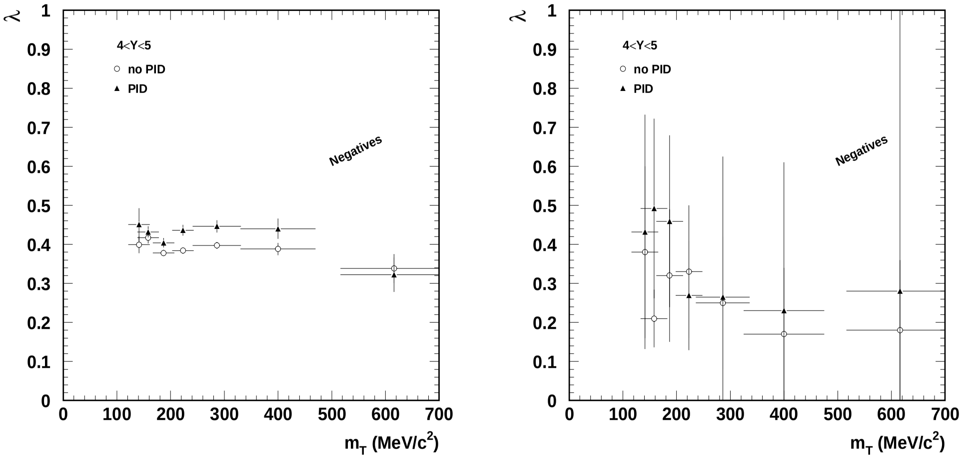

Figure 6.35: Comparison of λ extracted from the fit (left) and integral (right) methods, along with the effects of PID for in the rapidity interval 4<y<5. The effect of PID is quite small in this region leading one to speculate that electrons (and positrons) are the main cause of the discrepancy between identified and non-identified correlation functions. The errors are considerable larger with the integral method reflecting the cumulative effect of the errors on all bins. The positive pair correlation function (C^{++}) is contained in appendix F.

figure 6.11 where the Coulomb correction is applied as a function of Q_{inv}, it is not clear that one can draw any conclusions from the correlation function in the same variable (i.e. Q_{inv}). Furthermore the normalization must be calculated from the same spectrum. The region between 200-400 MeV/c is used for this purpose. The correlation function that resulted was a rather broad distribution that gave a radius of ∼2-4 fm, albeit with large errors—of the order of 50%. The large uncertainty indicates that, at least at CERN-SPS energies, multi-dimensional analysis of the correlation function will probably not be possible at the event level. This is a concern because it is not clear whether or not meaningful information can be extracted from a Q_{inv} spectrum, or any other single dimensional variable. This is a question that will have to be considered in future theoretical studies.

A typical central Pb-Pb event produces between 600-1200 particles which are detected within the VTPCs which means ∼450k pairs are available to construct a correlation function, so one may justly wonder why statistics appear so limited.

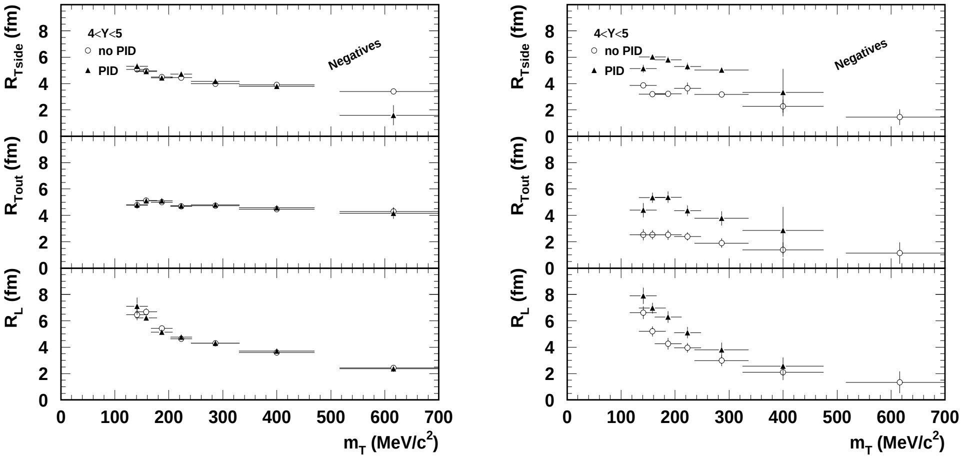

Figure 6.36: Comparison of radii parameters extracted from the fit (left) and integral (right) methods, along with the effects of PID for in the rapidity interval 4<y<5. The positive pair correlation function (C^{++}) is contained in appendix F.

The reason is because the particles are distributed over all phase space and it is only the pairs that are close in momentum space that actually correlate. Because there is no evidence for a difference in radii between the "++" and "−−" channels, including PID in the selection of particles allows for a simple extension to equation 6.11 which effectively doubles the number of pairs used in the signal by including the positive hadron pairs as shown in equation 6.12:

$$C_{ebe} = \frac{Y(\pi^-\pi^-) + Y(\pi^+\pi^+)}{Y(\pi^+\pi^-)} \tag{6.12}$$

Although the ensemble correlation functions showed that the PID capablilities in VTPC1 were marginal for selecting a pure pion sample, they will be improved in the near future with global tracking. Nevertheless, it is worthwhile to look at the first indications of a signal with this approach to see if meaningful results can be obtained and to get an idea of the statistical power available. The first results are shown in figure 6.38.

The first thing one notices is that the errors on the bins are very large. The

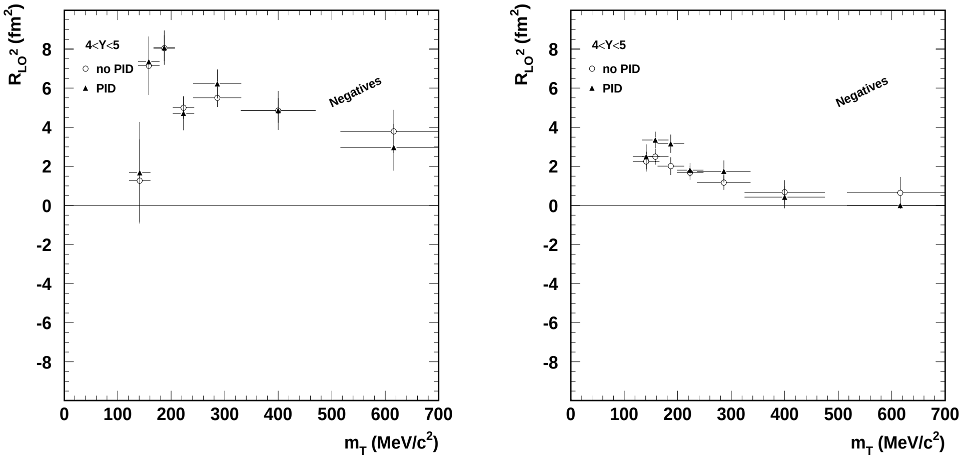

Figure 6.37: Comparison of the cross term R_{LO} extracted from the fit (left) and integral (right) methods, along with the effects of PID for the rapidity interval 4<y<5. The expected behavior is observed. The positive pair correlation function (C^{++}) is contained in appendix F.

width of the correlation function also appears to be narrower than those obtained from ensemble analysis. Since the errors are large, the integral method will be used because the region of sensitivity can be easily adjusted with the integration limits. A truncation at the cross-over point, as was done in the ensemble analysis, would result in the use of only 2-3 bins which would be insufficient to characterize the correlation function. Instead the first 100 MeV/c interval was integrated. The reason the interval 0-100 MeV/c was chosen was that it contains the complete region where the enhancement is expected and extends slightly beyond. Thus, a small bit of shape information is also included such that fluctuations should be detectable at both the size and shape level. It is noteworthy that the interval that is integrated determines the general size. That is, the fewer the number of bins used in the integration, the larger the size. This is not unexpected in light of the previous finding in examining ensemble correlation functions and can be seen in figure 6.38 where the correlation function in the top plot has a larger $< q_{inv}^2 >$ integral than the bottom plot from inspection (i.e. more bins contribute). This is reflected in the smaller value of R_{inv}.

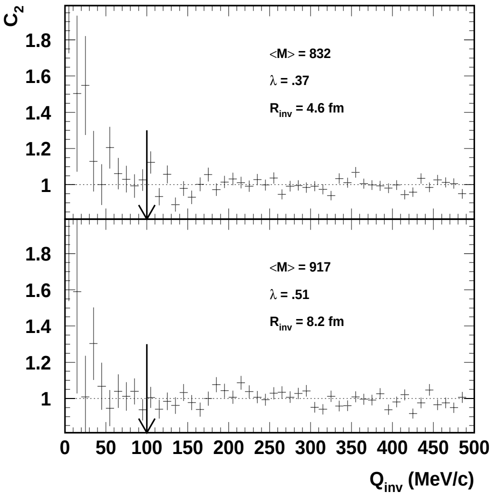

Figure 6.38: Typical correlation functions constructed from the tracks within the VTPCs of a single event with *no* cuts made. Shown are the radius parmeter R$_{inv}$, the correlation strength λ, and the event multiplicity M. Although the statistics are marginal, the correct shape and reasonable radius parameter is found.

The distribution of R$_{inv}$ and λ from 5000 events is shown in the left most panel of figure 6.39. The three distributions that are shown correspond to three different cuts of differing severity. The "no cuts" case (dotted line) uses all tracks that are found within the acceptance of the VTPCs in the construction of the correlation function. The second—"full cuts, no PID" (dashed line)—refers to cuts being imposed as outlined in section 6.1; that is, cuts based on track length, vertex position, two-track separation distance, and minimum Q$_{inv}$ were utilized. This means that all particles in the rapidity region 2<y<5, independent of their K_T were used. Finally, "full cuts, with PID" (solid line) includes the above cuts with the additional requirement that the specific ionization of the track be consistent with that of a pion. It should be noted that effects due to double counting of tracks should be small because of the relatively small overlap of VTPC1 and VTPC2. Although the inclusion of MTPC data would increase the multiplicity of each event, the large overlap between VTPC2 and MTPC would cause problems due to track double counting. The use of all tracks from all detectors will have to wait for the global tracking chain.

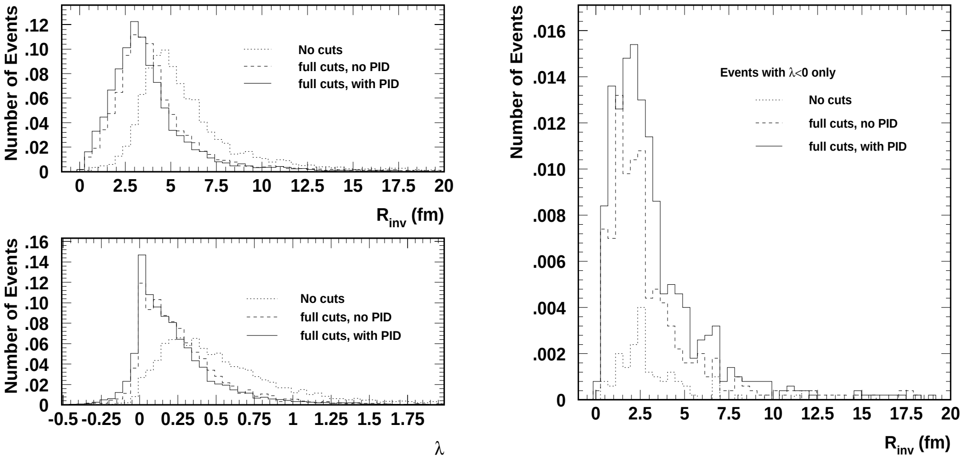

Figure 6.39: On the left, the distribution of R$_{inv}$ and λ from 5000 events. On the right, only events with a λ parameter that is negative are selected. These are cut, regarded as unphysical in the analysis. These account for ~2% of the total sample

It is curious that the distributions of both R$_{inv}$ and λ narrow as the cuts become more restrictive. This suggests that fluctuations can be induced in the correlation function due to effects *not* inherent to Bose-Einstein correlations with this method like the inclusion of non-vertex tracks, electrons, etc. Although the distributions become narrower, the resolution R ($=\frac{\sigma}{mean}$), remains constant at ~8.5%. The systematically larger R$_{inv}$ with the absence of any cuts leads one to believe that the fluctuations in the small Q$_{inv}$ region are dominated by counting statistics rather than something more fundamental, like a phase transition. In fact for the events that have a very small number of low Q$_{inv}$ pairs, the integral of the correlation function can actually become negative. These events are a small fraction (98/5000 or ~2%), but they produce events with a small radius as well. This highlights a short-coming in the integral method that λ and R$_{inv}$ are not linearly independent. The distribution of R$_{inv}$ for these events is shown in the right most plot of figure 6.39.

Cutting the unphysical events with negative λ allow a distribution of the radius parameter, R$_{inv}$ versus the event multiplicity to be made, again with the varying severity in the cuts. This is shown in figure 6.40. This not only shows the magnitude

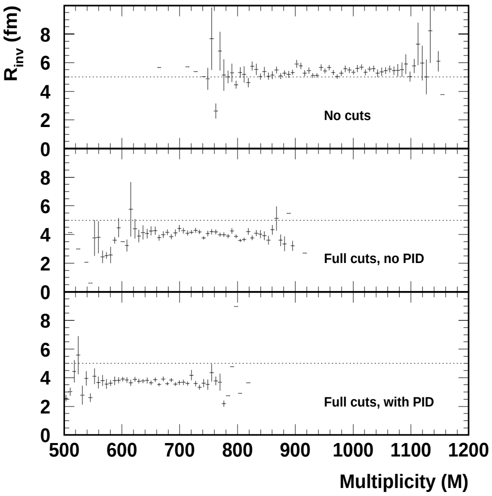

Figure 6.40: The correlation between R_{inv} and event multiplicity for the various cuts. Although it is obvious there is a change in the radius parameter with the different cuts, there is no strong variation in source geometry, characterized by R_{inv} with multiplicity. A line at 5 fm is drawn as a reference mark only.

of the number of tracks that are rejected with the cuts, but also that the radius parameter extracted is a very stable parameter with event multiplicity. Although it may be suggested that there is a very slight increase with multiplicity when no cuts are made, this effect disappears with the introduction of the cuts. The error shown in the figure is only statistical. Although it may be argued that the trigger utilized does not allow a large enough variation in centrality, there will be difficulties in constructing correlation functions in events with smaller multiplicities. Further progress awaits first results from the global tracking chain.

From these preliminary results, one can draw several conclusions. The first is that the multiplicity of Pb-Pb events at CERN SPS energies is marginal with which to construct single-dimensional correlation function. Although the construction of a background from an ensemble of events may reduce the statistical uncertainty in the denominator, one cannot discount the possibility that extracting the signal and background from the same event may have greater sensitivity because either the signal (numerator), or background (denominator) may exhibit fluctuations. The second obvious conclusion one can draw is that there is no evidence for a large scale fluctuation of the parameter R_{inv} with event multiplicity. Although this does not rule out the possibility of something happening in a small subset of the events, the errors in the present analysis will have to be reduced considerably before any such conclusions can be made.

6.7 Summary and Conclusions

The most important work carried out in this thesis was the use of ionization information in the VTPCs to facilitate PID. Along with this the first measurement of the specific ionization curve for $NeCO_2$ (90:10) (i.e. I/I_o versus p) was made and documented. This information was then used in the construction of a proton-proton correlation function in the VTPCs illustrating that it is indeed feasible to carry out such studies.

The first measurements of correlation functions in the backward rapidity region were also presented. Their properties, as expected, were symmetric about mid-rapidity when electron contamination was removed. This showed that the particle composition of the particle spectra was important in terms of extracting physics from a correlation function. Correlations constructed with quasi-identified particles were compared to those with unidentified particles. The results indicated that PID has a significant effect on not only the λ parameter, but also the radii, and the cross term. It was also shown that the expansion of the source is much stronger in the longitudinal than transverse directions, independent of rapidity interval considered. The evidence of this ordered flow allows for a rather elegant explanation of the anomalously large temperatures extracted from single particle spectra in a way that restores m_T scaling. Although the K_T evolution of these parameters are qualitatively the same, the magnitudes increase an appreciable amout—at the 10% level—with the use of identified spectra. This has implication in terms of the lifetime of particle emission because the lifetime is proportional to the difference between

R$_{Tout}$ and R$_{Tside}$. Because the largest differences in the different radii were seen in VTPC1, it can be inferred that the contamination due to electrons and positrons was most serious in terms of distorting the correlation function. Although capabilities for PID need to be improved from the present situation, the construction and study of correlation functions with positive particles (both pions and protons) seems feasible. In fact, even differential measurements with protons seem possible. However, in comparing the results obtained from π^+-π^+ correlation functions with those of π^--π^-, it is not clear that there is an asymmetry introduced because of different rescattering effects as suggested in section 6.1.3. In the regions where there is confidence in the PID capabilities (i.e. VTPC2 at low momentum), the two channels do agree within statistical error. The uncertainty in the PID capabilities in the two channels is large enough so that a definite statement can not be made at this time. Hopefully with the arrival of the Kr calibration and inclusion of a better calculation for the crossing angles, the $\frac{dE}{dx}$ capabilities will improve.

A method to extract radii parameters from the correlation functions *without* the use of a fitting algorithm was also used for the first time. Although perhaps useful in the extraction of parameters from one and two dimensional correlation functions, its appetite for statistics will limit its use in current experiments—especially in terms of multi-dimensional analysis. Still, regardless of the method utilized, it became painfully clear that the entire credibility of correlation function rests with the premise of understanding the Coulomb correction and applying it correctly to the data. It was also demonstrated that a major cause for non-Gaussian behavior of the correlation function is rooted in the Coulomb correction. Although there are still small deviations from Gaussian shape seen in an uncorrected correlation function, it is clear that the sensitivity required to study such fluctuations in a systematic fashion will require the order of 10^{10} pairs! The present uncertainty in the Coulomb correction leads one to ponder the possibility of extracting geometric information from the "$+-$" spectra directly as a means of reducing systematic uncertainty. On the other hand, perhaps it is wise to look at uncharged particles with which to construct correlation functions. NA49 has a large sample of reconstructed K^o's;

they seem ideal for this study. However the superposition of K_L^o and K_S^o in such a sample could also cause large uncertainties.

It is perhaps necessary to comment on the absence of any simulation studies in regards to correlation functions in this thesis. In order to calculate real Bose-Einstein correlation effects, one needs to solve a quantum-mechanical, relativistic many-body problem, which in itself is not a pleasent thing with which to deal. However, this is further complicated by having to carry out such a calculation in the region governed by non-perturbative QCD. Obviously this is not feasible at present so an appoximation is required. In fact there are methods of generating correlations in Monte Carlo events. However, the correlation is superimposed on an event after the final state particles have already been generated. It is carried out by shifting the momentum of final state particles such that exchange symmetry is ensured. Besides the obvious violation of energy and momentum conservation, this is, in my opinion, a rather poor approximation. Any real correlation is generated in the dynamics and evolution of a reaction, not in the final state interactions unless the correlations are exclusively due to rescattering. If this is the case, correlations should also be visible in the $\pi^+\pi^-$ channel, which is contrary to experimental findings. If the physics the correlation function purports to contain can be reproduced by shifting the final state momenta of particles this line of study, in regards to investigating the hadronic equation of state, is probably not worth pursuing any further. Thus, what conclusions can one draw from simulation? If data does agree with simulation data produced by this procedure it suggests that the correlation is not inherent to the dynamics of the system and has its basis in the final state interaction. If it does not agree, one can always argue that the simulation is not sophisticated enough. For these reasons, I believe simulation has no place in correlation studies, other than perhaps confirming that one's software is formally functioning.

Finally, the last section of the thesis suggested a method for constructing a correlation function from a single event, and the first results were presented. This is definitely not the final word, and when all detectors can be used together with better PID, there should be a modest increase in statistical power. With the current statistics, using a fixed integral truncation, a characterization of the radius R_{inv}, and λ were made at the event level. It was also shown that the use of identified spectra is important for removing large scale pseudo-fluctuations in event-by-event correlation functions. Large scale fluctuations of R_{inv} with event multiplicity were not observed which indicates that this technique did not isolate an event class with different or anomalous properties. Furthermore the uncertainty in the extracted parameters was large indicating that the statistics at CERN-SPS energies are marginal. This implies that probably nothing beyond a single dimensional correlation function is possible at present. Nonetheless, NA49 should serve as a valuable training ground for future event-by-event analysis programs in the coming phase of heavy ion experiments, most notably, STAR and ALICE.

Appendix A

Abbreviations

AA	nucleus-nucleus
ADC	Analog to Digital Converter
BNL	Brookhaven National Laboratory
CEBAF	Continuous Electron Beam Accelerating Facility
CERN	Organisation Européenne Pour La Recherche Nucléaire Europenan Organization for Nuclear Research
CT	Control and Transfer
DSP	Digital Signal Processor
ECR	Electron Cyclotron Resonance
ELFE	Electron Laboratory For Europe
EM	Electro-Magnetism
EOS	Equation of State
EPI	External Particle Identifier
EW	Electro-Weak
FEE	Front End Electronics
FG	Frisch Grid
GG	Gated Grid
GSI	Gesellschaft für Schwerionenforschung
GR	General Relativity
HBT	Hanbury-Brown and Twiss
HV	High Voltage
ISIS	Identification of Secondaries by Ionization Sampling

ISR	Intersecting Storage Ring
LBNL	Lawrence Berkeley National Laboratory
LINAC	Linear Accelerator
LCMS	Longitudinal Co-Moving System
LEP	Large Electron-Positron Collider
LHC	Large Hadron Collider
MIT	Massachusetts Institute of Technology
MSM	Minimal Standard Model
MTPC	Main TPC
MWPC	Multi-Wire Proportional Chamber
NA49	North Area 49
NN	Nucleon-Nucleon
QCD	Quantum Chromodynamics
QED	Quantum Electrodynamics
QGP	Quark Gluon Plasma
QNP	Quark Nuclear Physics
OPEP	One Pion Exchange Potential
PRF	Pad Response Function
PEP	Positron Electron Project
PID	Particle IDentification
PS	Proton Synchrotron
PSB	Proton Synchrotron Booster
RB	Receiver Board
RF	Radio Frequency
RHIC	Relativisitic Heavy Ion Collider
SC	Slow Control
SCA	Switched Capacitor Array
SLAC	Stanford Linear Accelerator
SPS	Super-Proton-Synchrotron
STAR	Solenoidal Detector at RHIC
TDC	Time to Digital Converter
TJNAF	Thomas Jefferson National Accelerating Facility
TPC	Time Projection Chamber
TTR	Two Track Resolution
VM	Vertex Magnet
VTPC	Vertex TPC

Appendix B

Hadron Stability

A partition function, Z can be written as the Laplace transform of the density of states, σ:

$$Z = \int dE\, \sigma(E,V) e^{-E/T} \tag{B.1}$$

In QCD the density of states is the mass spectrum of the hadrons, $\rho(m)$. Substituting into the above equation results in:

$$Z_{hadron} = \int dm\, \rho(m)\, e^{-m/T} \tag{B.2}$$

so if the mass spectrum is restricted to a single species; i.e. a pion, the density of states becomes a delta function:

$$\rho(m) = \delta(m - m_\pi) \tag{B.3}$$

and the equations for an ideal pion gas are recovered. If the spectrum is taken as an exponential, which is more realistic:

$$\rho(m) = m^a e^{bm} \tag{B.4}$$

where a and b are parameters that define the spectrum. Thus:

$$Z_{hadron} = \int dm\, m^a\, e^{bm} e^{-m/T} \tag{B.5}$$

and Z_{hadron} diverges for $b = 1/T$, where b is a parameter that defines the lowest lying state. In the case of hadrons, this is the pion. Thus the partition function has a singularity at a temperature of $T_c \sim m_\pi$ which is interpreted as the point of a phase transition at which normal hadronic matter cannot no longer exist.

Appendix C

Thermodynamics

The distribution of the number of particles per state is given by the Planck function, f($\mathbf{k}$):

$$f(\mathbf{k})d^3\mathbf{k} = \frac{1}{(2\pi)^3}\frac{d^3\mathbf{k}}{e^{\beta\epsilon}-1} \tag{C.1}$$

The total number of particles is then given by integrating the above over all states:

$$N = \int_0^\infty f(\mathbf{k})d^3\mathbf{k} \tag{C.2}$$

which gives:

$$N = \frac{g}{(2\pi)^3}\int \frac{dk\, dy\, k^2}{e^{\beta\epsilon}-1} \tag{C.3}$$

Thus:

$$\frac{dN}{dy} \propto T^3 \tag{C.4}$$

It is also known that the total energy of the system, ϵ is given by:

$$\epsilon = \int \epsilon\, f(\mathbf{k})d^3\mathbf{k} \tag{C.5}$$

which means:

$$\epsilon \propto T^4 \tag{C.6}$$

This is a simple result from the ideal gas. However, from this and the relation between the entropy, S, temperature, T, and energy, ϵ:

$$S = \frac{d\epsilon}{dT} \propto T^3 \tag{C.7}$$

a relation between the entropy and multiplicity can be deduced:

$$S \propto \frac{dN}{dy} \tag{C.8}$$

So a plot of $\frac{dN}{dy}$ versus $<\mathrm{p}_T>$ would be an analog to a plot of entropy versus temperature. This may uncover evidence of a first order phase transition in the context of a simple thermodynamic model.

Appendix D

Energy Loss in Gaseous Materials

The following tables are a small compilation of some of the specific ionization data available for various counter gases at atmospheric pressure. The values quoted are without errors. However, most authors report an uncertainty of at least ±5%. Beyond this precision, the method used to extract the most probable value can play a significant role. In most cases, the authors have used a simple truncation algorithm. This along with detector geometry and operating conditions as well as characteristics of electronics and environmental factors has a non-negligible effect on the results.

Also included in table D.4 are first results from VTPC2 which contains $NeCO_2$ (90:10). NA49 is the first experiment to use this chamber gas during data taking.

Ionization in Ar/Ne mixtures			
$\beta\gamma$	$ArCH_4$ (90:10) [136]	NeC_2H_6 (90:10) [137]	NeC_2H_4 (90:10) [120]
5.3	1.010	1.005	1.005
10.7	-	1.070	-
16.0	1.125	1.135	-
21.3	1.170	1.185	-
32.0	1.235	1.255	-
35.8	1.260	1.285	1.295
53.3	-	1.330	-
71.6	1.365	1.390	-
74.6	-	1.385	-
101.3	-	1.420	-
107.5	1.410	1.450	-
141.8	-	1.490	-
143.3	1.435	1.453	-
214.9	1.465	1.520	-
358.2	-	1.530	-
9785	1.600	1.600	1.610
19570	1.610	1.590	-
29350	1.625	1.585	-
39140	1.610	1.595	-

Ionization in $ArCH_4$	
$\beta\gamma$	$ArCH_4$ (95:5) [130]
5.3	1.010
9.6	1.080
10.4	1.090
17.1	1.140
20.9	1.180
32.4	1.255
41.9	1.275
52.3	1.305
64.5	1.310
67.0	1.330
73.3	1.350
94.2	1.375
115.1	1.410
140.4	1.420
211.3	1.465
281.5	1.475
2837	1.505
9785	1.610
39139	1.575

Table D.1: Ionization values for some Ar and Ne based chamber gases.

Ionization in HeC_2H_6

$\beta\gamma$	HeC_2H_6 (50:50) [138]
1.05	1.403
1.31	1.278
1.50	1.190
2.18	1.074
2.95	1.003
3.73	1.0
5.1	1.016
7.1	1.036
11.6	1.088
14.4	1.096
17.9	1.113
29.2	1.136
1186	1.232
3951	1.253

Ionization in C_3H_8 based mixtures

$\beta\gamma$	C_3H_8 [134]	$XeC_3H_8CH_4$ (87.5:5.0:7.5) [134]
1.05	1.409	-
1.40	1.212	-
1.68	1.080	-
2.18	1.042	1.060
3.30	1.0	1.0
14.2	1.113	1.162
21.2	1.152	1.230
35.7	1.190	1.310
64.8	1.232	1.418
3958	1.251	1.690

Table D.2: Ionization values in some C_nH_{2n+2} based gas mixtures.

Ionization in $ArCO_2$

$\beta\gamma$	$ArCO_2$ (80:20)[139]
4.51	1.001
6.03	1.007
10.0	1.007
14.8	1.134
35.4	1.224
53.8	1.291
65.0	1.324
105	1.371
118	1.420
154	1.456
172	1.466
675	1.463
1025	1.554
48500	1.535

Ionization in Ar

$\beta\gamma$	Ar [139]
26.6	1.208
53.2	1.251
106	1.323
160	1.409
178	1.420
714	1.414
1070	1.512
49000	1.485

Table D.3: Ionization values in some Ar based gas mixtures.

Ionization in $NeCO_2$	
$\beta\gamma$	$NeCO_2$ (90:10)[NA49]
2.39	1.101
2.93	1.039
3.46	1.001
3.99	1.000
5.20	1.046
8.39	1.122
10.66	1.146
12.92	1.161
23.28	1.227
33.13	1.268
36.72	1.283
52.84	1.322
74.33	1.359
107.7	1.396
145.1	1.418
3423	1.556
4401	1.556
5379	1.558
6357	1.547

Ionization in $ArCO_2$	
$\beta\gamma$	$ArCO_2$ (80:20) [140]
2.99	1.038
4.1	1.0
7.07	1.020
9.09	1.045
13.3	1.078
15.3	1.094
17.1	1.113
21.5	1.134
30.4	1.167
47.3	1.218
105.9	1.284
155.5	1.321
271.2	1.361
389	1.368
1410	1.417

Table D.4: Ionization values in some CO_2 based gas mixtures. Shown left is the first measurements from VTPC2 in NA49.

Appendix E

Effect of PID and the Coulomb Correction on Correlation Functions

Following is a compilation of correlation functions deduced from both positively and negatively charged particles, with and without PID. They include 1-dimensional functions in Q_{inv} with and without the two parameter Coulomb correction. Also included are the projections of the 3-d Pratt-Bertsch (LCMS) correlation function into the Transverse (Q_T) and Longitudinal (Q_L) components. This is meant as an illustration of how the Coulomb correction alters the shapes of the correlation functions. Shown in the following figures are the parameters extracted from the fit and integral methods. It can be seen that both R_T and R_L, in all rapidity regions, posses non-Gaussian structure. The Q_L projections systematically show a bump at the base of the enhanced region (∼100 MeV/c). While this is not as strong in the Q_T functions, these have a very noticeable slope in their profile. This is evident in the much larger G parameter extracted from the Q_T than the Q_L spectrum. As expected with this large deviation from Gaussian behavior, the radii parameters extracted from the integral method is much smaller than the fit method. The differences in the methods are discussed in detail in section 6.2.

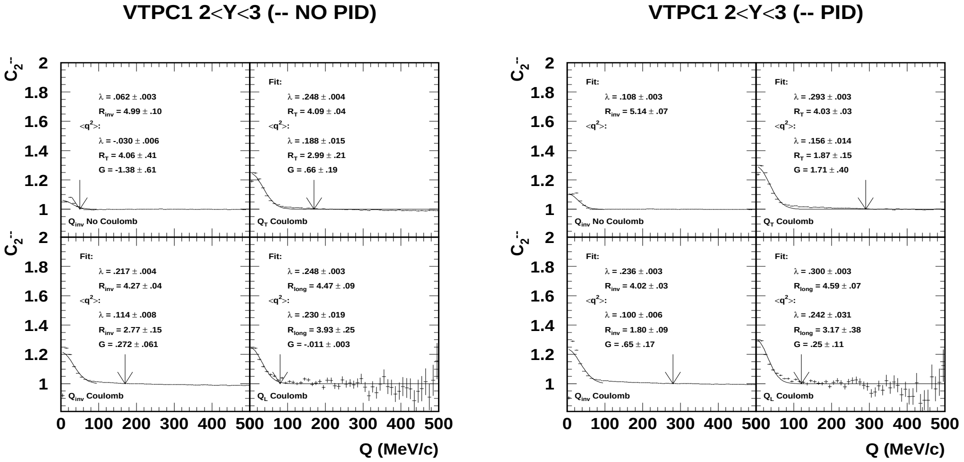

Figure E.1: Comparison between radii parameters from fit and integral methods for 1-d projection of a multi-dimensional correlation function, C^{--} in the rapidity region 2<y<3.

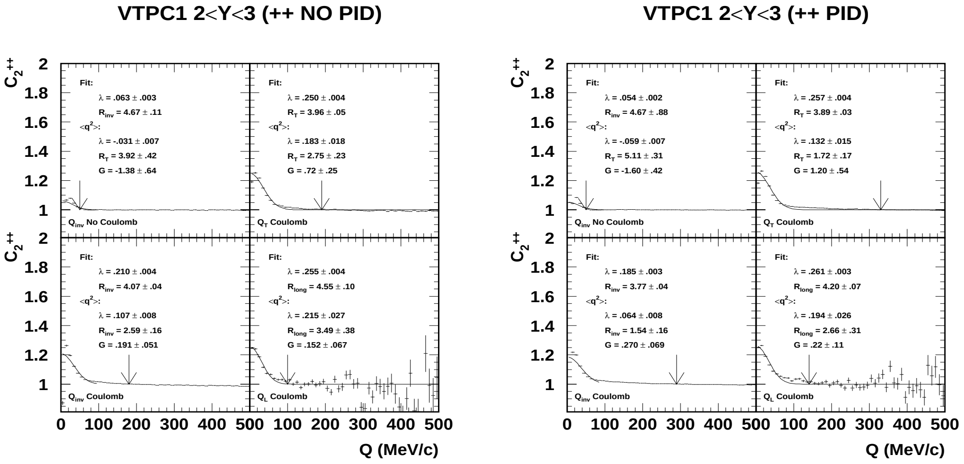

Figure E.2: Comparison between radii from fit and integral methods for 1-d projection of a multi-dimensional correlation function, C^{++} in the rapidity region2 <y<3.

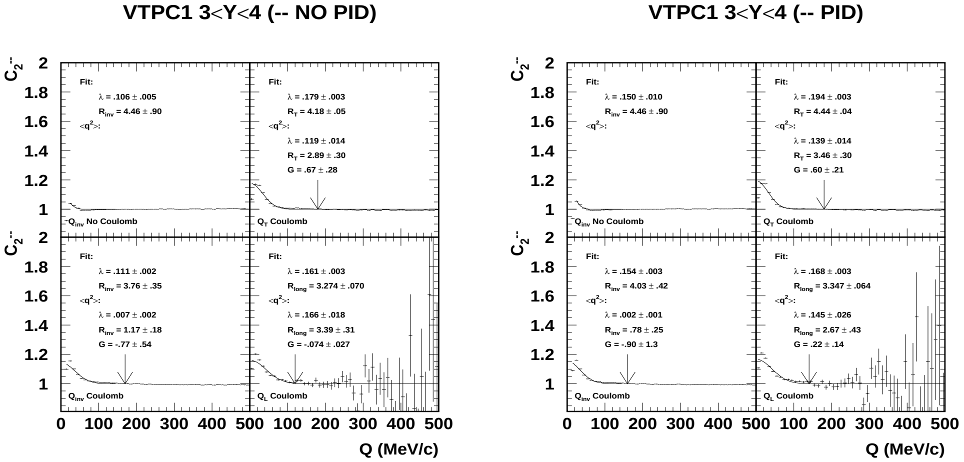

Figure E.3: Comparison between radii from fit and integral methods for 1-d projection of a multi-dimensional correlation function, C^{--} in the rapidity region 3<y<4.

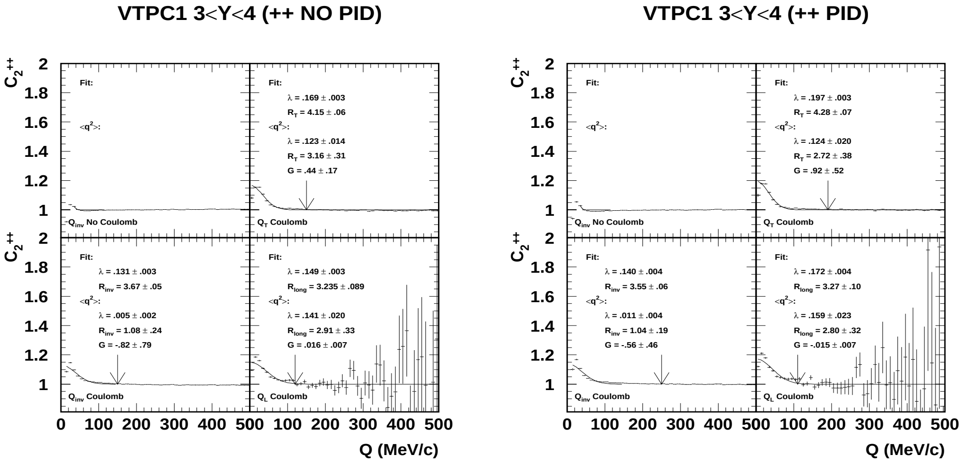

Figure E.4: Comparison between radii from fit and integral methods for 1-d projection of a multi-dimensional correlation function, C^{++} in the rapidity region 3<y<4.

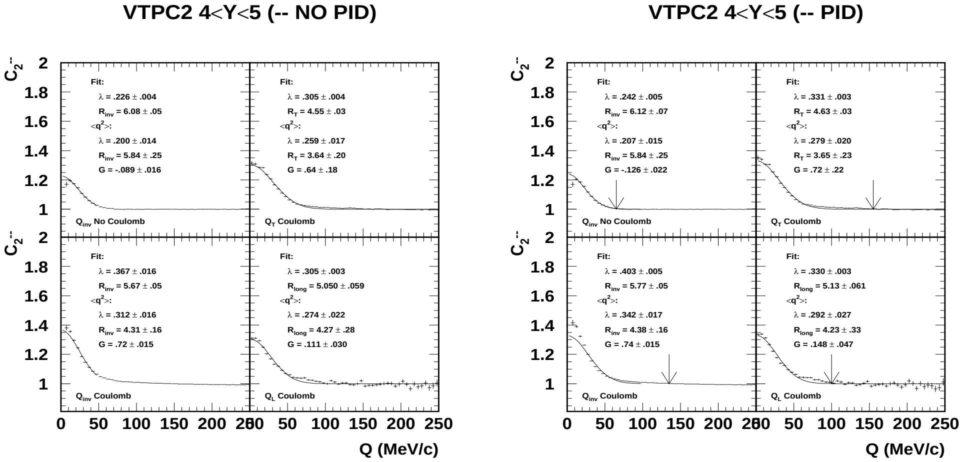

Figure E.5: Comparison between radii from fit and integral methods for 1-d projection of a multi-dimensional correlation function, C^{--} in the rapidity region 4<y<5.

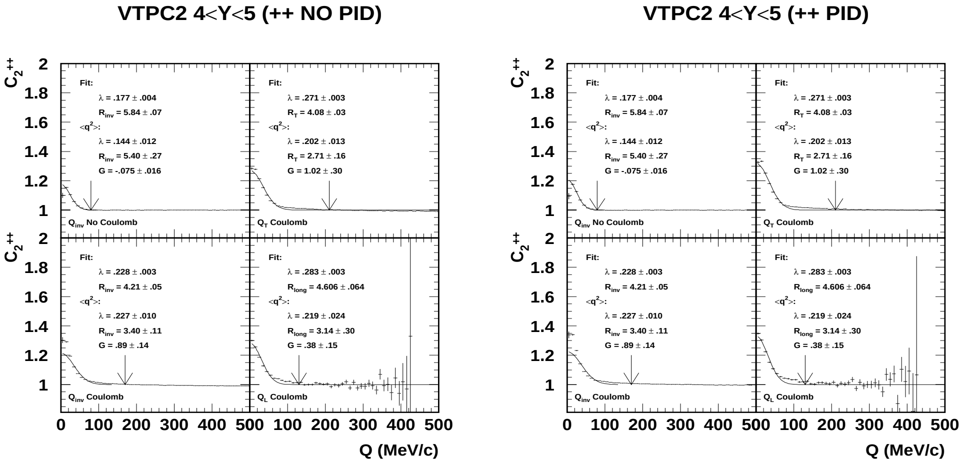

Figure E.6: Comparison between radii from fit and integral methods for 1-d projection of a multi-dimensional correlation function, C^{++} in the rapidity region 4<y<5.

Appendix F

Correlation Functions of Positive Hadrons

Following is a compilation of correlation functions deduced from the positively charged particles; both h^+h^+ and $\pi^+\pi^+$. They are shown in 2 groups; integrated over all K_T as a function of rapidity, and as a function of K_T in rapidity intervals: 2<y<3, 3<y<4, and 4<y<5. They can be directly compared with the correlation functions derived from the negative hadrons presented in chapter 6. The effects of PID are apparent as are the regions where separation power is not sufficient to reduce the contributions of protons in the correlation functions.

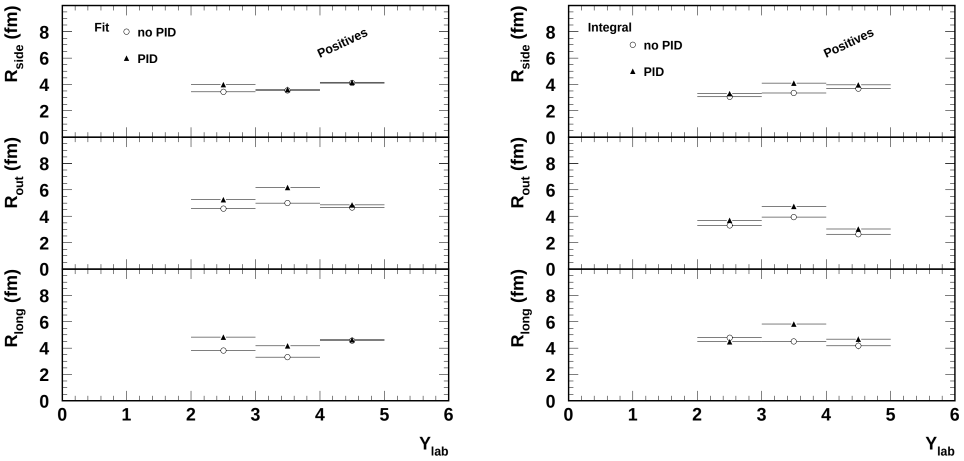

Figure F.1: Comparison between radii from fit and integral methods for multi-dimensional correlation function, C^{++} integrated over all K_T.

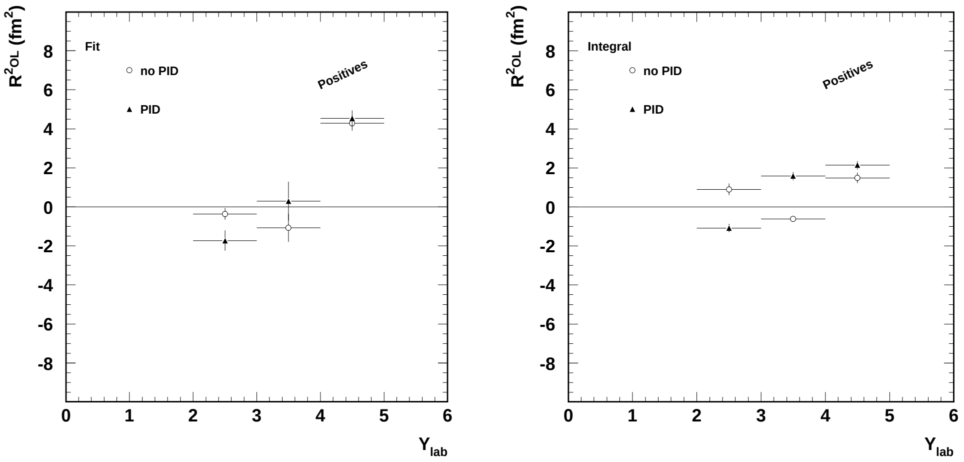

Figure F.2: Comparison between cross term R_{LO}, from fit and integral methods for multi-dimensional correlation function, C^{++} integrated over all K_T.

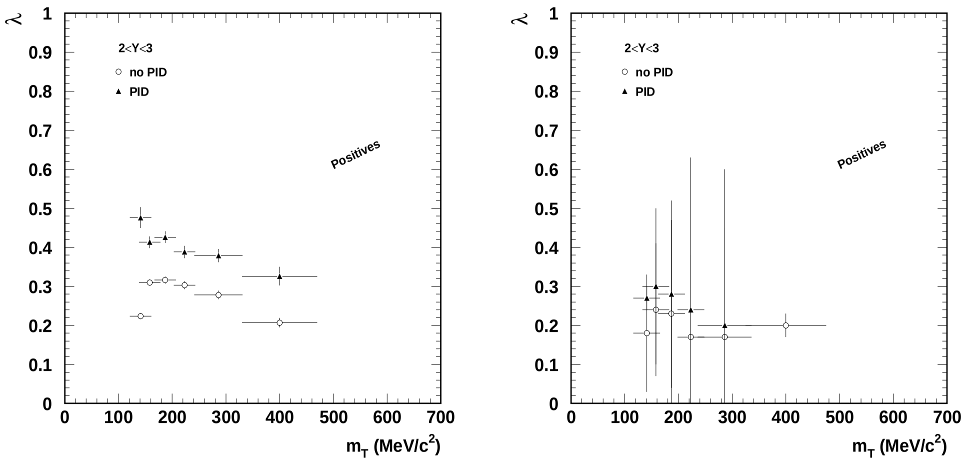

Figure F.3: Comparison between λ from fit and integral methods for multi-dimensional correlation function, C^{++} as a function of K_T in 2<y<3.

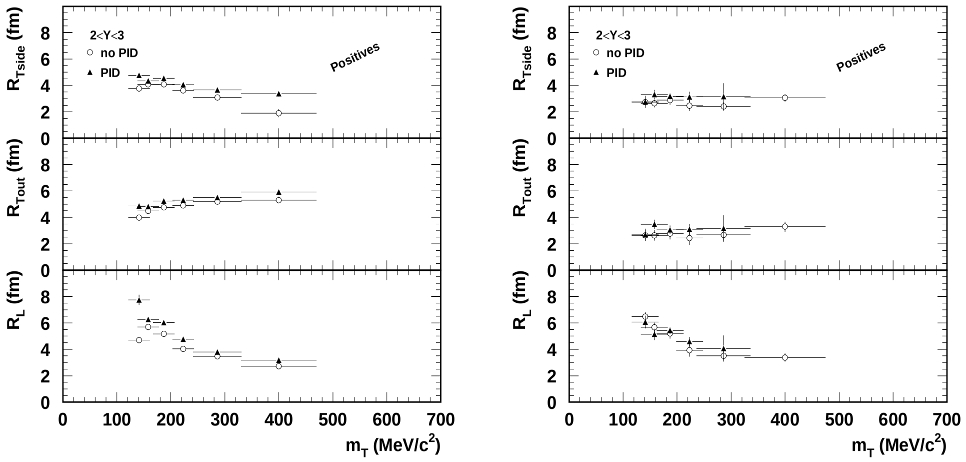

Figure F.4: Comparison between radii from fit and integral methods for multi-dimensional correlation function, C^{++} as a function of K_T in 2<y<3.

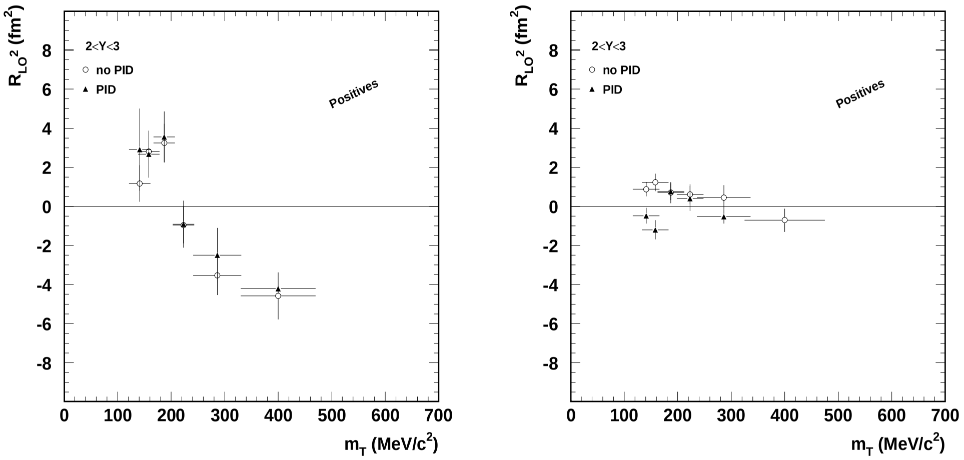

Figure F.5: Comparison between cross-term, R_{LO}, from fit and integral methods for multi-dimensional correlation function, C^{++} as a function of K_T in 2<y<3.

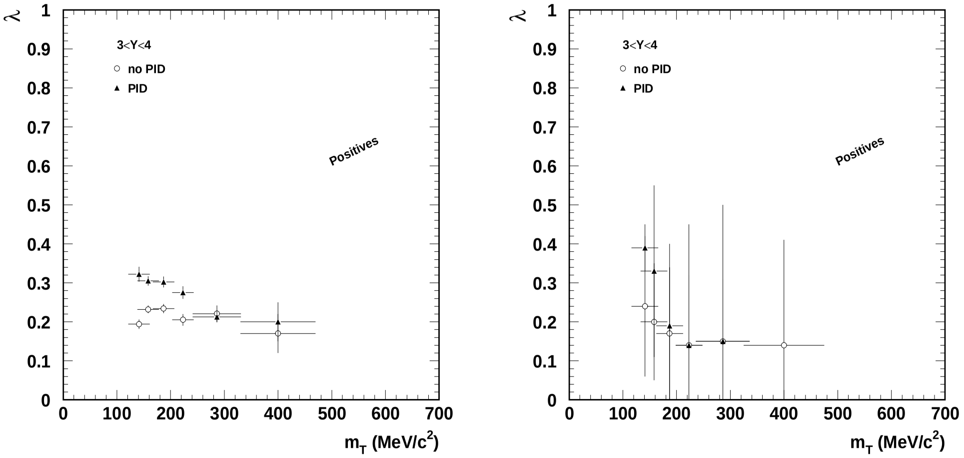

Figure F.6: Comparison between λ from fit and integral methods for multi-dimensional correlation function, C^{++} as a function of K_T in 3<y<4.

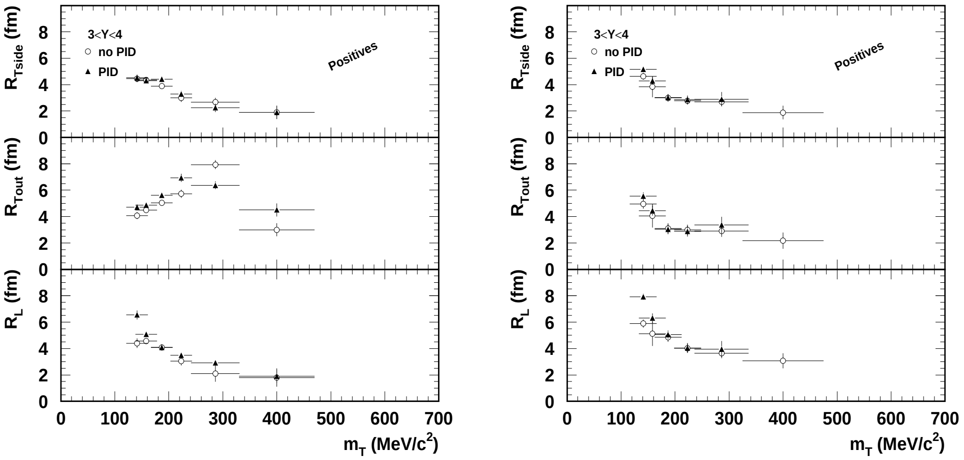

Figure F.7: Comparison between radii from fit and integral methods for multi-dimensional correlation function, C^{++} as a function of K_T in 3<y<4.

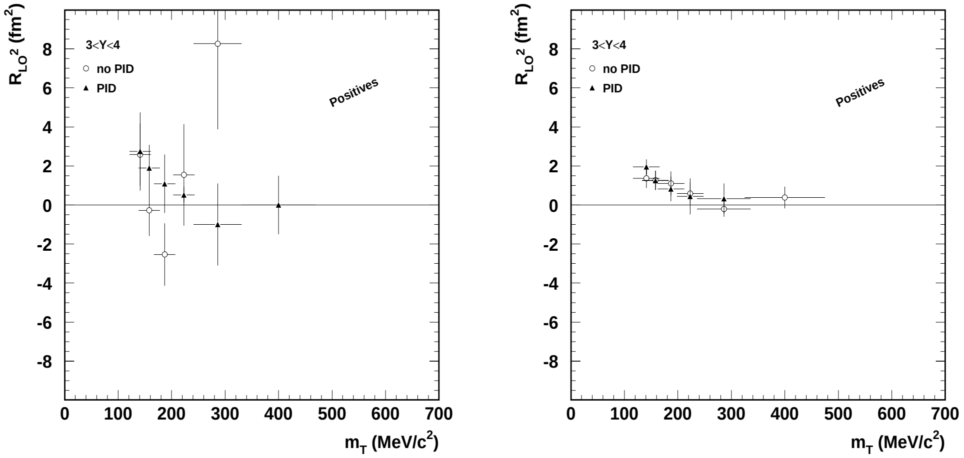

Figure F.8: Comparison between cross-term, R_{ol} from fit and integral methods for multi-dimensional correlation function, C^{++} as a function of K_T in 3<y<4.

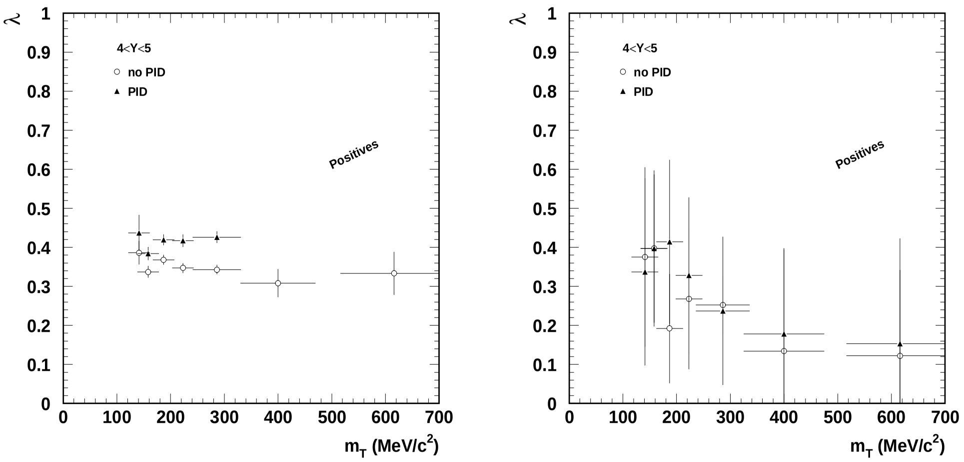

Figure F.9: Comparison between λ from fit and integral methods for multi-dimensional correlation function, C^{++} as a function of K_T in 4<y<5.

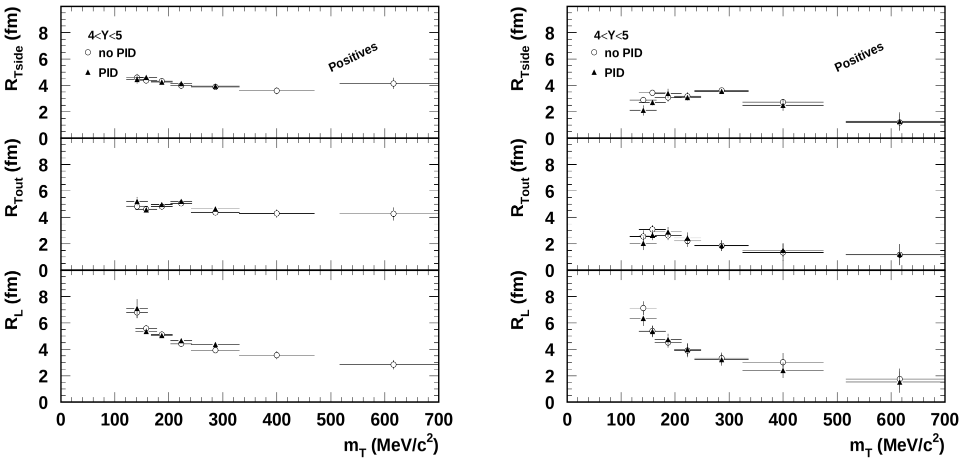

Figure F.10: Comparison between radii from fit and integral methods for multi-dimensional correlation function, C^{++} as a function of K_T in 4<y<5.

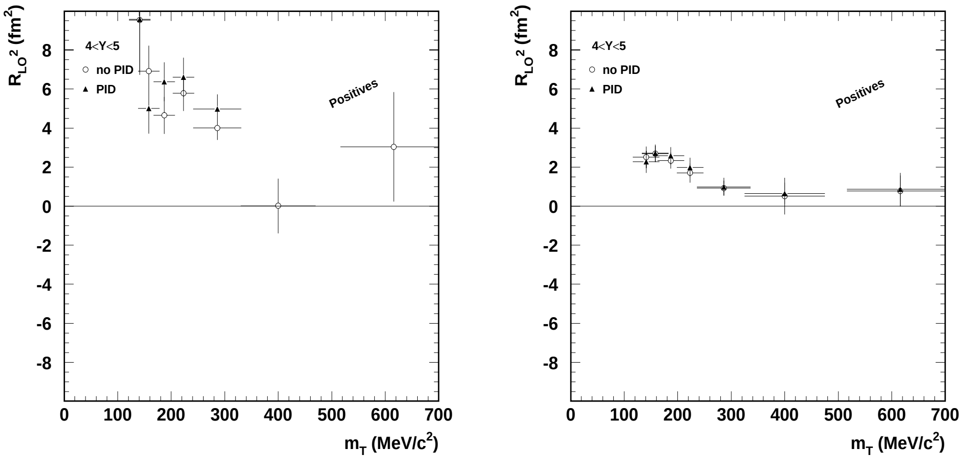

Figure F.11: Comparison between cross-term, R$_{ol}$ from fit and integral methods for multi-dimensional correlation function, C^{++} as a function of K_T in 4<y<5.

Bibliography

[1] E. Rutherford Phil. Mag. **21** (1911) 669.

[2] H. L. Anderson et al., Phys. Rev. **85** (1952) 936.

[3] M. Gell-Mann, Phys. Lett. **8** (1964) 214; G. Zweig, CERN Report, Th 401 and Th 412 (1964) (unpublished).

[4] E.D. Bloom et al., Phys. Rev. Lett **23** (1969) 930.

[5] A. Iwamoto et al., **NPA596** (1996) 329.

[6] A. M. Poskanzer, *A History of Central Collisions at the Bevalac*, LBL-27496, October, 1989.

[7] H. Satz ed., Quark Matter Formation and Heavy Ion Collisions: Proceedings Bielefeld 10-14 May 1982, (Singapore: World-Scientific, 1982).

[8] D. Treille *Review of the Standard Model*, CERN-PPE-92-107, (1992).

[9] J. Chadwick, Proc. R. Soc. (London) **A136** (1932) 692, Nature, **129** (1932) 312.

[10] H. Yukawa, Proc. Phys. Math Soc. (Japan) **17** (1935) 48.

[11] G. P. S. Occhialini et al., Nature **159** (1947) 186, 694; E. Gardner and C. M. G. Lattes, Science **107** (1948) 270.

[12] L. W. Nordheime, Phys. Rev **75** (1949) 1894; E. Feenberg and K. C. Hammack, Phys. Rev. **75** 1877; M. Goeppart-Mayer, Phys. Rev. **74** (1948) 235.

[13] A. Bohr and B. R. Mottelson, Nuclear Structure Vols. 1 & 2, (New York: Benjamin, 1975).

[14] Particle Data Group, Phys. Lett. **B50** (1974) 6; an excellent historty of particle/nuclear physics is given by F. Close. The Particle Explosion, (New York: Oxford University Press, 1987).

[15] G. Arnison et al. (UA1 collaboration), Phys. Lett. **B136** (1984) 294; P. Bagnaia et al. (UA2 collaboration), Phys. Lett. **B138** (1984) 430.

[16] G. 't Hooft, Nucl. Phys. **B33** (1971) 173.

[17] D. Gross and F. Wilczek, Phys. Rev. Lett. **26** (1973) 1343; H. D. Politzer, Phys. Rev. Lett. **26** (1973) 1346.

[18] A text introducing QCD in a field theoretic approach is: M. Kaku, Quantum Field Theory; A Modern Introduction, (Oxford: Oxford University Press, 1993).

[19] M. Lacombe et al., Phys. Rev **C21** (1980) 861.

[20] R. Machleidt et al., Phys. Rep **149** (1987) 1.

[21] For example, S. O. Backman, G. E. Brown, and J.A. Niskanen, Phys. Rep. **124** (1985) 1; B. D. Serot and J. D. Walecka, Adv. Nucl. Phys.**16** (1986) 1; J-M. Richard, Phys. Rep. **212** (1992) 1.

[22] R. Machleidt, Advances in Nucl. Phys. **19** (1989) 189; B. R. Martin, D. Morgan, G. Shaw, Pion-Pion Interactions in Particle Physics, (London: Academic Press, 1976).

[23] for example see B. Lasiuk, University of Saskatchewan, MSc. Thesis (1993) unpublished, and references therein; M. Rho and D. Wilkinson eds., Mesons in Nuclei, (New York: North-Holland Pub. Co.: 1979) 3 vols.

[24] for a program overview see http://www.cebaf.gov/general/visit/experiments/experiments.html.

[25] for a program overview see http://mitbates.mit.edu/exprog.html.

[26] J.Arvieux and B. Pire. Prog. Part. Nucl. Phys. **35** (1995) 299.

[27] H. Toki, M Fujiwara, and T. Kishimoto eds., Nuclear Physics Frontiers with Electro-Weak Probes, (Singapore: World-Scientific 1996).

[28] D. Gross and E. Witten, Phys. Rev **D21** (1980) 446; for a review of the subject see *Lattice 95: Proceedings*, Melbourne, Australia, 11-15 July 1995 in Nucl. Phys. Proc. Suppl. **B47** (1996) pp.1-866.

[29] R. Stock, *High Energy Nuclear Interationcs and Heavy Ion Collisions*, presented at ICHEP'96 Warsaw 25-31 July, 1996; J. Stachel, Nucl. Phys. **A610** (1996) 509c.

[30] J. Engels et al., Phys. Lett. **B101** (1981) 89.

[31] C. P. Singh Phys. Rep. **236** (1993) 149.

[32] R. Hagedorn, CERN-TH 7190/94 (1994).

[33] R. Stock, *High Energy Nuclear Interationcs and Heavy Ion Collisions*, presented at ICHEP'96 Warsaw 25-31 July, 1996. Figures from E. Laermann, Nucl. Phys. **A610** (1996) 1c; F. Karsch, Nucl. Phys. **A590** (1995) 367.

[34] A. Barton et al., Phys. Rev. **D26** (1982) 1497.

[35] A. Barton et al., Phys. Rev. **D27** (1983) 2580.

[36] M. J. Tannenbaum, Int. J. Mod. Phys. **A4** (1989) 3377.

[37] for a review of some important spectroscopy measurements see G. Gratta, H. Newman, and R. Y. Zhu, Ann. Rev. Nucl. Part. Sci. **44** (1994) 453, and references therein.

[38] E. Witten, Phys. Rev. **D30** (1984) 272.

[39] J. H. Applegate and C. J. Hogan, Phys. Rev. **D31** (1985) 3037.

[40] N. Iwamoto, Phys. Rev. **D28** (191983) 2353; for a general review see [31] and references therein.

[41] J. Rafelski, Phys. Rep. **88** (1982) 331.

[42] T. Matsui and H. Satz, Phys. Lett. **B178** (1986) 416.

[43] C. Cerschel and J. Hüfner, Z. Phys. **C56** (1992) 171.

[44] P. Bordalo et al. (NA50 collaboration), Proceedings of Rencontres de Moriond, March 1996, ed. Tranh Tan Van, (Edition Frontieres, 1996); Quark Matter '96 proceedings, Nucl. Phys. **A610** (1997).

[45] R. Stock, NATO Advanced Research Workshop: Hot Hadronic Matter, Theory and Experiment Proceedings. Divonne-les-Bains, June 27-July 1, 1994.

[46] R. Stock et al, (NA35 Collaboration), *Large Acceptance Detector Hadron Detector for an Investigation of Pb-Induced Reactions at the CERN-SPS.* CERN/SPSLC 91-52 P264 Ad. 1.

[47] R. Hanbury-Brown and R. Q. Twiss, Phil. Mag., **45** (1954) 663.

[48] R. Hanbury-Brown and R. Q. Twiss, Nature, **177** (1956) 1046.

[49] G. Goldhaber, W.B. Fowler, T.F. Moang, T.E. Kalogerpoulos, and W.M. Powell, Phys. Rev. Lett., **3** (1959) 181; G. Goldhaber et al., Phys. Rev. **120** (1960) 300.

[50] For example see D. Boal et al., Rev. Mod. Phys., **62** (1990) 553.

[51] P. A. M. Dirac, The Principles of Quantum Mechanics, (London: Oxford University Press,1947).

[52] S. Pratt, Phys. Rev. Lett., **53** (1984) 1219.

[53] for example see W. A. Zajc in *Particle Production in Highly Excited Matter*, eds. H. H. Gutbrod and J. Rafelski, NATO ASI series. Series B. Physics; v. 303, (New York: Plenum Press, 1993), pp. 483; C. Wong, Introduction to High-Energy Heavy Ion Collisions, (Singapore: World-Scientific, 1994), pp. 456.

[54] For example see A. Breakstone et al., Phys. Lett. **162B** (1985) 400, and A. Breakstone et al., Z. Phys. **C33** (1987) 333.

[55] P.D. Acton et al., OPAL Collaboration, Phys. Lett. **B267** (1991) 143.

[56] S.Y.Fung et al. Phys. Rev. Lett., **41** (1978) 1592.

[57] G. Roland et al. (NA35), **NPA566** (1994) 527c, and T. Sugitate et al. (NA44), in *Proceedings of International Symposium,* Japan, eds. M. Biyajima et al., World Scientific, 1992.

[58] S. Chapman, J. Rayford Nix, and U. Heinz, Phys. Rev **C52** (1995) 2694; U. A. Wiedemann, lecture at Univerity of Frankfurt (1996).

[59] S. Chapman, P. Scotto, and U. Heinz *Model Independent Features of the Two-Particle Correlation Function*, HEP-PH-9409349; S. Chapman and U. Heinz, Phys. Lett. **B340** (1994) 250.

[60] S. Chapman et al., Phys. Rev. Lett., **74** (1995) 4400.

[61] G.F Bertsch, Nucl. Phys. **A498** (1989) 173c.

[62] P. Jones et al. (NA49 Collaboration), at Quark Matter '96, Nucl. Phys. **A610** (1997) 188c.

[63] A. Makhlin and Y.Sinyukov, Z. Phys., **C39** (1988) 69.

[64] for example see U. Wiedemann, P. Scotto, and U. Heinz, Phys. Rev. **C53** (1996) 918, and [63].

[65] M. Gyulassy et al., Phys. Rev. **C20** (1979) 2267.

[66] S. Pratt., Phys. Rev. **D33** (1986) 1314.

[67] U. A. Wiedemann, *Invited Lecture at the Triangle Meeting, School and Workshop on Heavy Ion Collisions*, Sept. 1-5, 1996, Bratislava, Slovakia, see Acta Phys. Slov. **47** (1997) 15.

[68] U. Heinz, Nucl. Phys. **A610** (1996) 264.

[69] J. Bäechler et al. NA35 Collaboration, Phys. Rev. Lett. **72** (1994) 1419.

[70] see W. W. M. Allison and P. R. S. Wright, *The Physics of Charged Particle Identification: dE/dx, Cerenkov, and Transition Radiation* in Experimental Techniques in High-Energy Nuclear and Particle Physics, 2nd edition, T. Ferbel ed., (Singapore: World Scientific, 1991).

[71] M. Toy, *MTPC Tracking Environment*, NA49 note 45, (1994).

[72] P. Jacobs for the NA35 collaboration, Time Projection Chambers in NA35 and NA49, at the Winter Workshop on Nuclear Dynamics Key West Fl. (1993) LBL-33810.

[73] C. Garabatos et al., NIM A283 (1989) 553.

[74] H. D. Haseroth, *The CERN Heavy Ion Accelerating Facility*, CERN-PS-95-026 (1995).

[75] M. P. Bougarel, *Performance of the ECR Ion Source of CERN's Heavy Ion Injector*, CERN-PS-96-021-HI, (1995).

[76] D. J. Warner, *The Heavy Ion Linac for the CERN Lead Ion Facility*, CERN-PS-94-34, Sept. (1994), and Proc. of LINAC '94, Tsukuba, Japan, August 21-26 (1994).

[77] T. Abbott et al. (E802 Collaboration), Phys. Lett. **B197** (1987) 285; J. Bächler et al. (NA35 Collaboration), Phys. Lett. **B184** (1987) 271

[78] R.Renfordt et al., The NA49 Laser System, NA49 note 90, (1995).

[79] B. B. Rossi and H. H. Staub, Ionization Chambers and Counters Experimental Techniques, (New York: McGraw-Hill, 1949); G. Charpak et al., NIM **62** (1968) 262.

[80] G. Giorginis, et al., NIM **A273** (1988) 650.

[81] J. Marx et al., *The PEP-4 Facility as the Initial Detector at SLC: Letter of Intent* SLAC-PROPOSAL-SLC-05, Sept. 1982; H. Aihara et al. (PEP-4 Collaboration), IEEE Trans. Nucl. Sci. **30** (1983) 76.

[82] for example *The ALEPH Handbook*, ALEPH 89-77 (1989); *The Components of the DELPHI Detector* 82-3 (1982).

[83] H.G. Pugh et al., A Time Projection Chamber for the Study of Nucleus-Nucleus Collisions at the Bevalac LBL-22314.

[84] W. Blum and L. Rolandi, Particle Detection with Drift Chambers, (New-York: Springer-Verlag, 1993).

[85] D. L. Fancher and A. C. Schaffer, IEEE Trans. Nucl. Sci. **26** (1979) 150.

[86] M. Gaździcki and R. Renfordt, *Optimization of Pad Geometry in VTPC2*, NA49 note 10, (1992); M. Fuchs, *Vertex TPC1 Pad-orientation study*, NA49

note 24, (1992); H. Appelshäuser, *Optimization of VTPC1 Pad-Layout*, NA49 note 49, (1995).

[87] W.B. Atwood et al., NIM **A306** (1991) 446.

[88] H. G. Fischer, *Kr Calibration in NA49 TPCs*, CERN Software Meeting, October 7-8, 1995.

[89] T. Alber et al., NIM **A349** (1994) 56.

[90] F. Bieser et al., NIM **A385** (1997) 535.

[91] W. Rauch et al. (NA49 Collaboration), IEEE Trans. Nucl. Sci. **41** (1994) 30.

[92] G. Daskalakis et al., NIM **A328** (1993) 495.

[93] J. Bächler et al., Z. Phys. C52 (1991) 239.

[94] C. Brand et at., NIM **A237** (1985) 501.

[95] F. Gabler, Diploma-Thesis, Frankfurt Univerity (1995), unpublished.

[96] A. Brybicki, *Status of Kr Analysis*, NA49 Collaboration Meeting April 7-11, 1997; B. Lasiuk , *Electronics Calibration and Its Effect on dE/dx Performance*, NA49 Collaboration Meeting April 7-11, 1997.

[97] J. Günther et al., *Influence of cluster coordinate-determination on the spatial resolution Cluster finder*, NA49 note 79, (1995).

[98] B. Lasiuk et al., *The NA49 Magnet Mapping Measurement Program*, NA49 note 74, (1995).

[99] M. Fuchs., NIM **A367** (1995) 394.

[100] W. Blum and L. Rolandi, Particle Detection with Drift Chambers, (New-York: Springer-Verlag, 1993).

[101] R. L. Gluckstern, NIM **24** (1963) 381.

[102] H. Bethe and J. Ashkin, *Passage of Radiations through Matter* in, Experimental Nuclear Physics, E. Segré (ed.) (New York: Wiley 1953-59).

[103] E. Fermi, Phys. Rev. **57** (1940) 485.

[104] R. M. Sternheimer and R. F. Peierls, Phys. Rev. **B3** (1971) 3681.

[105] R. M. Sternheimer et al., Atomic and Nuclear Data Tables, **30** (1984) 261.

[106] J. H. Cobb, W. W. M. Allison, and J. N. Bunch, NIM **133** (1976) 315.

[107] W. Lohmann R. Kopp, and R. Voss, *Energy Loss of Muons in the High Energy Range 1-10000 GeV*, CERN 85-03 (1985).

[108] for an extensive compilation see J. F. Ziegler et al., The Stopping of Ions in Matter, (Permagon Press, 1985), vol I and II.

[109] B. Rossi, High Energy Particles, (Englewood Cliffs: Prentice-Hall, 1952).

[110] U. Fano, Ann. Rev. Nucl. Sc. **13** (1963) 1.

[111] L. G. Christophorou, Atomic and Molecular Radiation Physics, (London: Wiley, 1971).

[112] D. Combecher, *W-values of Low Energy Electrons for Several Gases*, as in W. Blum and L. Rolandi, Particle Detection with Drift Chambers, (New-York: Springer-Verlag, 1993).

[113] F. Sauli, *Principles of Operation of Multiwire Proportional and Drift Chambers.* CERN Report 77-09 (1977).

[114] H. Fischle, J. Heintze, B. Schmidt, NIM **A301** (1991) 202.

[115] L. Landau, J. Phys. U.S.S.R. **8** (1944) 201; ed. D. Ter Haar Collected Papers of L. D. Landau, (Oxford: Permagon Press, 1965).

[116] L. Livingston and H. Bethe, Rev. Mod Phys. **9** (1937) 245.

[117] F. Reif, Fundamentals of Statistical and Thermal Physics, (New York: McGraw-Hill 1965), see pp. 463.

[118] P. V. Vavilov, Sov. Phys. JETP **5** (1957) 749.

[119] J. E. Moyal, Phil. Mag. **46** (1955) 263.

[120] I. Lehraus et al., NIM **196** (1982) 361.

[121] F. Lapique and F. Piuz, NIM **175** (1980) 297; V. K. Ermilova et al., Sov. Phys.-JETP **29** (1969) 861.

[122] B. Lasiuk and C. A. Whitten Jr., *A Report on Specific Ionization in VTPC1*, NA49 note 99, (1996).

[123] I. Endo, NIM **188** (1981) 51.

[124] H. G. Fischer and J. Bächler, NA49 software meeting, CERN, February 10-14, 1997.

[125] S. R. Amendolia et al., NIM **A244** (1986) 516; H. Appelshäuser, University of Frankfurt, Ph.D. Thesis (1996), unpublished.

[126] J. Bächler, private communication; E. Gatti, NIM **163** (1979) 83.

[127] F. Paul Brady and J. Dunn, *Effect of ADC Threshold on Cluster Charge and* $\frac{dE}{dx}$, NA49 note 85, (1995).

[128] G. Igo and R. M. Eisberg, Rev. Sci. Instr. **25** (1954) 450.

[129] A. I. Alikhanov et al., *Proc. CERN Symposium on High Energy Accelerators and Pion Physics*, **2** (1956) 87; (CERN 56-25).

[130] for example, I. Lehraus et al., NIM **153** (1978) 347.

[131] W. W. M. Allison and Cobb, Ann. Rev. Nucl. Part. Sci, **30** (1980) 253.

[132] V. A. Chechin and V. C. Ermilova, NIM **136** (1976) 551.

[133] G. Roland, University of Frankfurt, Ph.D. Thesis (1992), unpublished.

[134] A. H. Walenta, NIM **161** (1979) 435.

[135] W. W, M. Allison, *Relativistic Particle Identification by dE/dx: The Fruits of Experience with ISIS*, International Conference on Instrumentation for Colliding Beam Physics, Oxford-16/82.

[136] I. Lehraus, R. Matthewson, and W. Tejessy, *Particle Identification by dE/dx Sampling in High Pressure Drift Detectors.*, CERN/EF 81-14, 14 October, 1981; also see Phys. Scripta **23** (1981) 727, and references therein.

[137] I. Lehraus et al., *Pressure Dependence of the Relativistic Rise in Neon and Highest Attainable Ionization Sampling Resolution on Neon, Argon, Ethylene, and Propane*, CERN/EF 82-14, 23 September, 1982; also in IEEE Trans. Nucl. Sci. **30** (1983) 50.

[138] K. Emi et al., NIM **A379** (1996) 225.

[139] W. W. M. Allison et al., NIM **133** (1976) 325, and references therein.

[140] W. S. Toothacker et al., NIM **A273** (1988) 97.

[141] H. G. Fischer, private communication.

[142] H. G. Fischer, CERN Academic Training Lectures, December 9-13, 1996.

[143] H. D. Maccabee and D. G. Papworth, Phys. Lett. **30A** (1969) 241; R. M. Sternheimer, Phys. Rev. **91** (1953) 256.

[144] B. Lasiuk , *Electronics Calibration and Its Effect on dE/dx Performance*, NA49 Collaboration Meeting April 7-11, 1997.

[145] A. Mock, University of Munich, Ph.D. Thesis (1997), unpublished.

[146] Z. Fodor, NA49 software meeting, CERN, February 10-14, 1997.

[147] H. Appelshäuser, University of Frankfurt, Ph.D. Thesis (1996), unpublished.

[148] M.Baker, Nucl. Phys. **A610** (1996) 213c.

[149] for example see G. Baym and P. Braun-Munzinger, Nucl. Phys. **A610** (1996)286c; D.V Anchishkin et al, *Coulomb Final State Interaction in Pion Interferometry for the Processes of High Multiplicity*; R. Lednicky and V. L. Lyuboshitz, Yad. Fiz. **32** (1982) 770, and R. Lednicky et al., SUBATECH-94-22, Nantes, 1994 subm. to Nucl. Phys. A.

[150] S. Pratt et al., Phys. Rev. **C42** (1990) 2646.

[151] S. Schönfelder, Dissertation, University of Munich (1997) unpublished.

[152] T. Alber et al. (NA35 collaboration), Z. Phys. **C73** (1997) 443.

[153] F. Sikler, NA49 Collaboration meeting (CERN), April 7-11, 1997.

[154] J. Cramer, NA49 collaboration meeting, October 9-12, 1996.

[155] H. Böggild et al., Phys. Lett., **B302** (1993) 510.

[156] for example J. G. Cramer and K. Kadija, Phys. Rev. **C53** (1996) 908.

[157] L. Rosselet et al., Nucl. Phys. **A610** (1996) 256c.

[158] B. Lasiuk, Acta Phy. Slov. **47** (1997) 15.

[159] D. Miśkowiec et al., Nucl. Phys. **A610** (1996) 227.

[160] P. Seyboth, private communication.

[161] for example see S. Chapman et al., Phys. Rev. **C52** (1995) 2694; A. N. Maklin and Y. M. Sinyukov, Z. Phys. **C39** (1988) 69.

[162] S. Chapman et al., Phys. Rev. **C52** (1995) 2694.

[163] A. N. Maklin and Y. M. Sinyukov, Z. Phys. **C39** (1988) 69.

[164] M. Herrmann and G. F. Bertsch, Phys.Rev. **C51** (1995) 328.

[165] S. Chapman, P. Scotto, and U. Heinz, hep-ph/9409349 (1994).

[166] R. Hagedorn in Hot Hadronic Matter: Theory and Experiment, J. Letessier et al. eds., (New York: Plenum Press, 1995) pp. 13; CERN-TH 7190/94.

[167] J. D. Bjorken, Phys. Rev. **D27** (1983) 140.

[168] U. Heinz et al, Nucl. Phys. **A610** (1996) 264.

[169] R. Stock, NATO Advanced Research Workshop: Hot Hadronic Matter, Theory and Experiment Proceedings. Divonne-les-Bains, June 27-July 1, 1994.